Astronomy Letters, Vol. 30, No. 5, 2004, pp. 283–292. Translated from Pis'ma v Astronomicheskiĭ Zhurnal, Vol. 30, No. 5, 2004, pp. 323–333.

A Photometric Study of Faint Galaxies in the Field of GRB 000926

T. A. Fatkhullin[1]*, A. A. Vasil'ev[2], and V. P. Reshetnikov[2]**

[1] *Special Astrophysical Observatory, Russian Academy of Sciences, Nizhniĭ Arkhyz, 357147 Karachai-Cherkessian Republic, Russia*

[2] *Astronomical Institute, St. Petersburg State University, Universitetskiĭ pr. 28, Petrodvorets, 198504 Russia*

Received September 30, 2003

Abstract—We present our B, V, R_c, and I_c observations of a $3'.6 \times 3'$ field centered on the host galaxy of GRB 000926 ($\alpha_{2000.0} = 17^h04^m11^s$, $\delta_{2000.0} = +51°47'9''.8$). The observations were carried out on the 6-m Special Astrophysical Observatory telescope using the SCORPIO instrument. The catalog of galaxies detected in this field includes 264 objects for which the signal-to-noise ratio is larger than 5 in each photometric band. The following limiting magnitudes in the catalog correspond to this limitation: 26.6 (B), 25.7 (V), 25.8 (R), and 24.5 (I). The differential galaxy counts are in good agreement with previously published CCD observations of deep fields. We estimated the photometric redshifts for all of the cataloged objects and studied the color variations of the galaxies with z. For luminous spiral galaxies with $M(B) < -18$, we found no evidence for any noticeable evolution of their linear sizes to $z \sim 1$.

Key words: *distant galaxies, photometric observations.*

INTRODUCTION

In recent years, significant progress has been made in studying the properties and evolution of distant galaxies. An important role in this progress has been played by detailed studies of several so-called deep fields—relatively small areas imaged (generally in several color bands) with long exposure times. The best-known deep fields include the northern and southern fields of the Hubble Space Telescope (Ferguson *et al.* 2000), Subaru (Maihara *et al.* 2001), VLT FORS (Heidt *et al.* 2003), and the most recent and deepest (in the history of optical astronomy) survey conducted as part of the GOODS (Great Observatories Origins Deep Survey) project with the Hubble Space Telescope (Giavalisco *et al.* 2003). In addition to surveys covering an appreciable part of the sky (2MASS, 2dF, SDSS, and others), but limited to relatively low redshifts ($z \leq 0.3$), deep fields allow the properties of high z galaxies to be studied and provide information about the evolution of the integrated parameters of galaxies.

Our primary objective was to study in detail the faint galaxies distinguished in the deep field obtained with the 6-m Special Astrophysical Observatory (SAO) telescope as part of our program of optical identification of gamma-ray bursts (GRBs). In recent years, investigators have increasingly pointed out that, with the accumulation of observational data, GRBs with their afterglows and host galaxies are becoming a useful tool in observational cosmology (see, e.g., Djorgovski *et al.* 2003; Ramirez-Ruiz *et al.* 2001; Trentham *et al.* 2002; and references therein). Thus, a comparative analysis of the properties of GRB host galaxies with the properties of galaxies at the same redshifts is now of relevant interest. One of the methods for solving this problem is to study the population of faint galaxies in the deep fields of GRB host galaxies.

OBSERVATIONS AND THEIR REDUCTION

We carried out our photometric observations of the field of the host galaxy of GRB 000926 on July 24 and 25, 2001, using the 6-m SAO telescope. The observing conditions were photometric with 1.3-arcsec seeing, measured as the full width at half maximum (FWHM) of the images of starlike objects in the field. The field was centered on the coordinates of the host galaxy $\alpha_{2000.0} = 17^h04^m11^s$ and $\delta_{2000.0} = +51°47'9''.8$, which correspond to the Galactic latitude and longitude $b = 37°21'$ and $l = 77°45'$, respectively. According to the infrared maps taken from the paper by Schlegel *et al.* (1998), the Galactic reddening toward the field being studied is $E(B-V) = 0.023$. In our observations, we used the SCORPIO (Spectral Camera

*E-mail: timur@sao.ru

**E-mail: resh@gong.astro.spbu.ru

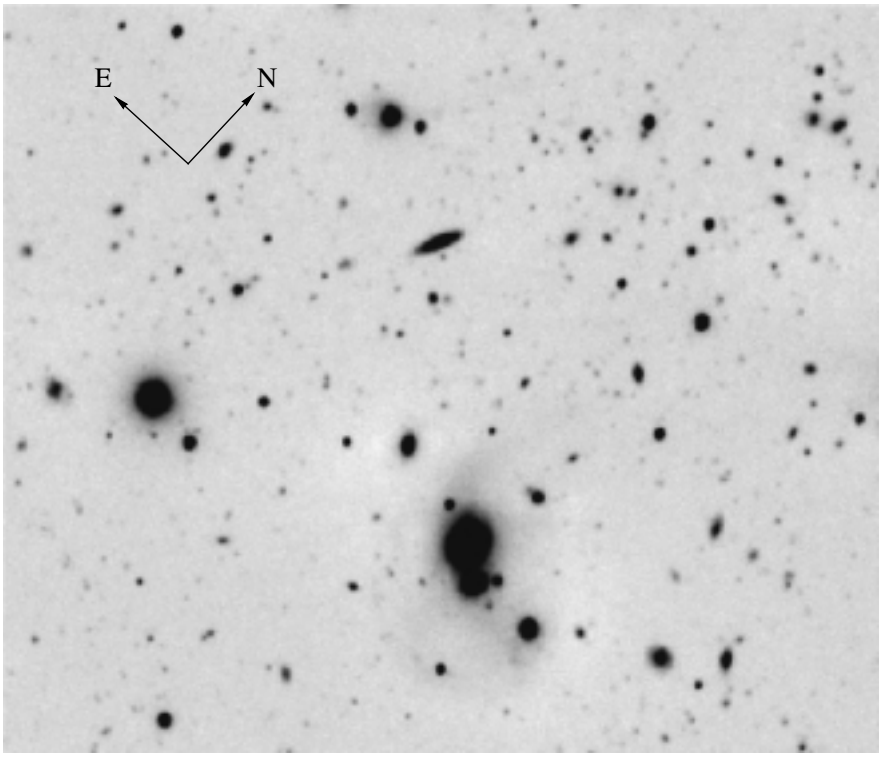

Fig. 1. Reproduction of the field of GRB 000926. The field sizes are $3'.6 \times 3'$.

with Optical Reducer for Photometrical and Interferometrical Observations; for a description, see http://www.sao.ru/moisav/scorpio/scorpio.html) instrument mounted at the prime focus of the 6-m SAO telescope. The detector was a TK1024 1024 × 1024 CCD array. The pixel size was 24 μm, which corresponded to an angular scale of $0''.289$ per pixel. The CCD response curve and the SCORPIO broadband filters reproduced a photometric system close to the standard Johnson–Cousins BVR_cI_c system (Bessel 1990). We took five frames in each of the B and V bands with total exposure times of 2500^s and 1500^s, respectively; ten frames in R_c (1800^s); and fifteen frames in I_c (1800^s). The absolute photometric calibration of the data was performed using the observations of standard stars from the lists by Landolt (1992) and Stetson (accessible at http://cadcwww.dao.nrc.ca/cadcbin/wdb/astrocat/stetson/query) on the same nights.

The primary data reduction was performed using the ESO-MIDAS software package.[1] It included debiasing, flat fielding, defringing in R_c and I_c, and cosmic-ray hit removal (for a detailed description, see the dissertation by Fatkhullin 2003). All of the frames taken in one color band were coadded. The coadded frames were reduced to the same orientation and to a single coordinate system. The sizes of the region where the coadded images overlapped in all bands were $3'.6 \times 3'$. This region was used for the subsequent analysis (Fig. 1).

[1] This package is supported and distributed by the European Southern Observatory.

LARGE-SCALE PHOTOMETRY OF OBJECTS IN THE FIELD

Extracting Objects

We used the SExtractor (Source Extractor) (Bertin and Arnouts 1996) package to extract objects in the field and to perform their photometry. This package is unique in that it allows us to extract objects and construct their isophotes on one image and to calculate the fluxes within these isophotes on another image. Thus, we can determine the fluxes in all bands for a given object within the same region of the image. On the other hand, this technique makes it possible to find all of the objects in the field from its common image for all bands, which allows problems with the identification of the same object in different bands to be avoided.

There are several methods for constructing a common image (i.e., the detection field). For example, the field obtained by coadding the frames in different color bands is often used to extract objects. We used a

relatively new method, that of constructing a χ^2-field. The χ^2-field is a common image for all bands, and it is used to extract objects and to construct a common catalog of objects for all bands. The idea of the method is that probabilistic methods are used to analyze the distribution of image pixel values and to determine the optimum detection limit for objects above the background level (Szalay *et al.* 1999).

Schematically, the process of constructing the χ^2-field can be described as follows. The mean and rms deviation (σ_b) of the sky background (the distribution of sky background values is assumed to be Gaussian) are determined from the images in each color band. Subsequently, the corresponding background value is subtracted from each image, and the resulting frame is divided by σ_b. As a result, we obtain a transformed image for each band in which the sky background is specified by a Gaussian with a zero mean and a unit variance. If we consider the combined transformed images, each pixel of the common field may be represented as a vector with the number of elements equal to the number of bands. The resulting χ^2-field is an image, each pixel of which is equal to the square of the length of the corresponding vector of the common field.

If the observed region contained no objects and displayed only the sky background, then the probability distribution function for χ^2-field values would correspond to χ^2 with the number of degrees of freedom equal to the number of bands. However, an actual field contains objects, and, therefore, the distribution of χ^2-field values is distorted. By analyzing the χ^2-fields for the observed region and for the sky background, we can determine the optimum detection limit for objects in the actual field; this limit turns out to be lower than that in the method of coadding the frames in different color bands.

The detection conditions were specified in such a way that objects that occupied an area of no less than five pixels were extracted at fluxes in these pixels exceeding 3σ above the background level. For detection, we also used filtering based on a wavelet analysis using a mexhat-type filter with a FWHM that corresponded to the quality of our images, i.e., $1''.3$. This filtering allowed us to effectively extract objects in frames with a large image density and around bright extended galaxies as well as to separate the components of multiple objects.

Object Extraction Results and Photometry

More than 550 objects satisfied the detection criteria. However, to eliminate problems related to inaccurate photometry due to the defects of the objects themselves, we excluded those which turned out to be near the image boundaries and in two regions around very bright objects (an overexposed star and a large interacting system of galaxies). Thus, slightly more than 400 objects remained.

To increase the reliability of the subsequent analysis, we included in the final catalog only those objects for which the signal-to-noise ratio was larger than 5 in each band. There were 285 such objects. The following limiting magnitudes in the catalog corresponded to this limitation: 26.6 (B), 25.7 (V), 25.8 (R), and 24.5 (I).

For each object, we determined the total apparent magnitudes and the corresponding color indices using the so-called best magnitudes generated by the SExtractor package. These values are the best fits to the asymptotic magnitudes of extended objects (Bertin and Arnouts 1996).

The SExtractor package allows the objects to be separated into starlike and extended ones by assigning a corresponding starlikeness index from 0 (extended) to 1 (star) to each of them. For the subsequent analysis, we selected only those objects for which the starlikeness index was less than 0.7 in B (in this band, the stellar disks and spiral arms of galaxies are separated relatively better). There were 264 such objects. We attributed the objects with an index larger than 0.7 (their number was 21) to stars.

ESTIMATING THE REDSHIFTS

Determining the spectroscopic redshifts for several hundred faint objects extracted in deep fields is a complicated and time-consuming observational problem. Fortunately, for many problems (e.g., for estimating the evolution of the galaxy luminosity function), the so-called photometric redshifts estimated from multicolor photometry turn out to be quite acceptable. The accuracy of these z estimates is about 10%, which is high enough for statistical studies of the properties of distant objects. The main idea of the photometric redshift estimation is very simple: an object's multicolor photometry may be considered as a low-resolution spectrum that is used to estimate z (Baum 1963).

In practice, we estimated the photometric redshifts for the extended objects of our sample using the Hyperz software package (Bolzonella *et al.* 2000). The input data for Hyperz were: the apparent magnitudes of the objects in four bands, the internal extinction law (we used the law by Calzetti *et al.* (2000) for starburst galaxies, which is most commonly used for studies similar to our own), the redshift range in which the solution is sought (we considered z from 0 to 1.3), and the cosmological model (we used a flat model with $\Omega_m = 0.3$, $\Omega_\Lambda = 0.7$, and $H_0 = 70$ km s^{-1} Mpc^{-1}).

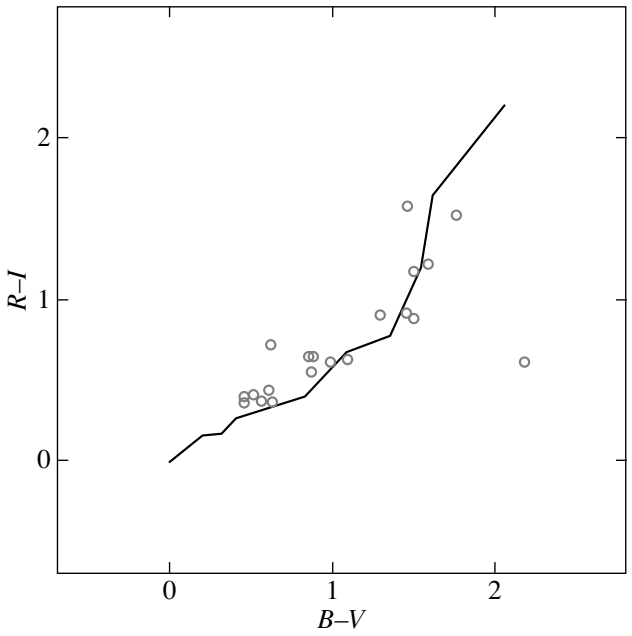

Fig. 2. Color distribution for starlike objects in the two-color diagram. The solid line represents the color sequence for main sequence stars.

The observed spectra of the galaxies were compared with the synthetic spectra for E, Sa, Sc, Im, and starburst galaxies taken from the GISSEL98 library.

Apart from the redshift estimate, the Hyperz package yielded the following basic parameters for each object: the spectral type of the galaxy (based on the similarity between the spectral energy distribution of the object and one of the synthetic spectra), the age, the absolute B magnitude, and a number of others.

RESULTS AND DISCUSSION

Our catalog of extended objects ($N = 264$) has the following integrated parameters:

(1) the mean absolute magnitude of the galaxies is $\langle M_B \rangle = -17.4 \pm 2.7(\sigma)$;

(2) the mean photometric redshift is $\langle z \rangle = 0.53 \pm 0.39$;

(3) the starlikeness index in the B band is 0.08 ± 0.12, i.e., extended objects dominate in the catalog;

(4) the apparent flattening of the galaxies varies between 0.22 and 1.00 with a mean value of $\langle b/a \rangle = 0.80 \pm 0.20$.

Irregular and starburst galaxies (126 of the 264 objects or 48%) constitute about one half of the catalog. Sa–Sc spiral galaxies are encountered in almost a third of the cases (79 objects or 30%). The contribution of elliptical galaxies is 22% (59 objects).

The mean angular size of the objects (FWHM) corrected for the FWHM of the stars varies between $1''.0$ in R to $1''.2$ in I (the errors of the means are $\pm 0''.5$). At the mean redshift, a linear size of ≈ 7 kpc corresponds to this angular size. If we restrict our analysis to relatively near galaxies at $z \leq 0.5$ (in this case, the mean redshifts of the galaxies of various spectral types are close), the expected dependence of the linear sizes on the galaxy type shows up. Thus, the mean FWHM for elliptical galaxies corresponds to a linear size of 3.4 kpc, while starburst galaxies exhibit a more extended brightness distribution with FWHM $\approx$4.7 kpc.

Starlike Objects

We used a fairly stringent criterion to separate galaxies and stars: we attributed objects with a starlikeness index in B of less than 0.7 to galaxies (a less stringent limitation, e.g., 0.9–0.95 (Arnouts *et al.* 2001), is commonly used).

The number of stars found in the field (21 stars with apparent magnitudes $B \leq 24.5$) is in good agreement with the prediction of Bezanson's Milky Way model (for a description of this model, see, e.g., Robin *et al.* 2000). In a field with an area of 0.003 square degrees located at the Galactic coordinates that correspond to our region, this model predicts 24 stars with $B \leq 24.5$. Given the small size of the field under study, such a close coincidence is, of course, partly accidental. However, it is indicative of the relatively small number of stars that could be erroneously attributed to galaxies.

Figure 2 shows the distribution of stars in the two-color diagram. The solid line in the figure represents the color sequence for main sequence stars (Sparke and Gallagher 2000). Most of the stars exhibit colors typical of main-sequence dwarfs.

Galaxy Counts

The differential galaxy counts normalized to 1 sq. degree and found within $0^m.5$ bins are shown in Fig. 3 (circles). These counts were not corrected for observational selection and represent the actually observed numbers. The crosses in the figure indicate similar counts for the VIRMOS survey (Le Fevre 2003; McCracken *et al.* 2003). Clearly, our counts are in excellent agreement with this survey. For apparent magnitudes $B < 25$, $V < 24.5$, $R_c < 24$, and $I_c < 24$, the difference in the numbers of galaxies observed in one magnitude bin, on average, does not exceed 20%. For fainter magnitudes, observational selection, which manifests itself in the form of bends in the curves of differential counts in Fig. 3, strongly affects our data.

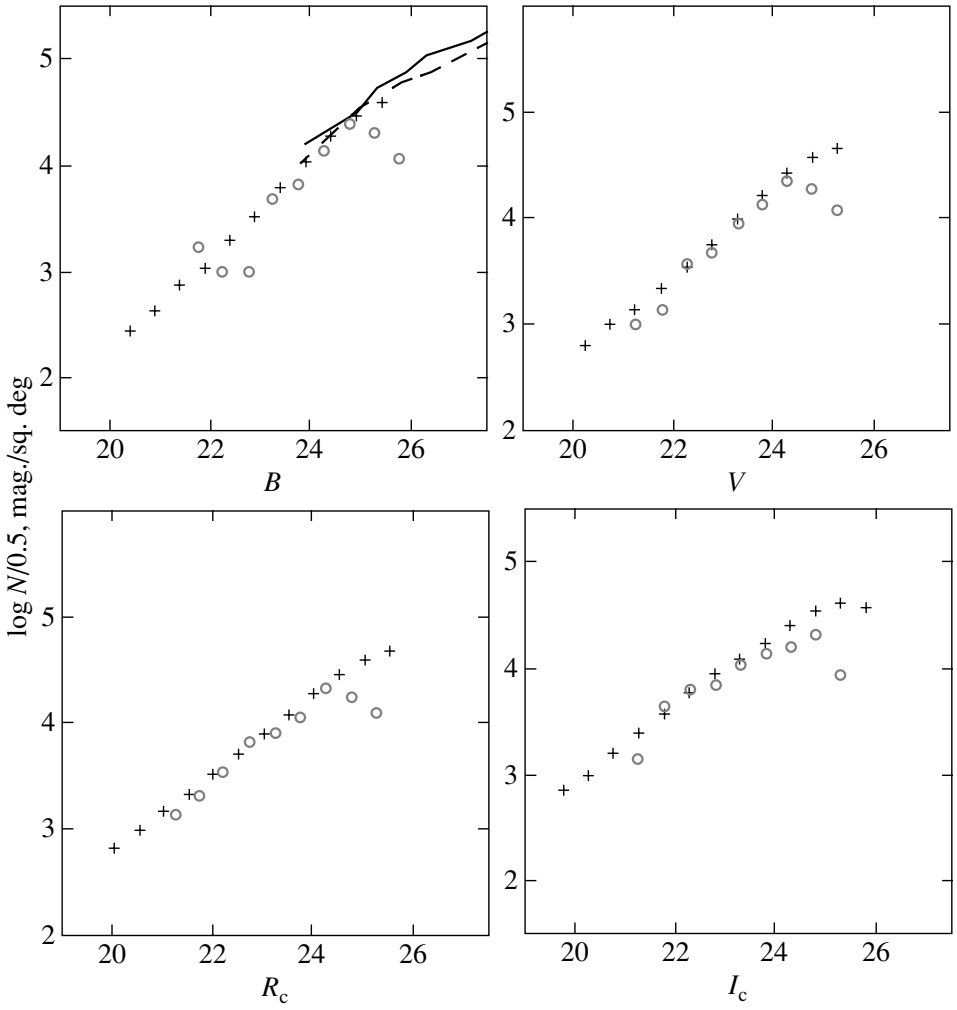

Fig. 3. Differential galaxy counts in the field of GRB 000926 (circles) in different bands. The crosses indicate similar counts for the VIRMOS survey (McCracken *et al.* 2003). The solid and dashed lines represent the B-band counts for the northern and southern deep fields of the Hubble Space Telescope, respectively (Metcalfe *et al.* 2001).

The slopes of the curves shown in Fig. 3 are also in good agreement. According to our data, these slopes are

$$0.47 \pm 0.09 \quad (B \leq 25), \quad 0.47 \pm 0.04 \quad (V \leq 24),$$
$$0.38 \pm 0.03 \ (R_c \leq 24) \text{ and } 0.29 \pm 0.04 \ (I_c \leq 24).$$

A similar variation in the slopes of the curves of differential counts when passing from B to I_c was also pointed out by McCracken *et al.* (2003).

On the other hand, the VIRMOS data are in excellent agreement (to within ~10%) with previous CCD galaxy counts (McCracken *et al.* 2003). As an example, Fig. 3 shows the counts for the northern and southern deep fields of the Hubble Space Telescope (Metcalfe *et al.* 2001). Near $B \sim 25$, the ground-based and space counts join to form a single dependence that is currently traceable to $B \sim 29$. A detailed interpretation of this dependence (apart from the fact that this is a classical cosmological test) can yield important information about the evolution of galaxy properties (Gardner 1998).

In Fig. 4, the observed colors of our field galaxies are plotted against their apparent magnitude. The figure clearly shows a trend well known from previous studies: fainter galaxies have, on average, bluer colors. The dashed lines in the figure indicate similar dependences for the VIRMOS galaxies (McCracken *et al.* 2003) that are in satisfactory agreement with our data.

The agreement between the counts in our field with the data for other deep fields is remarkable, because our field is very small and contains a relatively small number of galaxies. For example, the previously mentioned VIRMOS catalog contains $\approx 10^5$ galaxies; this number exceeds the size of our sample by several hundred. This agreement suggests that our

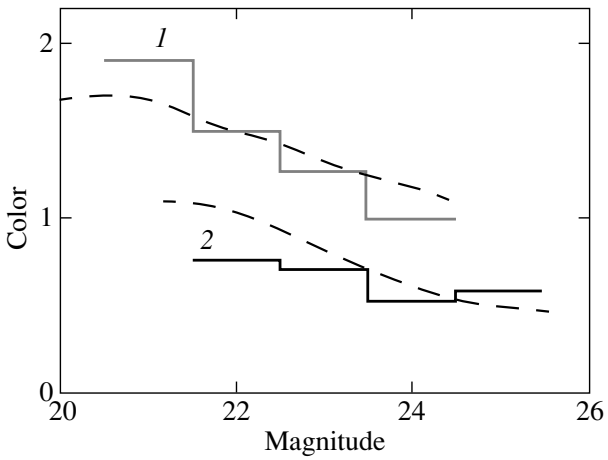

Fig. 4. Mean color index $V-I_c$ for the galaxies of our field versus apparent magnitude I_c (*1*), and color index $B-V$ versus B (*2*). The dashed lines represent similar diagrams for the VIRMOS galaxies (McCracken *et al.* 2003).

field is representative and reflects well the average properties of the galactic population, at least up to $z \sim 1$.

The z Distribution

Figure 5a shows the redshift distribution of the catalogued galaxies. This distribution exhibits a peak at $z = 0.2$–0.3 and a long, gently sloping tail up to $z = 1.3$. The z distribution of the galaxies is distorted by selection effects. One of the strongest selection effects is our requirement that the signal-to-noise ratio for an object be larger than five in all four bands. As a result of this condition, such objects were mostly detected at a relatively low z because of the decline in the spectral energy distribution of early-type galaxies at short wavelengths. This effect is clearly seen from Fig. 5a, where the dashed and heavy solid lines indicate the distributions of E–Sa and Sc–Im galaxies, respectively.

Figure 5b shows the distribution of the catalogued galaxies in the "absolute magnitude B ($M(B)$)—redshift" plane. The galaxy distribution in this plane is also determined by selection effects; we extract mostly luminous objects among the more distant objects. As an example, the dashed line in the figure indicates the selection curve for an Sc spiral galaxy with the apparent magnitude $B = 26$ (the observed magnitude distorted by the k-correction). If all of the galaxies of this type brighter than 26^m were included in our sample of objects, they would lie below the dashed line in the figure. The fainter galaxies with $B > 26$ would lie above this line. Clearly, the magnitude limitation explains well the galaxy distribution in the $M(B)$–z plane.

The strong selection in absolute magnitude in our sample makes it difficult to directly compare the parameters of nearby and distant galaxies. However, if we restrict our analysis only to luminous objects (say, with $M(B) < -18$), then the selection effect is weaker for them, and such galaxies are confidently extracted up to the limiting z of our sample (Fig. 5). Spiral and starburst galaxies dominate (≈90%) in this sample.

Figure 6 shows variations in the angular sizes (the FWHM corrected for the FWHM of the stars) of luminous ($M(B) < -18$) galaxies in the R_c band (the seeing was best during observations in this band). Note that the FWHM values depend on the cosmological decline in brightness much less strongly than do the isophotal diameters. Therefore, they may be used as rough estimates of the galaxy sizes. The barred circles in Fig. 6 represent the mean values and the corresponding dispersions for the redshift ranges 0–0.5, 0.5–1.0, and 1.0–1.3, while the dashed lines indicate the lines of constant linear sizes (the lower and upper curves correspond to linear sizes of 3 and 15 kpc, respectively). The angular sizes of the extended objects from our sample are located, on average, between the two curves of constant linear sizes. For the luminous galaxies under consideration, the mean FWHM in linear measure changes only slightly with increasing z, and is 8 kpc (the solid curve in Fig. 6). The dotted curve in Fig. 6 indicates the expected variation in the observed angular size of an object 8 kpc in diameter, as predicted by the model by Mao *et al.* (1998) (in this model, the galaxy size varies as $\propto (1+z)^{-1}$). Clearly, our data for the galaxies with $M(B) < -18$ are inconsistent with such a strong evolution of their sizes. This conclusion agrees with the conclusion by Lilly *et al.* (1998) that the linear sizes of large and luminous spiral galaxies change little to $z \sim 1$. A similar conclusion was reached by Simard *et al.* (1999) and Takamiya (1999).

In the redshift range 0.3 to 0.5, where faint and luminous objects are represented almost equally, we compared the linear sizes for the galaxies with $M(B) > -18$ and $M(B) < -18$. The luminous ($M(B) \approx -19$) spiral and elliptical galaxies turned out to be a factor of about 1.5 to 2 larger than the fainter ($M(B) \approx -17$) galaxies. The expected change in size for a galaxy with an exponential brightness distribution and a constant central surface brightness is $\Delta \log D \propto 0.2 \Delta M$. Therefore, when the absolute magnitude of a spiral galaxy changes by 2^m, its size will change by a factor of ≈2.5. The observed change in galaxy size is smaller than this estimate, probably because the disks of many distant galaxies are poorly described by an exponential law (Reshetnikov *et al.* 2003).

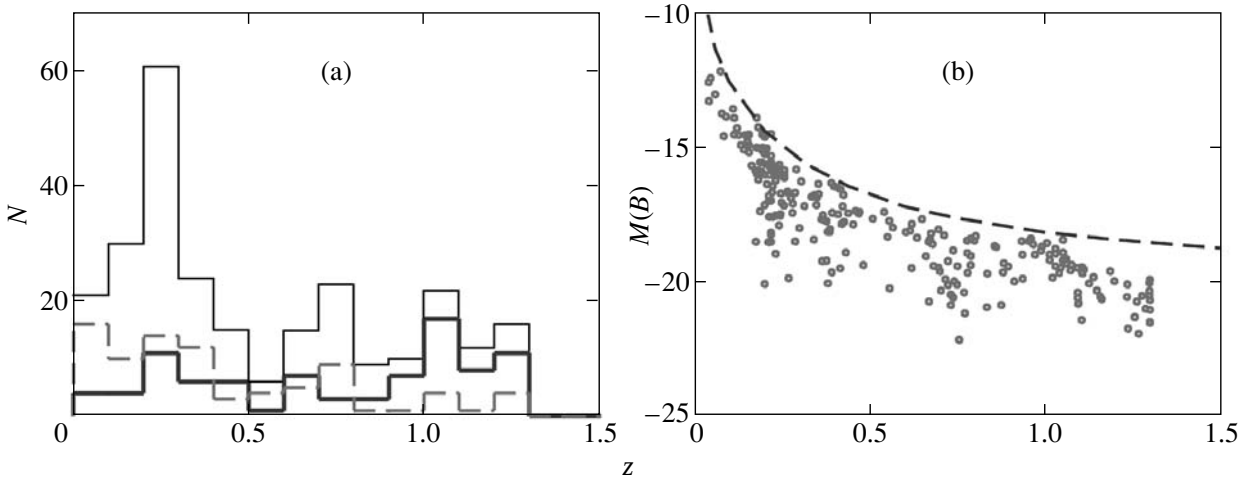

Fig. 5. (a) The z distribution of sample galaxies (thin solid line); the heavy solid and dashed lines indicate the distributions for Sc–Im and E–Sa galaxies, respectively; (b) the absolute magnitude–redshift diagram.

The variation in the observed colors of extended objects with z roughly corresponds to the expected variation for local galaxies at the corresponding z. As an example, Fig. 7 shows the galaxy positions in the two-color diagrams for two redshift ranges. The solid line in each of the panels represents the color sequence for normal galaxies at $z = 0.2$ (a) and $z = 0.8$ (b), as constructed by Fukugita *et al.* (1995). The colors of galaxies at $z = 0.7$–0.9 are in satisfactory agreement with the expected distribution in the two-color diagram (all of the objects in this z range brighter than $M(B) = -18$); the agreement is poorer for $z \approx 0.2$. However, the agreement becomes much better if we consider only the luminous galaxies with $M(B) < -18$ at $z \approx 0.2$ (the crosses in Fig. 7a).

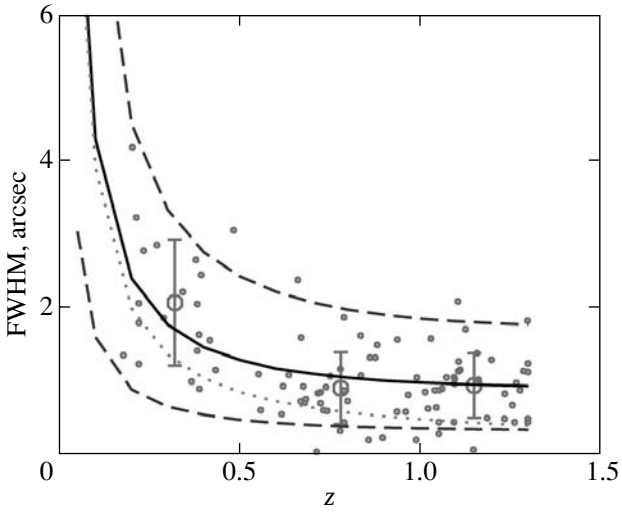

Fig. 6. Galaxy angular size in R_c versus redshift (see the text).

The color variations of Sa–Im spiral galaxies with z are shown in a more detailed form in Figs. 7c and 7d. The solid lines in these figures represent the expected dependences for the accretion model of spiral galaxy formation (Westera *et al.* 2002; Samland and Gerhard 2003). According to Westera *et al.* (2002), the galactic disk is formed inside a dark halo through ongoing external gas accretion. In this model, the star formation rate is a nonmonotonic function of time: it reaches its maximum at $z \approx 1$ and remains significant down to $z = 0$. The dashed lines indicate the dependences for the model of a single collapse. In this scenario, the disk has been formed through the contraction of a protogalactic cloud at $z > 1$. We see from Figs. 7c and 7d that, in general, the accretion model satisfactorily describes the general pattern of variation in the observed colors of galaxies with z. The collapse model is in much poorer agreement with our data, predicting much redder colors at each z.

The Host Galaxy of GRB 000926

What is the host galaxy of the GRB whose region is studied here?[2] The apparent magnitudes of the galaxy corrected for extinction in the Milky Way are $B = 26.01 \pm 0.17$, $V = 25.76 \pm 0.22$, $R_c = 25.88 \pm 0.28$, and $I_c = 24.65 \pm 0.40$ (Fatkhullin 2002); its redshift is $z = 2.0379$ (Castro *et al.* 2003). Given the k-correction for an Sc spiral galaxy (Poggianti 1997), the absolute magnitude of the host galaxy is $M(B) =$

[2] An image of this galaxy and more information can be found at SAO RAS http://www.sao.ru/hq/grb/host-obs.html.

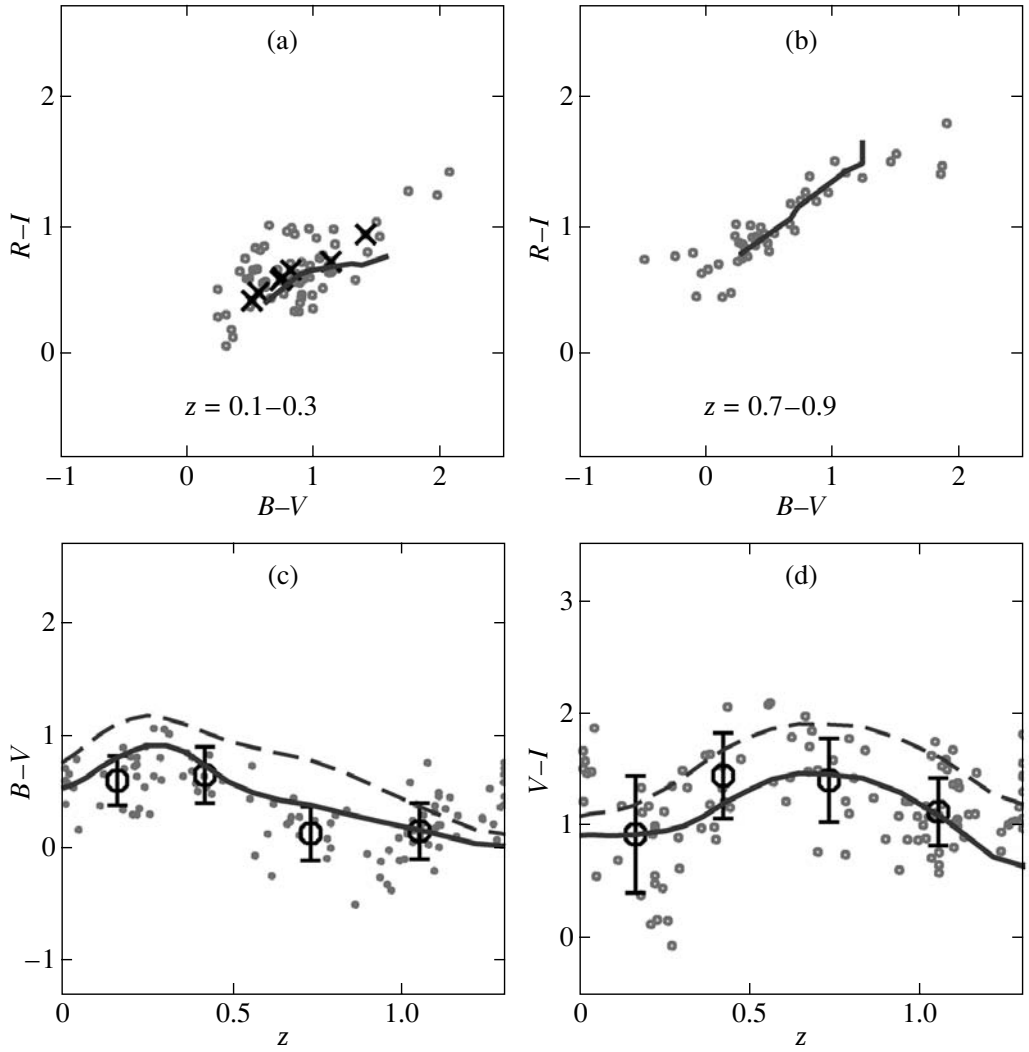

Fig. 7. (a and b) Positions of the sample galaxies in the two-color diagrams for two redshift ranges. The solid lines indicate the corresponding color sequences for normal galaxies (Fukugita *et al.* 1995); the crosses in Fig. 7a mark luminous galaxies with $M(B) < -18$. (c and d) The evolution of the observed colors of spiral galaxies. The barred circles represent the mean color indices in the redshift ranges 0–0.3, 0.3–0.6, 0.6–0.9, and 0.9–1.2. The heavy solid and dashed lines indicate the model dependences for the accretion model of disk galaxy formation and for the model of a single collapse (Westera *et al.* 2002), respectively.

−19.1. Consequently, it is a relatively faint, but not dwarf object. The galaxy mass was roughly estimated by Castro *et al.* (2003) to be $\approx 10^{10} M_\odot$. This value yields an estimate of the mass-to-light ratio $M/L(B) \approx 1.5$ (in solar units), which is typical of objects of late morphological types with violent star formation.

The observed colors of the host galaxy were compared with the colors of faint ($B > 25$) galaxies in this field by Fatkhullin (2002). The galaxy was found to be, on average, bluer than other faint extended objects. This conclusion is also confirmed by a direct comparison of the observed colors for the host galaxy of GRB 000926 with the colors of objects at $z \approx 2$ in our field. Note, however, that, because of observational selection (see Fig. 5), the galaxies that we extracted at $z \approx 2$ are, on average, much more luminous than the host galaxy being discussed. A proper comparison of the colors requires studying the parameters of galaxies at $z \approx 2$ with a luminosity comparable to that of the GRB 000926 host galaxy. Since such objects are located near the magnitude limit of our field, this is very difficult to do using our data. However, certain conclusions can still be reached. That the colors of the host galaxy are bluer than the colors of galaxies at lower z can be explained by the fact that the specific star formation rate in the Universe increases with redshift (see, e.g., Madau *et al.* 1998); hence, bluer

colors are expected, on average, for the galaxies (see, e.g., Fig. 3 from the paper by Rudnik *et al.* 2003). Therefore, the host galaxy may well be a typical spiral galaxy for an epoch of $z \approx 2$. This explanation is consistent with the conclusion previously reached by several authors that the host galaxies of GRBs are normal blue galaxies similar in properties to galaxies at the same redshifts (Sokolov *et al.* 2001; Le Floc'h *et al.* 2003; Djorgovski *et al.* 2003).

CONCLUSIONS

We have presented the results of our detailed photometric study of a small ($3'.6 \times 3'$) region in the field of GRB 000926 (Fig. 1). The observations were carried out on good photometric nights, which allowed us to reach a limiting magnitude of 26.6 in the B band under fairly stringent conditions.

In the field under study, we extracted 264 extended objects and 21 starlike objects. The number of presumed stars agrees with the expected number in Bezanson's Milky Way model. The stellar colors are typical of main sequence dwarfs (Fig. 2).

The differential galaxy counts in the field to $B \approx 25$ are in good (to within 20%) agreement with previous CCD surveys of several deep fields (Fig. 3). We have confirmed the existence of a general tendency in the observed colors of the field galaxies with their apparent magnitude (Fig. 4).

An analysis of the images of luminous ($M(B) < -18$) galaxies has led us to conclude that there is no strong evolution of their linear sizes at $z \leq 1$ (Fig. 6).

In general, the color variations of spiral galaxies with z agree with the predictions of the accretion model, in which galactic disks are formed within dark halos through long-term external gas accretion (Fig. 7).

One of the important results of our study is that in the cases where we can compare our data with previously published data for other (often deeper and larger) fields, they are in good agreement. This implies that investigating relatively small deep fields is a quite efficatious method of studying the evolution of galaxies.

ACKNOWLEDGMENTS

This work was supported by the Federal Astronomy Program (project no. 40.022.1.1.1101) and the Russian Foundation for Basic Research (project nos. 03-02-17152 and 01-02-17106).

REFERENCES

1. S. Arnouts, B. Vandame, C. Benoist, *et al.*, Astron. Astrophys. **379**, 740 (2001).
2. W. Baum, *IAU Symp. 15: Problems of Extragalactic Research* (Macmillan, New York, 1963), p. 390.
3. E. Bertin and S. Arnouts, Astron. Astrophys. **117**, 393 (1996).
4. M. Bessel, Publ. Astron. Soc. Pac. **102**, 1181 (1990).
5. M. Bolzonella, J.-M. Miralles, and R. Pello, Astron. Astrophys. **363**, 476 (2000).
6. D. Calzetti, L. Armus, R. C. Bohlin, *et al.*, Astrophys. J. **533**, 682 (2000).
7. S. Castro, T. Galama, F. Harrison, *et al.*, Astrophys. J. **586**, 128 (2003).
8. S. G. Djorgovski, S. R. Kulkarni, D. A. Frail, *et al.*, Proc. SPIE **4834**, 238 (2003).
9. T. Fatkhullin, Bull. Spec. Astrophys. Obs. **53**, 5 (2002).
10. T. A. Fatkhullin, Candidate's Dissertation (SAO RAS, Nizhnii Arkhyz, 2003); http://www.sao.ru/hq/grb/team/timur/timur.html.
11. H. C. Ferguson, M. Dickinson, and R. Williams, Ann. Rev. Astron. Astrophys. **38**, 667 (2000).
12. M. Fukugita, K. Shimasaku, and T. Ichikawa, Publ. Astron. Soc. Pac. **107**, 945 (1995).
13. J. P. Gardner, Publ. Astron. Soc. Pac. **110**, 291 (1998).
14. M. Giavalisco *et al.* (the GOODS team), astro-ph/0309105 (2003).
15. J. Heidt, I. Appenzeller, A. Gabasch, *et al.*, Astron. Astrophys. **398**, 49 (2003).
16. A. U. Landolt, Astron. J. **104**, 340 (1992).
17. O. Le Fevre, Y. Mellier, H. J. McCracken, *et al.*, astro-ph/0306252 (2003).
18. E. Le Floc'h, P.-A. Duc, I. Mirabel, *et al.*, Astron. Astrophys. **400**, 499 (2003).
19. S. Lilly, D. Schade, R. Ellis, *et al.*, Astrophys. J. **500**, 75 (1998).
20. P. Madau, L. Pozzetti, and M. Dickinson, Astrophys. J. **498**, 106 (1998).
21. T. Maihara, F. Iwamuro, H. Tanabe, *et al.*, Publ. Astron. Soc. Jpn. **53**, 25 (2001).
22. Sh. Mao, H. J. Mo, and S. D. M. White, Mon. Not. R. Astron. Soc. **297**, L71 (1998).
23. H. J. McCracken, M. Radovich, E. Bertin, *et al.*, Astron. Astrophys. **410**, 17 (2003).
24. N. Metcalfe, T. Shanks, A. Campos, *et al.*, Mon. Not. R. Astron. Soc. **323**, 795 (2001).
25. B. M. Poggianti, Astron. Astrophys., Suppl. Ser. **122**, 399 (1997).
26. E. Ramirez-Ruiz, E. Fenimore, and N. Trentham, AIP Conf. Proc. **555**, 457 (2001).
27. V. P. Reshetnikov, R.-J. Dettmar, and F. Combes, Astron. Astrophys. **399**, 879 (2003).
28. A. C. Robin, C. Reyle, and M. Creze, Astron. Astrophys. **359**, 103 (2000).
29. G. Rudnik, H.-W. Rix, M. Franx, *et al.*, astro-ph/0307149 (2003).
30. M. Samland and O. E. Gerhard, Astron. Astrophys. **399**, 961 (2003).

31. L. Simard, D. C. Koo, S. M. Faber, *et al.*, Astrophys. J. **519**, 563 (1999).
32. V. Sokolov, T. Fatkhullin, A. Castro-Tirado, *et al.*, Astron. Astrophys. **372**, 438 (2001).
33. L. S. Sparke and J. S. Gallagher III, *Galaxies in the Universe: An Introduction* (Cambridge Univ. Press, Cambridge, 2000).
34. A. Szalay, A. Connolly, and G. Szokoly, Astron. J. **177**, 68 (1999).
35. M. Takamiya, Astrophys. J., Suppl. Ser. **122**, 109 (1999).
36. N. Trentham, E. Ramirez-Ruiz, and A. Blain, Mon. Not. R. Astron. Soc. **334**, 983 (2002).
37. D. Schlegel, D. Finkbeiner, and M. Davis, Astrophys. J. **500**, 525 (1998).
38. P. Westera, M. Samland, R. Buser, and O. E. Gerhard, Astron. Astrophys. **389**, 761 (2002).

Translated by V. Astakhov

Astronomy Letters, Vol. 30, No. 5, 2004, pp. 293–308. Translated from Pis'ma v Astronomicheskiĭ Zhurnal, Vol. 30, No. 5, 2004, pp. 334–350.

The Light Curve of Supernova 1987A: The Structure of the Presupernova and Radioactive Nickel Mixing

V. P. Utrobin*

Institute for Theoretical and Experimental Physics,
ul. Bol'shaya Cheremushkinskaya 25, Moscow, 117259 Russia
Max-Planck-Institut für Astrophysik, Karl-Schwarzschild-Str. 1, Garching, D-85741 Germany

Received October 9, 2003

Abstract—We have studied the influence of the presupernova structure and the degree of ^{56}Ni mixing on the bolometric light curve of SN 1987A in terms of radiation hydrodynamics in the one-group approximation by abandoning LTE and by taking into account nonthermal ionization and the contribution of spectral lines to its opacity. Our study shows that moderate ^{56}Ni mixing at velocities $\leq$2500 km s^{-1} can explain the observed light curve if the density of the outer layers of the presupernova exceeds the value obtained in the evolutionary model of a single nonrotating star severalfold. Abandoning LTE and allowing for nonthermal ionization when solving the equation of state and calculating the mean opacities and the thermal emission coefficient leads to a significant difference between the gas temperature and the radiation temperature in the optically thin layers of the supernova envelope. We demonstrate the fundamental role of the contribution of spectral lines to the opacity in an expanding envelope and of the accurate description of radiative transfer in reproducing the observed shape of the bolometric light curve. We have found that disregarding the contribution of spectral lines to the opacity introduces an error of $\sim$20% into the explosion energy, and that a similar error is possible when determining the mass of the ejected matter. The resonant scattering of radiation in numerous lines accelerates the outer layers to velocities of $\approx$36 000 km s^{-1}; this additional acceleration affects the outer layers with a mass of $\approx 10^{-6} M_{\odot}$. Proper calculations of the supernova luminosity require that not only the delay effects, but also the limb-darkening effects be taken into account. © *2004 MAIK "Nauka/Interperiodica".*

Key words: *supernovae and supernova remnants.*

INTRODUCTION

Supernova (SN) 1987A, which exploded in the Large Magellanic Cloud (LMC), still provides extensive astrophysical information. Nevertheless, it holds many secrets, offering a unique opportunity to study in depth this grandiose event and the preceding evolution of the exploded star. One of the surprises was the fact that the exploded star (presupernova) turned out to be a blue supergiant rather than a red supergiant, as expected for type-II supernovae with a plateau (SN IIP). The explosion of the blue supergiant confirmed the far-sighted conclusion reached by Shklovsky (1984) several years earlier that, since the irregular galaxies (to which the LMC belongs) are metal-poor, the formation of extended stellar envelopes is hampered in presupernovae; therefore, supernovae with properties similar to those shown by SN 1987A must explode in these galaxies instead of ordinary SN II. Indeed, the underabundance of heavy elements in the LMC matter compared to the cosmic composition favors the formation of blue supergiants (Arnett 1987; Hillebrandt *et al.* 1987). In the case of SN 1987A, however, it cannot explain the high nitrogen abundance that was revealed in the circumstellar matter by an analysis of ultraviolet lines (Cassatella 1987; Lundqvist and Fransson 1996). In addition to standard assumptions, either a modification of convective mixing through the meridional circulation induced by rotation of the star during its evolution (Weiss *et al.* 1988), or limited semiconvection at a low abundance of heavy elements (Woosley *et al.* 1988), or invoking evolutionary effects in a close binary system (Podsiadlowski and Joss 1989; Hillebrandt and Meyer 1989) is required to interpret these two facts in evolutionary calculations.

All of these possibilities were equally promising until the ESO ground-based New Technology Telescope (Wampler *et al.* 1990) and the NASA/ESA Hubble Space Telescope (Jakobsen *et al.* 1991) discovered intricate ring structures around SN 1987A. The existence of these structures imposes severe constraints on the pattern of evolution of the presuperno-

*E-mail: utrobin@itep.ru

va, necessitating deviations from spherical symmetry, at least shortly before the supernova explosion. For a single star, this suggests at least including rotation effects. However, including these effects and using new OPAL opacities has not freed the evolutionary calculations from problems in explaining the observed properties of the presupernova, requiring a more thorough development of the physics of rotating stars and convective mixing (Woosley *et al.* 1997). In contrast, the evolution of stars in a close binary is so rich in possibilities that it admits not only the model of accretion of a substantial amount of matter from the secondary component onto the presupernova, but also the model of a complete merger with it (Podsiadlowski 1992).

Since the structure of the presupernova and the chemical composition of its outer layers (which are unaffected by explosive nucleosynthesis, being the end result of the entire evolution of the star) in many respects determine the pattern of supernovae explosion, the incompleteness of the picture outlined above and the absence of decisive arguments for a particular evolutionary scenario of the presupernova prompt us to analyze the light curve of SN 1987A once again. Interest is also stirred by the fact that the light curve is shaped mainly by radioactive decays of ^{56}Ni and ^{56}Co whose distribution in the supernovae envelope is a clear trace left by the explosion mechanism. The hydrodynamic models of SN 1987A based on evolutionary calculations of the presupernova necessitated strong ^{56}Ni mixing up to velocities of $\sim$4000 km s^{-1} to reproduce the observed bolometric light curve (Woosley 1988; Shigeyama and Nomoto 1990; Blinnikov *et al.* 2000). On the other hand, the hydrodynamic modeling of the SN 1987A explosion that uses nonevolutionary presupernova models and that proceeds from the best agreement with observations has shown the possibility of moderate ^{56}Ni mixing up to velocities of $\sim$2000 km s^{-1} (Utrobin 1993). Note that Blinnikov *et al.* (2000) not only solved the system of radiation hydrodynamics equations in the multigroup approximation, but also took into account the contribution of spectral lines to the opacity, while other researchers restricted their analyses to the simple approximation of radiative heat conduction.

Our goal here is to investigate the influence of the presupernova structure and the degree of ^{56}Ni mixing on the bolometric light curve of SN 1987A in terms of radiation hydrodynamics in the one-group approximation by abandoning local thermodynamic equilibrium (LTE) and by taking into account nonthermal ionization and the contribution of spectral lines to the opacity. Our results have confirmed the previous conclusions listed above, provided that the density of the outer layers of the nonevolutionary presupernova model is several times higher than the density in the evolutionary model of a single nonrotating star. We give the system of radiation hydrodynamics equations in the one-group approximation with the equation of state for an ideal gas in a nonequilibrium radiation field and for nonthermal ionization with appropriate mean opacities and thermal emission coefficient. We describe the numerical method for solving this system of equations and consider the hydrodynamic models studied. We compare the evolutionary and nonevolutionary presupernova models, analyze the behavior of the gas temperature and the radiation temperature in the supernova envelope, and study the role of nonthermal ionization, the contribution of spectral lines to the opacity, limb-darkening effects, and the chemical composition of the surface layers in the supernova explosion. In conclusion, we discuss our results and their possible implications.

RADIATION HYDRODYNAMICS

The CRAB software package has been developed for hydrodynamic studies of supernovae. This package models an unsteady one-dimensional spherically symmetric gas flow in the fields of gravity and nonstationary nonequilibrium radiation in Lagrangian variables. The time-dependent radiative transfer equation, written in a comoving frame of reference to within terms on the order of the ratio of the matter velocity to the speed of light, can be solved as a system of equations for the zeroth and first moments of the radiation intensity in angular variable. To close this system of moment equations, we use a variable Eddington factor that can be calculated by directly taking into account the scattering of radiation in the medium. The satisfaction of the LTE conditions when solving the equation of state and determining the mean opacities and the thermal emission coefficient is not assumed. In the inner, optically thick layers of the supernova envelope where thermalization takes place, the diffusion of equilibrium radiation is described in the approximation of radiative heat conduction. We have performed our study with a simplified version of radiation hydrodynamics in the one-group (gray) approximation, in which the nonequilibrium radiation field can be parametrized by an appropriate blackbody temperature.

Radiation Hydrodynamics in the One-Group Approximation

According to Mihalas and Mihalas (1984),[1] the system of radiation hydrodynamics equations in the

[1] See also an independent derivation of the ensuing equations by Imshennik (1993) based on the book by Imshennik and Morozov (1981).

one-group approximation comprises the following: the continuity equation

$$\frac{\partial r}{\partial t} = u, \quad \frac{\partial r}{\partial m} = \frac{1}{4\pi r^2 \rho}, \tag{1}$$

the equation of motion

$$\frac{\partial u}{\partial t} = -4\pi r^2 \frac{\partial (P_g + Q)}{\partial m} - \frac{Gm}{r^2} + \frac{1}{c}\chi_F^0 F^0, \tag{2}$$

the energy equation for the gas

$$\frac{\partial E_g}{\partial t} = -(P_g + Q)\frac{\partial}{\partial t}\left(\frac{1}{\rho}\right) + c\kappa_E^0 E^0 - 4\pi\frac{\eta_t^0}{\rho} + \varepsilon, \tag{3}$$

the equation for the total radiative energy density

$$\frac{\partial E^0}{\partial t} = -4\pi\rho\frac{\partial}{\partial m}(r^2 F^0) - 4\pi\rho(1 + f^0) \tag{4}$$
$$\times E^0 \frac{\partial}{\partial m}(r^2 u) + \frac{u}{r}(3f^0 - 1)E^0 + 4\pi\eta_t^0 - c\rho\kappa_E^0 E^0,$$

and the equation for the total radiative energy flux

$$\frac{\partial F^0}{\partial t} = \left(2\frac{u}{r} - c\rho\chi_F^0 - 8\pi\rho\frac{\partial}{\partial m}(r^2 u)\right)F^0 \tag{5}$$
$$- c^2\left(4\pi r^2\rho\frac{\partial}{\partial m}(f^0 E^0) + \frac{1}{r}(3f^0 - 1)E^0\right).$$

Here, t is the time in the comoving frame of reference; m is the mass of the gas within the sphere of radius r; u is the gas velocity; ρ is the gas density; P_g and E_g are the pressure and specific internal energy of the gas, respectively; Q is the artificial viscosity; E^0 is the total radiative energy density related to the radiation temperature T_r by $E^0 = aT_r^4$; F^0 is the total radiative energy flux; χ_F^0 is the mean opacity weighted in radiative energy flux (true absorption and scattering); κ_E^0 is the mean opacity weighted in radiative energy density (true absorption); η_t^0 is the total thermal emission coefficient; ε is the rate of change in internal energy, for example, due to the deposition of gamma rays produced by radioactive decays; f^0 is the variable Eddington factor equal to the ratio of the radiation pressure P_r^0 to the total radiative energy density E^0. The radiation characteristics, the mean opacities, and the thermal emission coefficient refer to the comoving frame of reference and are denoted by the superscript 0.

Initial data and boundary conditions must be specified to properly formulate the problem of radiation hydrodynamics described by hyperbolic equations: the radius r, the velocity u, and the total radiative energy flux F^0 at the inner boundary and the total radiative energy flux F^0 and a zero gas pressure ($P_g = 0$) at the outer boundary.

Ionization Balance and the Equation of State

If the stationarity condition is satisfied, the equation of state for an ideal gas in a nonequilibrium radiation field and for nonthermal ionization requires solving the problem of the populations of excited atomic and ionic levels and the ionization balance. In the absence of LTE, the distribution in excited atomic and ionic levels and in ionization states is determined by the balance of all possible elementary processes, and the general solution of the problem must include an infinite system of algebraic equations for the entire set of levels and processes. This is a very complicated problem because of both the mathematical difficulties and the lack of reliable physical data on the required elementary processes. This circumstance and the necessity of multiple calculations of the equation of state in hydrodynamic calculations force us to disregard the excited atomic and ionic levels and to restrict our analysis only to the ground atomic and ionic states and, hence, to their ionization balance. Of greatest interest in the establishment of ionization balance in supernova envelopes are the following elementary processes: photoionization and radiative recombination, electron ionization, three-particle recombination, and nonthermal ionization.

To simplify the system of balance equations, we take into account only three ionization states for all elements. The ionization balance equation for a Z^0 atom and a Z^+ ion in which the photoionization, electron ionization, and nonthermal ionization rates are balanced out by the radiative and three-particle recombination rates is

$$R_{Z^0}N_{Z^0} + q_{Z^0}N_e N_{Z^0} + \Gamma_{Z^0}N_{Z^0} = \alpha_{Z^+}N_e N_{Z^+} + \chi_{Z^+}N_e^2 N_{Z^+}, \tag{6}$$

where R_{Z^0} is the photoionization probability of the Z^0 atom in a radiation field that is not necessarily in equilibrium; α_{Z^+} is the radiative recombination coefficient; q_{Z^0} is the electron ionization rate for the Z^0 atom for a Maxwellian energy distribution; χ_{Z^+} is the coefficient of the corresponding three-particle recombination; Γ_{Z^0} is the nonthermal ionization rate for the Z^0 atom; and N_e, N_{Z^0}, and N_{Z^+} are the number densities of the electrons, Z^0 atoms, and Z^+ ions, respectively. A similar equation can also be written for the Z^+ and Z^{++} ions and for hydrogen, the only difference being that the negative hydrogen ion will act as the third ionization state.

The analytic fits to the cross sections for photoionization from the ground state for various atoms and ions required to calculate the photoionization probability and the radiative recombination coefficient were taken from the papers by Verner and

Yakovlev (1995) and Verner *et al.* (1996). The photoionization cross section for the negative hydrogen ion was calculated by Wishart (1979). The fitting formulas for the electron ionization rates of various atoms and ions are given in the paper by Voronov (1997). The radioactive nuclides produced by explosive nucleosynthesis emit mostly gamma rays with an energy of about 1 MeV, which lose their energy through Compton scattering by free and bound electrons. In turn, the Compton electrons lose their energy through the heating of free electrons and the ionization and excitation of atoms and ions. Kozma and Fransson (1992) accurately solved this complicated problem and calculated the nonthermal ionization and excitation rates for atoms and ions.

Now, to find the ionization balance for a mixture of chemical elements, for example, composed of H and elements from He to Fe, we close the system of balance equations described above by the equations for the conservation of the number of particles and electrical plasma neutrality. Given the gas density, the electron temperature, the nonequilibrium radiation and nonthermal ionization properties, and the parameters of the elementary processes, the derived system of equations can be easily reduced to a nonlinear equation for the unknown degree of ionization x_e. Note that the physical conditions in the supernova envelope at the expansion phase concerned are characterized by the equality between the electron and ion temperatures, which are designated as the gas temperature T_g. Solving this equation for the degree of ionization x_e yields all of the required relative atomic and ionic number densities x_{H^0}, x_{H^+}, x_{H^-}, x_{Z^0}, x_{Z^+}, and $x_{Z^{++}}$.

The pressure P_g and the internal energy E_g of an ideal gas in the equation of state for a mixture of chemical elements are

$$P_g = \frac{kT_g}{m_u A}(1 + Ax_e)\rho, \tag{7}$$

$$E_g = \frac{3}{2}\frac{kT_g}{m_u A}(1 + Ax_e) + \frac{X_H}{m_u A_H}\left(I_H x_{H^+} - I_{H^-}x_{H^-}\right) + \sum_{Z=He}^{Fe}\frac{X_Z}{m_u A_Z}\left(I_{Z^0}x_{Z^+} + \left(I_{Z^0} + I_{Z^+}\right)x_{Z^{++}}\right), \tag{8}$$

where X_Z is the mass fraction of the Z element; A_Z is the atomic mass of the Z element (AMU); I_{Z^0} and I_{Z^+} are the ionization potentials for the Z^0 atom and the Z^+ ion, respectively; and A is the mean atomic mass (AMU) defined by the identity

$$\frac{1}{A} = \frac{X_H}{A_H} + \sum_{Z=He}^{Fe}\frac{X_Z}{A_Z}. \tag{9}$$

The ionization balance and the equation of state were considered in more detail previously (Utrobin 1998).

The Mean Opacities and the Emission Coefficient

The relative atomic and ionic number densities that were calculated, as described above, in the absence of LTE, but without allowing for any excited states, determine the corresponding mean opacities and the thermal emission coefficient. As the mean opacity χ_F^0 weighted in radiative energy flux, we use the Rosseland mean that includes the contributions both from bound–free and free–free absorption and from Thomson scattering by free electrons and Rayleigh scattering by neutral hydrogen. The mean opacity κ_E^0 weighted in radiative energy density is calculated as the Planck mean with a radiation temperature T_r that includes only the contributions from bound–free and free–free absorption. Accordingly, the total spontaneous thermal emission coefficient η_t^0 includes bound–free and free–free processes. The free–free absorption by atoms and ions was calculated using the Gaunt factor (tabulated by Sutherland 1998) averaged over the Maxwellian distribution, and the free–free absorption coefficient for the negative hydrogen ion was taken from the paper by Bell and Berrington (1987).

Apart from the processes in the continuum, we also took into account the contribution of bound–bound processes to the opacity. Slightly more than 500 000 spectral lines were chosen from the extensive atomic line database compiled by Kurucz and Bell (1995). To calculate the corresponding opacity, we solved the special problem of the populations of excited atomic and ionic levels and the ionization balance for a mixture of chemical elements from H to Zn with all ionization stages at given density and temperature using the Boltzmann and Saha formulas. We averaged the contribution of spectral lines in a medium with a velocity gradient using the generalized formula by Castor *et al.* (1975) at the early expansion phases of the supernova envelope and using the formula by Blinnikov (1996) after the passage to free expansion. The line opacity in an expanding medium calculated in this way was treated as pure scattering.

The Numerical Method

We used the standard method of lines (see, e.g., Berezin and Zhidkov 1962; Blinnikov and Bartunov 1993) to numerically solve the system of radiation hydrodynamics equations (1)–(5). The essence

of this method is that the system of partial differential equations is reduced to a system of ordinary differential equations by an appropriate substitution of finite-difference fits for the derivatives with respect to the spatial coordinates. In all of the computed models, we broke the star down into 300 computational mass bins. The derived system of ordinary differential equations is stiff, but there are well-developed algorithms for its integration. One of the most efficient methods is the implicit method by Gear (1971) with an automatic choice of both the time integration step and the order of accuracy of the method. The implementation of Gear's method involves calculating the corresponding Jacobi matrix and inverting the large and sparse matrix derived from it. Zlatev's efficient algorithm (Österby and Zlatev 1983) that was specially modified by Blinnikov and Bartunov (1993) was used to invert such a large and sparse matrix of arbitrary structure.

The system of time-dependent frequency-integrated moment equations—the equation for the total radiative energy density (4) and the equation for the total radiative energy flux (5)—is closed by introducing a variable Eddington factor f^0. The latter can be determined by solving the time-independent transfer equation for a spherically symmetric expanding medium (Mihalas and Mihalas 1984) written simultaneously in the laboratory and comoving frames of reference to within terms on the order of u/c,

$$\mu\frac{\partial I}{\partial r}+\frac{1-\mu^2}{r}\frac{\partial I}{\partial \mu}=\left(1-\mu\frac{u}{c}\right)\rho(\kappa_a^0+\kappa_s^0)(S-I), \tag{10}$$

with the source function that explicitly includes the contribution of scattering,

$$S=\left(1+5\mu\frac{u}{c}\right)\frac{\eta_t^0/\rho+\kappa_s^0 J^0}{\kappa_a^0+\kappa_s^0}, \tag{11}$$

where $\mu=\cos\theta$ and θ is the angle between the direction of propagation of the radiation and the radius vector $\mathbf{r}$. The frequency-integrated specific radiation intensity I refers to the laboratory frame of reference, while the frequency-integrated mean radiation intensity J^0, the opacity of true absorption κ_a^0, and the opacity of scattering κ_s^0 are calculated in the comoving frame of reference and are denoted by the superscript 0. The formal solution along the characteristics (individual rays) in the absence of externally incident radiation on the outer boundary is used in solving the transfer equation (10). The frequency-integrated moments of the radiation intensity are transformed from the laboratory frame to the comoving frame using the Lorenz transformations (Mihalas and Mihalas 1984), and the corresponding Eddington factor f^0 is then calculated. In addition, the solution obtained allows us to also calculate the variable Eddington factor at the outer boundary, which relates the total radiative energy flux to the mean frequency-integrated radiation intensity.

The bolometric luminosity calculated by taking into account the delay and limb-darkening effects is given by the formula

$$L(t_{\rm obs})=\int_0^1 4\pi R^2(t)\pi I(R(t),\mu)2\mu d\mu, \tag{12}$$

where $t_{\rm obs}$ is the time in the observer's frame of reference; $R(t)$ is the outer radius of the supernova envelope at time t; $I(R(t),\mu)$ is the specific radiation intensity at the outer boundary of the envelope at the same time derived from the solution of the transfer equation (10) with the angular dependence and with the appropriate source function (11). It would be natural to measure the time $t_{\rm obs}$ from the detection time of the neutrino signal that emerges during the supernova explosion and that reaches an observer at distance D in time D/c. In this case, the relation between the times $t_{\rm obs}$ and t is given by

$$t_{\rm obs}=t-\frac{R(t)\mu}{c}. \tag{13}$$

The deposition of gamma rays produced by radioactive ^{56}Ni and ^{56}Co decays can be determined from the solution of the gamma-ray transfer problem by assuming that the gamma rays interact with matter through absorption at opacity $\kappa_\gamma=0.06Y_e$ cm^2 g^{-1}, where Y_e is the number of electrons per baryon. The gamma-ray transfer was modeled by the transfer equation (10) with appropriate opacity κ_γ and source function.

HYDRODYNAMIC MODELS

First, recall that the presupernova is Sanduleak $-69°202$, a blue B3 Ia supergiant (Gilmozzi *et al.* 1987; Panagia *et al.* 1987; Sonneborn *et al.* 1987) with an apparent magnitude of $12^m.24$ (Rousseau *et al.* 1978), an effective temperature of about 16 300 K, and a bolometric correction of about -1.15 (Humphreys and McElroy 1984). At the distance modulus $m-M=18.5$ for the LMC, the color excess $E(B-V)=0.15$, and the interstellar extinction $A_V=3.1E(B-V)$ (Pun *et al.* 1995), the radius of the blue supergiant is about $46.8R_\odot$. We take this value as the presupernova radius R_0.

Important information about the chemical composition of the surface layers in the presupernova can be obtained by analyzing the spectra of its circumstellar matter. Studying emission lines from the circumstellar matter around SN 1987A, Wang (1991) estimated the ratio $n(\mathrm{He})/n(\mathrm{H})\sim 0.20$. Investigating narrow

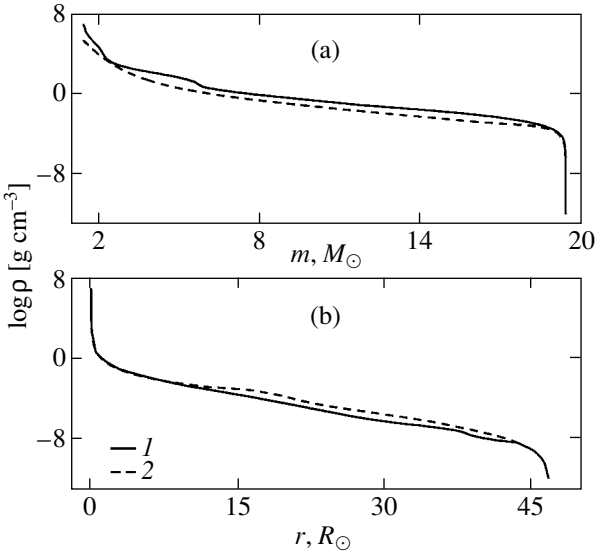

Fig. 1. Initial density distributions in mass (a) and radius (b) for the evolutionary model E (*1*) and the nonevolutionary model N (*2*).

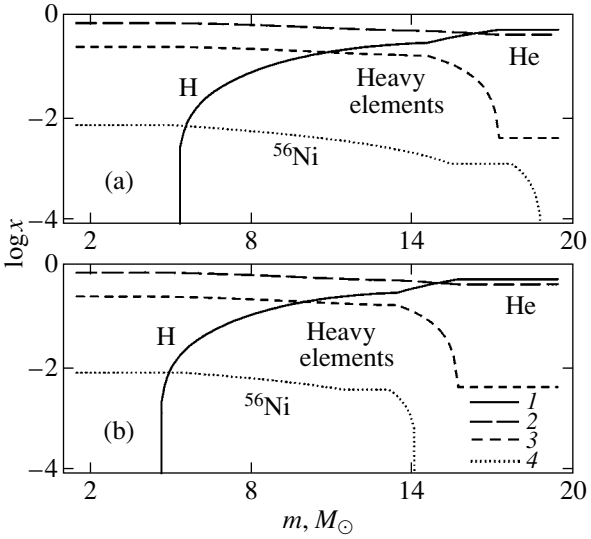

Fig. 2. Chemical composition of the evolutionary model E (a) and the nonevolutionary model N (b): *1*—hydrogen mass fraction, *2*—helium mass fraction, *3*—heavy-element mass fraction, *4*—^{56}Ni mass fraction.

ultraviolet and optical emission lines from the inner circumstellar ring around SN 1987A, Lundqvist and Fransson (1996) obtained $n(\mathrm{He})/n(\mathrm{H}) \sim 0.25$. Being aware of the uncertainty in these estimates, we take a ratio of 0.20. This value together with the data by Dufour (1984) on the metallicity in the LMC yields a relative mass fraction of $X = 0.555$ for hydrogen, $Y = 0.441$ for helium, and $Z = 0.004$ for heavy elements. We take this chemical composition as the chemical composition of the surface layers in the presupernova. According to Dufour (1984), a chemical composition with $X = 0.743$, $Y = 0.251$, and $Z = 0.006$ is characteristic of the LMC.

Here, we investigate the evolutionary and nonevolutionary models of the presupernova. The evolutionary models were constructed from model l20n2ae that was computed by Woosley *et al.* (1997) without allowing for mass loss and rotation and with a collapsing core mass of $1.58M_\odot$, a helium core mass of $5.85M_\odot$, an ejected envelope mass of $17.80M_\odot$, a total mass of $19.38M_\odot$, and an outer radius of $64.2R_\odot$. For convenience and agreement with observations of the presupernova, model l20n2ae was rescaled to a hydrostatic presupernova model with the ejected envelope mass $M_{\mathrm{env}} = 18.0M_\odot$, the total mass $M = 19.58M_\odot$, and the initial radius $R_0 = 46.8R_\odot$; the outer layers were broken down into smaller computational mass bins that were in both hydrostatic and radiative equilibrium at the observed presupernova bolometric luminosity of $-8^m\!.12$. Strictly speaking, after this restructuring and after specifying a chemical composition of the outer layers identical to the observed presupernova composition, the model can hardly be called evolutionary. Nevertheless, a very important property of the evolutionary model l20n2ae, the pattern of density distribution at the explosion time (Fig. 1), is preserved. Below, we denote these models by the letter E.

The nonevolutionary presupernova models have the same ejected envelope mass M_{env}, total mass M, and initial radius R_0 as the evolutionary models, but differ from them in initial density distribution (Fig. 1). The latter is chosen from the condition of good agreement between the computed and observed bolometric light curves for moderate ^{56}Ni mixing, by analogy with the construction of the previous hydrodynamic model for SN 1987A (Utrobin 1993). Just as in the evolutionary presupernova models, the outer layers of the nonevolutionary models are in hydrostatic and radiative equilibrium at the observed presupernova bolometric luminosity and have the observed chemical composition of the presupernova, unless specified otherwise, while the inner layers have the chemical composition of model l20n2ae (Fig. 2). We denote these models by the letter N.

The supernova explosion is triggered by an instantaneous energy release near the stellar center at the initial time. The explosion energy E is specified as the excess above the total energy of the initial envelope configuration. In all of the models under consideration, except for the specially specified ones, the mass of the radioactive nickel nuclide M_{Ni} is $0.073M_\odot$. Basic parameters of the computed hydrodynamic models are given in the table. Apart from the basic models E and N and the similar models Enn

Parameters of the hydrodynamic models

Model	M_{env}, $M_\odot$	R_0, $R_\odot$	E, 10^{51} erg	M_{Ni}, $M_\odot$	Note
E	18	46.8	1.0	0.073	–
Eni	18	46.8	1.0	0.073	^{56}Ni profile, as in model N
Enn	18	46.8	1.0	0	Without ^{56}Ni
N	18	46.8	1.0	0.073	–
Nnn	18	46.8	1.0	0	Without ^{56}Ni
Nnt	18	46.8	1.0	0.073	Without nonthermal ionization
Nlo	18	46.8	1.0	0.073	Without line opacity
Nld	18	46.8	1.0	0.073	Without limb darkening
Ncc	18	46.8	1.0	0.073	LMC chemical composition
Nce	18	46.8	1.2	0.073	LMC chemical composition

and Nnn, but without ^{56}Ni, we present the following: model Eni shows moderate ^{56}Ni mixing in the evolutionary model; model Nnt was computed without including nonthermal ionization; model Nlo shows the role of line opacity in the expanding medium; model Nld indicates the importance of limb darkening in calculating the emergent flux from the supernova envelope; models Ncc and Nce have a chemical composition of the surface layers characteristic of the LMC.

RESULTS

The Evolutionary and Nonevolutionary Presupernova Models

Woosley (1988), Shigeyama and Nomoto (1990), and Blinnikov *et al.* (2000) have convincingly shown that in the explosion of the presupernova model obtained through evolutionary calculations, good agreement with the observed bolometric light curve is achieved only under the assumption of strong ^{56}Ni

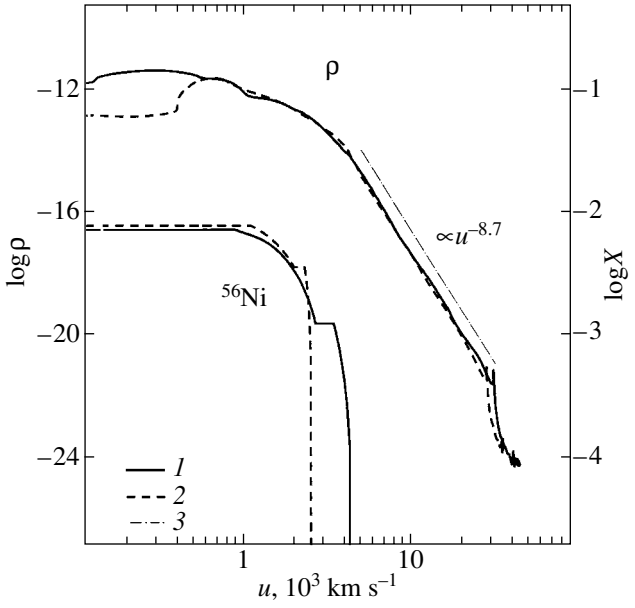

Fig. 3. Behavior of the density and the ^{56}Ni mass fraction in the supernova envelope at time $t = 120$ days: (*1*) model E, (*2*) model N, (*3*) density distribution fit $\rho \propto u^{-8.7}$ in the velocity range 4400–27 000 km s^{-1}.

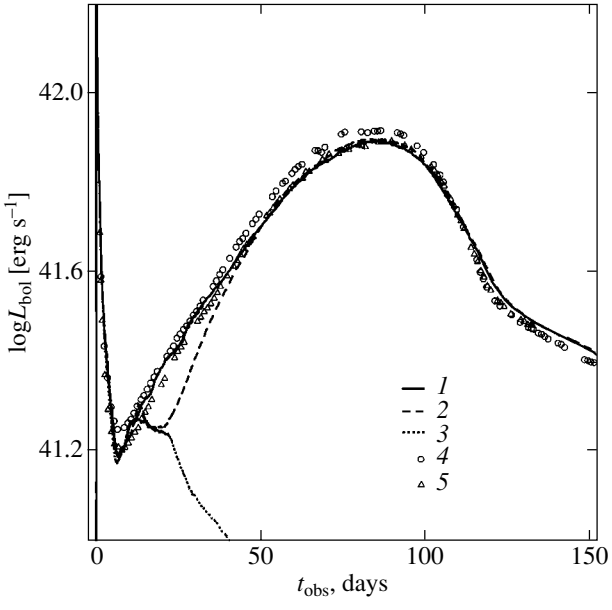

Fig. 4. Bolometric light curves for model E (*1*), model Eni (*2*) (model E with the ^{56}Ni profile in velocity space as in model N), model Enn (*3*) (model E without ^{56}Ni), the observations of SN 1987A (*4*) by Catchpole (1987, 1988), the observational data (*5*) by Hamuy *et al.* (1988).

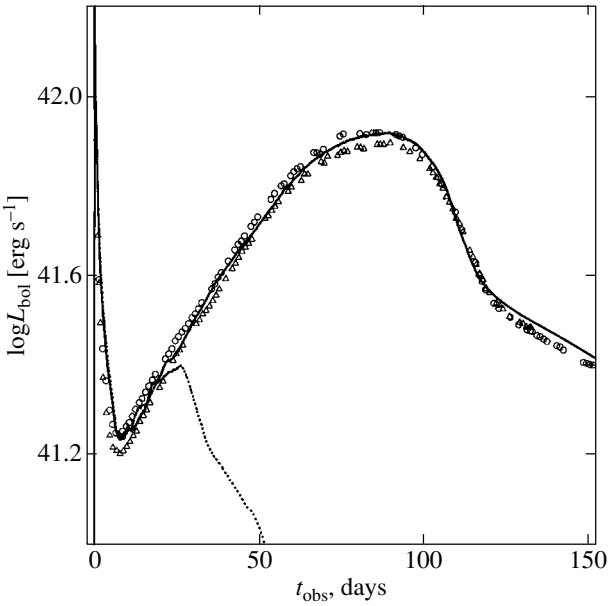

Fig. 5. Same as Fig. 4 for model N (solid line) and model Nnn—model N without ^{56}Ni (dotted line).

mixing up to velocities of ~4000 km s^{-1}. Indeed, moderate (at velocities $u \leq 2500$ km s^{-1}) ^{56}Ni mixing in the evolutionary model Eni similar to the mixing in the nonevolutionary model N (Fig. 3) gives rise to a local minimum in the light curve in the interval 15–30 days (Fig. 4). In the evolutionary model, this deficit of bolometric luminosity, as was pointed out above, can be removed only through strong ^{56}Ni mixing, which is demonstrated by model E (Figs. 3 and 4).

The local minimum of the bolometric luminosity in the evolutionary model Eni arises as follows: Energy release in the central regions of the presupernova gives rise to a strong shock that propagates toward the stellar surface. After the shock passage through the star, the matter heats up, and the radiative energy density increases. Concurrently, the matter acquires an outward-increasing velocity that everywhere exceeds the local parabolic velocity. In about 0.0823 days, the shock emerges on the surface and heats the outer stellar layers—the effective temperature rises to $\sim 4.6\times10^5$ K, the color temperature rises to $\sim 1.1\times10^6$ K, and the luminosity increases sharply. After the emergence of the shock, an expansion of the star begins; this expansion leads to rapid cooling of the surface layers and to the same rapid decrease in luminosity. As a result, a narrow peak is formed whose luminosity at maximum is $\sim 3.5\times10^{44}$ erg s^{-1} and which is partially shown in the bolometric light curve (Fig. 4).

The subsequent expansion of the envelope gradually creates conditions under which a special radiative cooling regime of the matter arises—a cooling wave (CW). Remarkably, even the first hydrodynamic models of supernovae constructed and studied by Imshennik and Nadyozhin (1964) revealed this cooling regime for compact presupernovae, to which the case of SN 1987A belongs. The CW properties were studied in more detail by Grassberg and Nadyozhin (1976). After about 10 days, this regime for the ejected matter completely determines the supernova luminosity; the photosphere is located within the CW front, and the subphotospheric, optically thick layers are cooled almost adiabatically. In the absence of ^{56}Ni in the supernova envelope, the internal energy of the matter and the radiative energy stored in these layers after the shock passage and then partially lost during expansion continue to radiate away for a relatively short period. In the evolutionary model Enn, which is similar to E and which contains no ^{56}Ni in the envelope, the supernova luminosity begins to decrease already after ~13 days, and the energy store in the envelope is depleted by ~40 days (Fig. 4).

Clearly, if ^{56}Ni is distributed in the deep layers whose time of gamma-ray diffusion remains larger than the characteristic envelope expansion time for a long period, then the gamma-ray diffusion begins to be involved in shaping the light curve with a long delay when the luminosity already begins to fall; as a result, a local minimum of the bolometric luminosity is formed. Moderate ^{56}Ni mixing in the evolutionary model Eni has the property described above (Fig. 4). To obtain a monotonic light curve without any local minimum of the bolometric luminosity in the interval 15–30 days, the following simple solution suggests itself: strong ^{56}Ni mixing up to velocities of ~4000 km s^{-1} at which the local gamma-ray deposition compensates for the energy loss through envelope expansion and prevents the undesirable decrease in luminosity. This effect, which is demonstrated by model E (Fig. 4), helped Woosley (1988), Shigeyama and Nomoto (1990), and Blinnikov *et al.* (2000) to reproduce the observed bolometric light curve in their hydrodynamic calculations.

A more radical method of obtaining a monotonic light curve even at moderate ^{56}Ni mixing is to construct a model of the presupernova with a density of its outer layers much higher than the density in the evolutionary model l20n2ae. In such a presupernova, more internal energy of the matter and more radiative energy is stored in the outer, denser layers after the passage of a strong shock through the envelope; this energy may prove to be enough to maintain the increasing luminosity even after 13 days. A proper density distribution in the now nonevolutionary presupernova model (denoted by the letter N) is obtained from agreement between the theoretical and observed bolometric light curves; the density ratio

in the outer ($15-40R_\odot$) layers lies within the range 2.4–4.9 (Fig. 1). Indeed, this density distribution in the presupernova even without ^{56}Ni in the envelope causes an increase in luminosity until ~25 days, as shown by model Nnn (Fig. 5). Finally, moderate ^{56}Ni mixing in model N (Fig. 3) proves to be enough to explain the observed behavior of the bolometric light curve (Fig. 5), just as in our previous hydrodynamic model (Utrobin 1993).

Both in the evolutionary model E after ~13 days (Fig. 4) and in the nonevolutionary model N after ~25 days (Fig. 5), the subsequent run of the bolometric light curve is entirely determined by gamma-ray energy deposition and by the subsequent reprocessing of this energy by the envelope matter and its reradiation in the form of soft thermal photons. The ascending branch of the light curve and its peak were reconciled with observations by an appropriate specification of the chemical composition in the transition region between the surface layers and the helium core (Fig. 2). Here, the crucial factor is deep hydrogen mixing into the helium core up to velocities of ~980 km s^{-1}. This role of hydrogen mixing in reproducing the bolometric light curve was previously noted by Woosley (1988), Shigeyama and Nomoto (1990), Utrobin (1993), and Blinnikov *et al.* (2000). The quasi-exponential decline in luminosity after the maximum is caused by radioactive decays of ^{56}Ni and ^{56}Co whose mass is $0.073M_\odot$.

The Gas and Radiation Temperature Profiles

According to Eqs. (3) and (4), abandoning LTE when solving the equation of state and determining the mean opacities and the thermal emission coefficient will affect the pattern of energy exchange between matter and radiation. The results of this approach can be best studied from the behavior of the gas temperature and the radiation temperature in the envelope. Using the main model N as an example, let us trace the evolution of the radial distributions of the gas temperature and the radiation temperature in the comoving frame of reference at the most characteristic times shown in Fig. 6. Clearly, from the center to the subphotospheric layers in an optically thick medium under conditions close to LTE, the radiation temperature is virtually equal to the gas temperature (Figs. 6a–6c). This state exists until $t \sim 115$ days. Subsequently, however, the envelope rapidly becomes optically thin, and the gas temperature turns out to be lower than the radiation temperature because of the weakening interaction between matter and radiation against the background of the increasing role of adiabatic losses (Fig. 6d).

In contrast, the gas temperature above the photosphere differs from the radiation temperature even in the initial state due to non-LTE conditions. Subsequently, when the shock emerges on the surface and several days later, this difference gradually increases and then becomes significant (Fig. 6). The bolometric luminosity in the surface layers in the comoving frame of reference is almost constant: $L^0 = 4\pi r^2 \pi F^0 \approx$ const (Fig. 7). This fact may be expressed in the following approximate dependence for the radiation temperature distribution in the outer layers: $T_\mathrm{r} \propto (E^0)^{1/4} \propto (F^0)^{1/4} \propto r^{-1/2}$. However, the high expansion velocity of these layers and the delay effect lead to a deviation from this simple dependence. During the explosion, the bolometric luminosity decreases outward; it "remembers" the earlier and bright phase only after the liminosity peak in the interval $t \approx 120-140$ days and increases toward the envelope surface (Fig. 7). The described behavior of the bolometric luminosity is consistent with the calculations by Blinnikov *et al.* (2000). Accordingly, during the explosion, the radiation temperature curve runs below the fitting straight line (Figs. 6a–6c), except for the interval $t \approx 120-140$ days when the radiation temperature is higher (Fig. 6d).

In turn, the gas temperature in the surface layers in the almost complete absence of interaction between radiation and matter and of any heating sources decreases adiabatically as $T_\mathrm{g} \propto t^{-2}$ (Fig. 6) even since the first days. A "frozen-in" structure, a temperature trace from the thin, dense layer formed when the shock emerges on the presupernova surface, arises at the outer edge of the envelope. The dense layer itself is produced by the transition from the adiabatic regime of propagation of a strong shock in the surface layers to the isothermal regime. This layer was first observed in hydrodynamic models of SN II with extended progenitors similar to supergiants (Grassberg *et al.* 1971). For SN 1987A, Imshennik and Nadyozhin (1988) analytically considered the emergence of a shock wave on the presupernova surface. In the hydrodynamic modeling of SN 1987A, a dense layer is formed only when abandoning the approximation of radiative heat conduction, which is too rough to describe the radiative transfer in the surface layers (Blinnikov and Nadyozhin 1991; Ensman and Burrows 1992; Blinnikov *et al.* 2000). The temperature trace is subsequently observed all of the time (it is not shown in Figs. 6c and 6d). Until $t \sim 115$ days, a transition from the optically thick medium where the gas and radiation are described by a single temperature to the transparent layers where the gas cools down adiabatically occurs in the region between the photosphere and the surface layers. In this case, the complex interaction between the heating and cooling processes in the near-photosphere layer manifests itself in the form of a thin structure in the gas temperature distribution (Figs. 6a, 6c, and 6d).

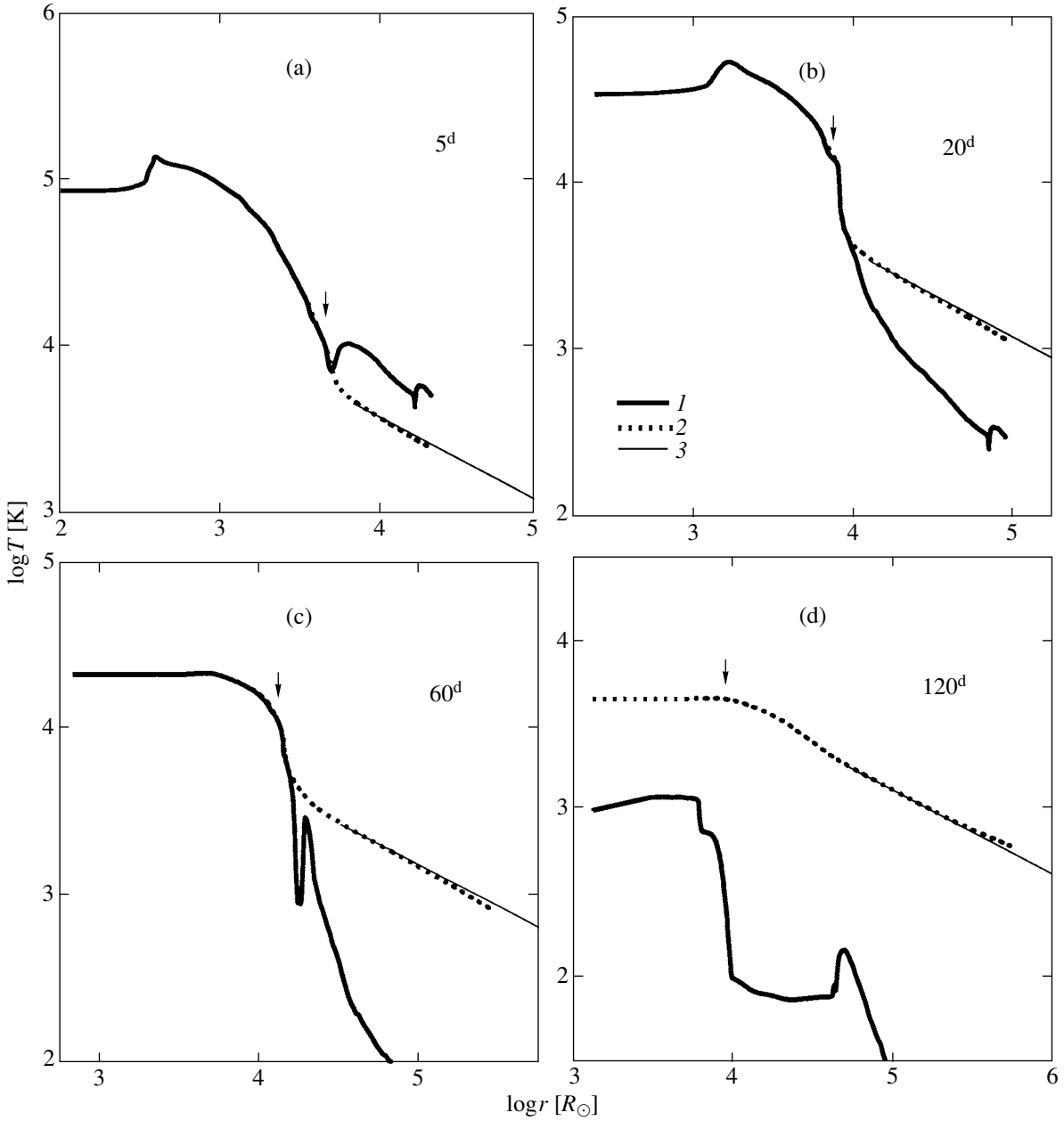

Fig. 6. Evolution of the radial distribution of the gas temperature (*1*) and the radiation temperature (*2*) in the comoving frame of reference in model N: (a) $t = 5$ days, (b) $t = 20$ days, (c) $t = 60$ days, (d) $t = 120$ days; *3*—the fit $T_r \propto r^{-1/2}$ to the radiation temperature distribution under the assumption of constant bolometric luminosity. The vertical arrow marks the location of the photosphere.

The Role of Nonthermal Ionization

After $t_{\rm obs} \sim 30$ days, the luminosity of SN 1987A is produced mainly by ^{56}Ni and ^{56}Co decays, and the pertinent question regarding the role of nonthermal ionization in the supernova explosion arises. To study this question, we computed model Nnt, in which the ionization balance was found without allowing for nonthermal ionization in Eq. (6), but with the energy deposition from radioactive ^{56}Ni and ^{56}Co decays retained in Eq. (3). The bolometric light curve for model Nnt turned out to be almost coincident with that for model N, exhibiting only a small luminosity deficit as the maximum is approached in the interval $t_{\rm obs} \approx 40$–70 days (Fig. 8). This deficit owes its origin to an increase in opacity in the absence of nonthermal ionization. Thus, it should be recognized that nonthermal ionization plays a minor role in shaping the bolometric light curve of SN 1987A. A much larger effect of nonthermal ionization was found in

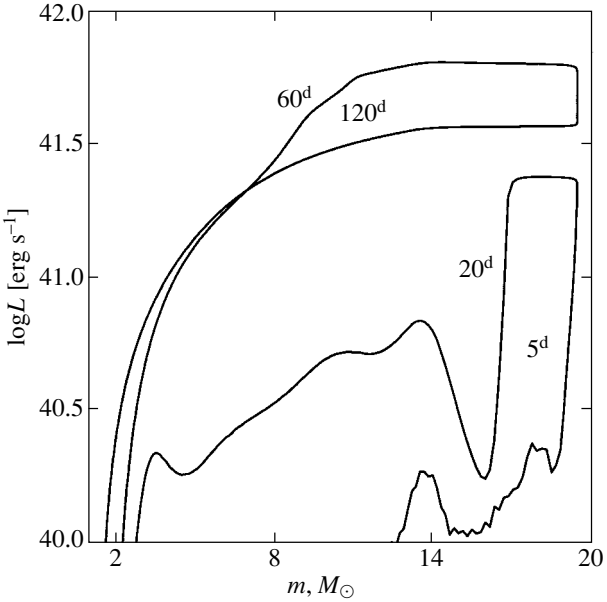

Fig. 7. Luminosity distribution in mass in the comoving frame of reference for model N at times $t = 5$, 20, 60, and 120 days.

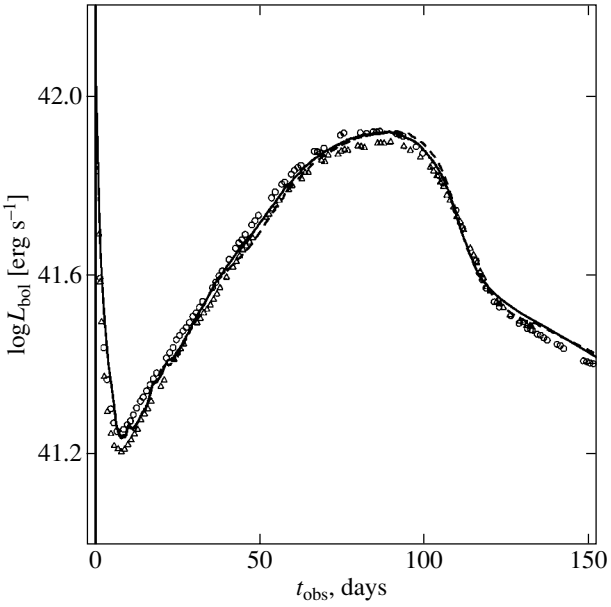

Fig. 8. Same as Fig. 4 for model N (solid line) and model Nnt—model N without nonthermal ionization (dashed line).

SN 1993J (Utrobin 1996). This finding can be explained by the much lower hydrogen abundance in the SN 1993J envelope than that of the SN 1987A envelope and, as a result, by the larger relative contribution of other elements to the opacity when nonthermal ionization is taken into account.

Before the envelope becomes optically thin, the behavior of the gas temperature and the radiation temperature with nonthermal ionization (Fig. 6) differs little from the case without nonthermal ionization (Fig. 9). However, at $t = 120$ days, a radical difference arises in the inner layers in which the main energy deposition from radioactive ^{56}Co decays takes place: the gas temperature is lower than the radiation temperature in the former case and vice versa in the latter. The enhanced ionization of the matter caused by nonthermal ionization increases the importance of bremsstrahlung processes in the energy exchange between matter and radiation and even leads to the dominance of these cooling processes over the nonthermal gas heating. In the absence of nonthermal ionization, the gas cooling by bremsstrahlung processes becomes much weaker, and the nonthermal heating dominates, causing the gas temperature to exceed the radiation temperature.

The Influence of Line Opacity

The decrease in opacity due to disregarding the line contribution in model Nlo causes the bolometric luminosity to increase from the first few days and until the luminosity peak (Fig. 10), which is equivalent in action to a decrease in opacity due to the reduction in hydrogen abundance (Utrobin 1989). The corresponding behavior of the light curve also shows up when increasing the hydrogen abundance in the outer layers (Fig. 11). These facts lead us to the firm conclusion that disregarding the contribution of lines to the opacity introduces an error of $\sim$20% into the explosion energy E (see the table). Since an increase in explosion energy E by a factor of 1.5 at the CW phase increases the bolometric luminosity by $\sim$1.5 and since an increase in envelope mass $M_{\rm env}$ by the same factor decreases the luminosity by a factor of $\sim$1.3 (Utrobin 1989), a similar error is also possible when determining the mass of the ejected matter. Recall that this dependence of the bolometric luminosity at a fixed initial radius of the presupernova makes it difficult to estimate the explosion energy E and the ejected envelope mass $M_{\rm env}$, and the observed luminosity actually determines only their ratio $E/M_{\rm env}$ (Woosley 1988; Utrobin 1993).

After the luminosity peak, the bolometric luminosity in model Nlo decreases more rapidly than the observed luminosity, which emphasizes the fundamental role of the line contribution to opacity, along with the proper description of the radiative transfer, in reproducing the observed shape of the bolometric light curve (Fig. 10). Due to the disregard of the line contribution to the opacity and without a proper allowance for the radiative transfer, we failed to achieve reasonable agreement with the observed light curve near and after the peak in the hydrodynamic modeling

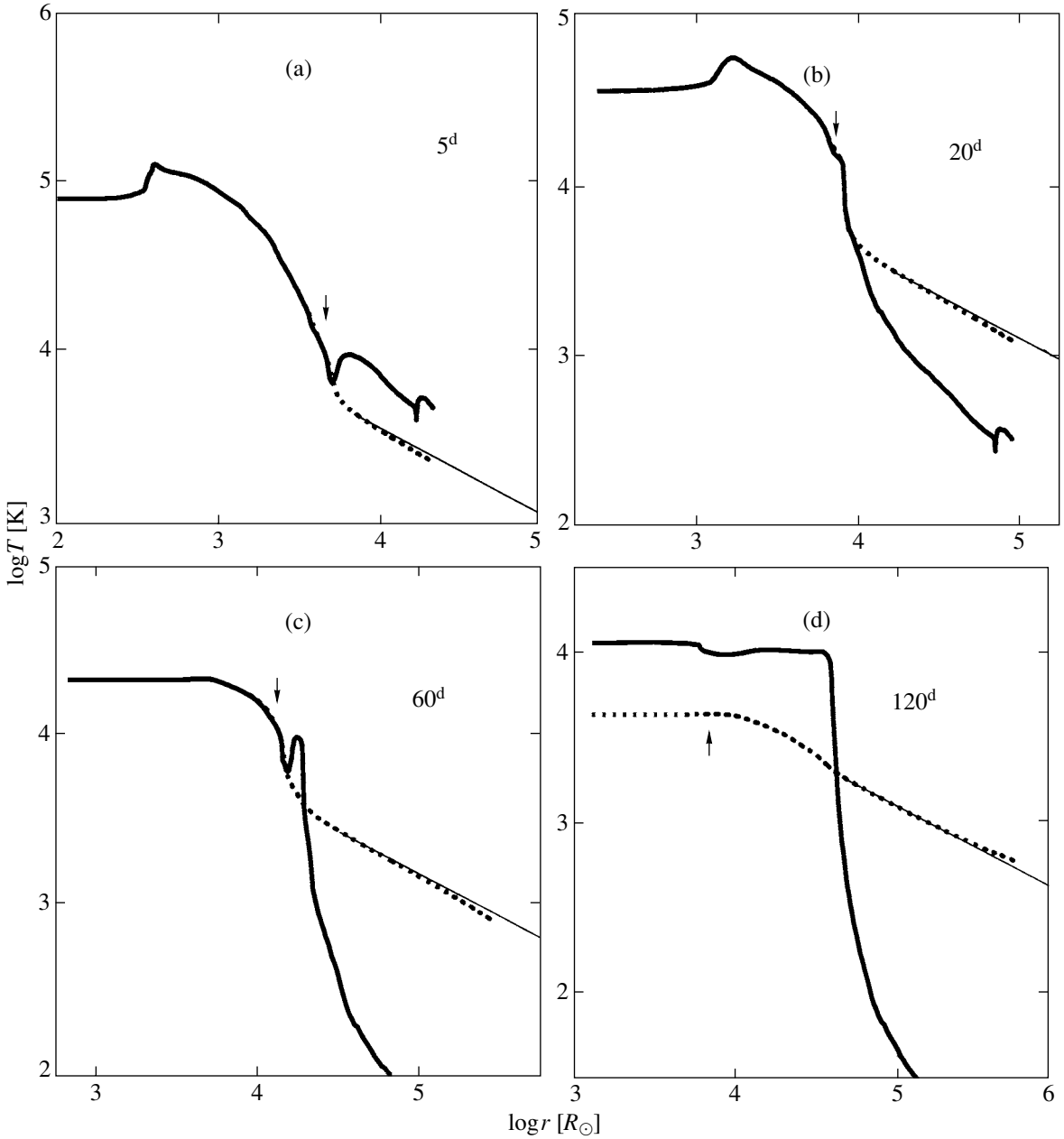

Fig. 9. Same as Fig. 6 for model Nnt.

of SN 1987A using the approximation of radiative heat conduction (Utrobin 1993).

Lines are also of the same importance in forming the gas flow in the outer layers of the expanding supernova envelope (Fig. 12). After the shock emerges on the presupernova surface at $t = 0.0823$ days, an expansion of the envelope begins, and it rapidly (during the first few days) passes to free expansion. In model N, the resonant scattering of radiation in numerous lines accelerates the outer layers up to velocities of $\approx$36 000 km s^{-1}, while in model Nlo, which disregards the line opacity, the velocity of the outer layers does not reach even 30 000 km s^{-1}. Additional line-induced acceleration takes place in the outermost layers with a mass of $\approx 10^{-6} M_\odot$.

Limb Darkening

The solution of the radiation hydrodynamics equations (1)–(5), which contain only the angular moments of the radiation intensity, yields the behavior of these moments in time and space, while the solution of the time-independent transfer equation (10) yields the limb-darkening law. Using the derived angular

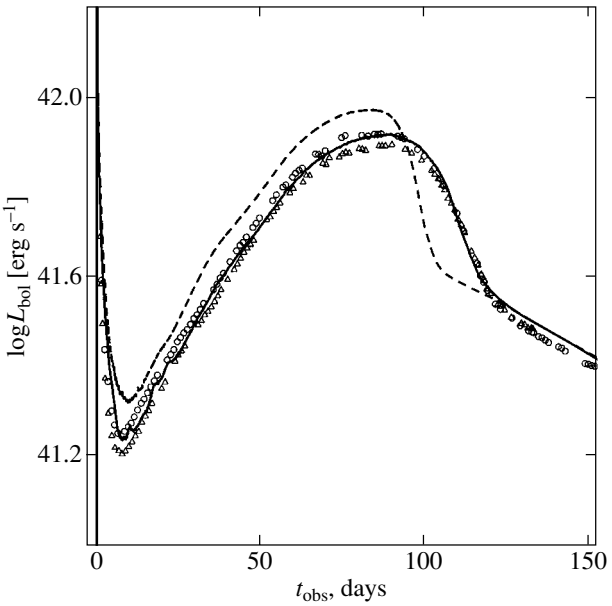

Fig. 10. Same as Fig. 4 for model N (solid line) and model Nlo—model N without line opacity (dashed line).

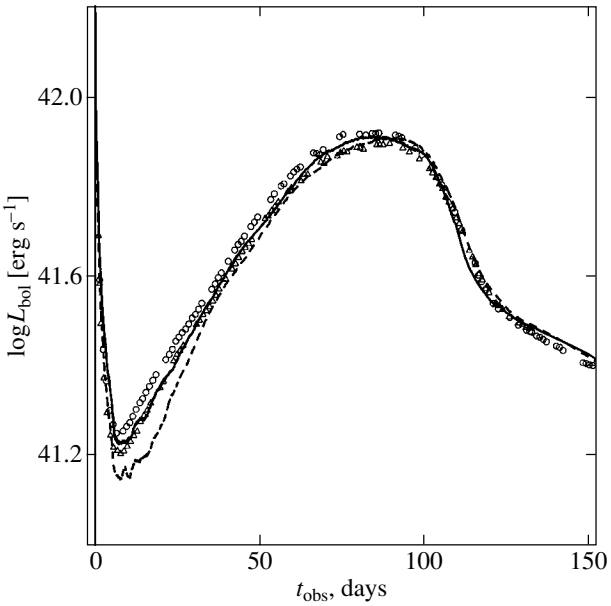

Fig. 11. Same as Fig. 4 for model Nce—model N with the LMC chemical composition and the explosion energy $E = 1.2 \times 10^{51}$ erg (solid line) and model Ncc—model N with the LMC chemical composition (dashed line).

dependence of the intensity of the radiation emerging from the supernova envelope in calculating the bolometric luminosity with the delay effect from formulas (12) and (13) proves to be a very important factor, as shown by a comparison with the isotropic radiation in model Nld (Fig. 13). During the first ~25 days, when a well-defined photosphere exists, particularly at the CW formation phase, the emitted radiation is nearly isotropic, and the bolometric light curves for models N and Nld almost coincide. As the envelope expands and becomes optically thin, the continuum formation region gradually becomes more extended, while the degree of anisotropy of the emergent radiation increases. The increase of the latter with time clearly shows the difference between the light curves for models N and Nld, which reaches particularly large values after the luminosity peak.

Interestingly, the bolometric luminosity calculated by taking into account the limb-darkening law is higher and lower than the luminosity for isotropic radiation before and after the luminosity peak (Fig. 13), respectively. To explain this behavior of the bolometric luminosity, let us simplify formula (12) by assuming that the envelope is expanding freely, $R(t) \approx u_{\rm out} t \approx u_{\rm out} t_{\rm obs}(1 + u_{\rm out}\mu/c)$, and by fitting the emergent anisotropic radiation as $I(R(t), \mu) \approx I(\mu) \propto \mu^{\alpha}$, where $u_{\rm out}$ is the velocity of the outer boundary of the supernova envelope, and α is a positive number that specifies the degree of anisotropy of the emergent radiation. Note the following two limiting cases: isotropic radiation ($\alpha = 0$) and a point radiation source ($\alpha \to \infty$). The above assumptions allow us to estimate the ratio of the bolometric luminosity $L(\alpha)$ calculated by taking into account the limb-darkening law described by the parameter α to the luminosity for isotropic radiation $L(0)$ at time $t_{\rm obs}$:

$$\frac{L(\alpha)}{L(0)} \approx 1 + \frac{u_{\rm out}}{c}\left(\frac{\alpha+2}{\alpha+3} - \frac{2}{3}\right)\frac{\partial \ln L(0)}{\partial \ln t_{\rm obs}}. \qquad (14)$$

As would be expected, this ratio depends on both the delay effect and the limb-darkening law. The correction on the right-hand side of formula (14) is on the order of $u_{\rm out}/c$; it increases with increasing degree of anisotropy of the emergent radiation, while its sign is determined solely by the time derivative of the bolometric luminosity. The latter property entirely explains the observed behavior of the bolometric luminosity with an allowance made for the limb-darkening law before and after the luminosity peak.

Influence of the Chemical Composition of the Outer Layers

The hydrodynamic models considered above have a chemical composition of the surface layers of the presupernova similar to that of the circumstellar matter. How do the basic parameters of the supernova explosion change if we substitute the chemical composition of the surface layers with the LMC chemical composition, which is characterized by a higher hydrogen abundance? Models Ncc and Nce, which have this property (see the table), give an answer to

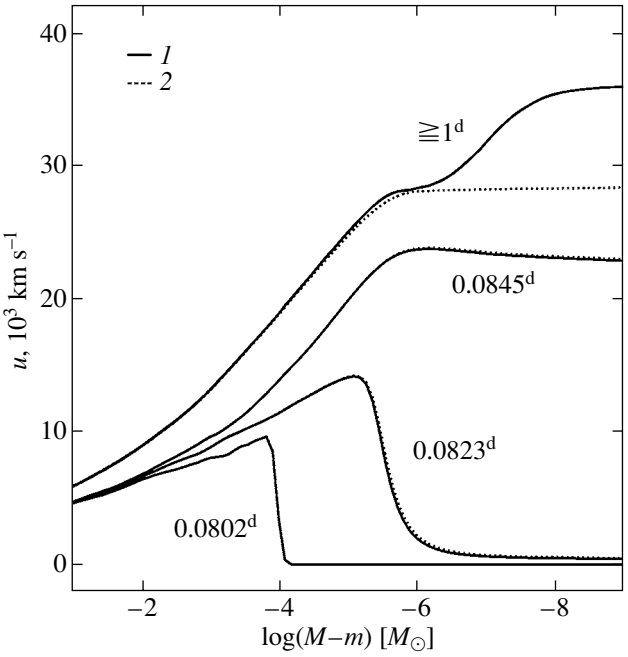

Fig. 12. Evolution of the velocity distribution in mass for model N (*1*) and model Nlo (*2*): at the time the shock approaches the presupernova surface $t = 0.0802$ days, at the time the shock emerges on the surface $t = 0.0823$ days, at $t = 0.0845$ days and, subsequently, at explosion times $t \geq 1$ days, when the envelope is already expanding freely. The mass is measured from the envelope surface.

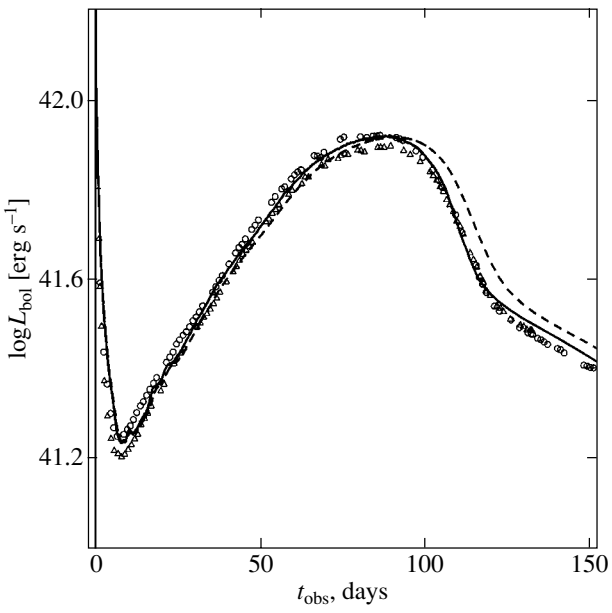

Fig. 13. Same as Fig. 4 for model N (solid line) and model Nld—model N without limb darkening (dashed line).

this question. Model Ncc shows that the passage to the LMC chemical composition in the surface layers accompanied by the corresponding increase in opacity causes the bolometric luminosity to decrease in the interval $t_{obs} \approx 5$–80 days (Fig. 11). In contrast, agreement with the observations of SN 1987A is achieved in model Nce, which has a higher explosion energy, $E = 1.2 \times 10^{51}$ erg, and a slightly modified chemical composition of the inner layers compared to model Ncc.

DISCUSSION

Our study of the influence of the presupernova structure and the degree of ^{56}Ni mixing on the bolometric light curve of SN 1987A in terms of radiation hydrodynamics in the one-group approximation by abandoning LTE and by taking into account nonthermal ionization and the contribution of lines to the opacity leads us to the following important conclusion: moderate (at velocities $u \leq 2500$ km s^{-1}) ^{56}Ni mixing can explain the observed light curve if the density of the outer layers in the presupernova exceeds that in the evolutionary model of a single nonrotating star severalfold. Moderate ^{56}Ni mixing is supported by the modeling of infrared emission lines at late stages, in the interval 200–700 days. Li *et al.* (1993) showed that the intensity of iron, cobalt, and nickel emission lines and their evolution with time are attributable to ^{56}Ni mixing up to velocities of ~2500 km s^{-1}, while the same observations led Kozma and Fransson (1998) to conclude that the iron synthesized during the explosion was mixed to velocities of ~2000 km s^{-1}.

A similar serious constraint on the ^{56}Ni mixing scales follows from an analysis of the so-called Bochum event in SN 1987A if the interpretation of it offered below is correct. This event consists in the formation of two peaks, blue and red, in the Hα profile after ~20 days (Hanuschik and Dachs 1988). The blue peak can be explained by the nonmonotonic, spherically symmetric population distribution of the second hydrogen level in the atmosphere with the excitation minimum at velocities of ~4000–5000 km s^{-1} (Chugai 1991), which is the result of nonstationary hydrogen recombination with a significant role played by the hydrogen neutralization processes involving H^- and H_2 (Utrobin and Chugai 2002). The red peak is the result of a local enhancement of the hydrogen excitation from an asymmetric ^{56}Ni ejection in the far hemisphere (Chugai 1991) with an absolute velocity of ~4600 km s^{-1} (Utrobin *et al.* 1995). The spherically symmetric nonmonotonicity of the hydrogen excitation is very sensitive to the nonthermal excitation produced by ^{56}Ni, and its existence for ~20–40 days implies that the ^{56}Ni mixing at that

time was within the photosphere and, accordingly, did not extend in velocity farther than $\sim$2500 km s^{-1}.

Thus, moderate ^{56}Ni mixing in the envelope of SN 1987A receives confirmation both in spectroscopic observations at the photospheric phase and in nebular observations. The above analysis of the bolometric light curve convincingly shows that the outer layers of the presupernova have a density that is several times higher than that in the evolutionary model of a single nonrotating star. This important conclusion has the following direct implication: the presupernova structure required for the explosion of SN 1987A can be produced during the evolution of a single star in which, apart from the mass of the star on the main sequence and its chemical composition, stellar rotation may play a key role, or during the evolution of the presupernova in a close binary during the merger with the secondary component.

As must be the case, abandoning LTE and allowing for nonthermal ionization when solving the equation of state and determining the mean opacities and the thermal emission coefficient result in a significant difference between the gas temperature and the radiation temperature in the optically thin layers of the supernova envelope compared to the equilibrium case. This stresses the importance of the correct description of the energy exchange between matter and radiation when modeling supernova explosions.

Our study shows how important an allowance for the contribution of lines to the opacity is in the hydrodynamic modeling of SN 1987A. First, it has become clear that the contribution of lines to the opacity in an expanding envelope and the accurate description of the radiative transfer play a fundamental role in reproducing the observed shape of the bolometric light curve. Second, it has been established that disregarding the contribution of lines to the opacity introduces an error of $\sim$20% into the explosion energy, and that a similar error is possible when determining the mass of the ejected matter. Third, the resonant scattering of radiation in numerous lines accelerates the outer layers up to velocities of $\approx$36 000 km s^{-1}, while the velocities of these layers without an allowance for lines do not reach even 30 000 km s^{-1}; the additional line-induced acceleration affects the outer layers with a mass of $\approx 10^{-6} M_\odot$.

The next important conclusion is that proper calculations of the observed supernova luminosity require taking into account both the delay effects and the limb-darkening effects; the importance of the latter increases with time as the anisotropy of the emergent radiation increases. This conclusion is confirmed by our analytic estimate of the bolometric luminosity that includes the delay effects and the limb-darkening law. Accordingly, this estimate contains a explicit dependence on the time derivative of the bolometric luminosity and the degree of anisotropy of the emergent radiation.

In conclusion, let us note that substituting the chemical composition of the surface layers, which is similar to that of the circumstellar matter, with the LMC chemical composition, which is characterized by a higher hydrogen abundance, causes the bolometric luminosity to decrease in the interval $t_{\rm obs} \approx$ 5–80 days, and good agreement with the observations of SN 1987A is achieved with a higher explosion energy, $E = 1.2 \times 10^{51}$ erg.

ACKNOWLEDGMENTS

I wish to thank S.I. Blinnikov and N.N. Chugai for their helpful discussions. I am grateful to A. Heger who provided the evolutionary model l20n2ae and comments to it. This work was supported in part by the Russian Foundation for Basic Research (project no. 01-02-16295).

REFERENCES

1. W. D. Arnett, Astrophys. J. **319**, 136 (1987).
2. K. L. Bell and K. A. Berrington, J. Phys. B: At. Mol. Phys. **20**, 801 (1987).
3. I. S. Berezin and N. P. Zhidkov, *Methods of Calculations* (Fizmatgiz, Moscow, 1962) [in Russian], Vol. 2.
4. S. I. Blinnikov, Pis'ma Astron. Zh. **22**, 92 (1996) [Astron. Lett. **22**, 79 (1996)].
5. S. I. Blinnikov and O. S. Bartunov, Astron. Astrophys. **273**, 106 (1993).
6. S. I. Blinnikov and D. K. Nadyozhin, *Supernovae,* Ed. by S. E. Woosley (Springer, New York, 1991), p. 213.
7. S. Blinnikov, P. Lundqvist, O. Bartunov, *et al.*, Astrophys. J. **532**, 1132 (2000).
8. A. Cassatella, *ESO Workshop on SN 1987A,* Ed. by I. J. Danziger (ESO, Garching, 1987), p. 101.
9. J. I. Castor, D. C. Abbott, and R. I. Klein, Astrophys. J. **195**, 157 (1975).
10. R. M. Catchpole, J. M. Menzies, A. S. Monk, *et al.*, Mon. Not. R. Astron. Soc. **229**, 15P (1987).
11. R. M. Catchpole, P. A. Whitelock, M. W. Feast, *et al.*, Mon. Not. R. Astron. Soc. **231**, 75P (1988).
12. N. N. Chugai, Pis'ma Astron. Zh. **17**, 942 (1991) [Sov. Astron. Lett. **17**, 400 (1991)].
13. R. J. Dufour, *IAU Symp. No. 108: Structure and Evolution of the Magellanic Clouds,* Ed. by S. van den Bergh and K. S. de Boer (Reidel, Dordrecht, 1984), p. 353.
14. L. Ensman and A. Burrows, Astrophys. J. **393**, 742 (1992).
15. R. Gilmozzi, A. Cassatella, J. Clavel, *et al.*, Nature **328**, 318 (1987).
16. C. W. Gear, *Numerical Initial Value Problems in Ordinary Differential Equations* (Prentice-Hall, New Jersey, 1971).

17. E. K. Grassberg and D. K. Nadyozhin, Astrophys. Space Sci. **44**, 409 (1976).
18. E. K. Grasberg, V. S. Imshennik, and D. K. Nadyozhin, Astrophys. Space Sci. **10**, 3 (1971).
19. M. Hamuy, N. B. Suntzeff, R. Gonzalez, and G. Martin, Astron. J. **95**, 63 (1988).
20. R. W. Hanuschik and J. Dachs, Astron. Astrophys. **205**, 135 (1988).
21. W. Hillebrandt and F. Meyer, Astron. Astrophys. **219**, L3 (1989).
22. W. Hillebrandt, P. Höflich, J. W. Truran, and A. Weiss, Nature **327**, 597 (1987).
23. R. M. Humphreys and D. B. McElroy, Astrophys. J. **284**, 565 (1984).
24. V. S. Imshennik, Pis'ma Astron. Zh. **19**, 883 (1993) [Astron. Lett. **19**, 358 (1993)].
25. V. S. Imshennik and Yu. I. Morozov, *Radiation Relativistic Gas Dynamics of High-Temperature Phenomena* (Atomizdat, Moscow, 1981).
26. V. S. Imshennik and D. K. Nadyozhin, Astron. Zh. **41**, 829 (1964).
27. V. S. Imshennik and D. K. Nadyozhin, Pis'ma Astron. Zh. **14**, 1059 (1988) [Sov. Astron. Lett. **14**, 449 (1988)].
28. P. Jakobsen, R. Albrecht, C. Barbieri, *et al.*, Astrophys. J. **369**, L63 (1991).
29. C. Kozma and C. Fransson, Astrophys. J. **390**, 602 (1992).
30. C. Kozma and C. Fransson, Astrophys. J. **497**, 431 (1998).
31. R. L. Kurucz and B. Bell, *Atomic Line Data, Kurucz CD-ROM No. 23* (Smithsonian Astrophys. Obs., Cambridge, USA, 1995).
32. H. Li, R. McCray, and R. A. Sunyaev, Astrophys. J. **419**, 824 (1993).
33. P. Lundqvist and C. Fransson, Astrophys. J. **464**, 924 (1996).
34. D. Mihalas and B. W. Mihalas, *Foundations of Radiation Hydrodynamics* (Oxford Univ. Press, New York, 1984).
35. O. Österby and Z. Zlatev, *Direct Methods for Sparse Matrices* (Springer-Verlag, Berlin, 1983; Mir, Moscow, 1987).
36. N. Panagia, R. Gilmozzi, J. Clavel, *et al.*, Astron. Astrophys. **177**, L25 (1987).
37. Ph. Podsiadlowski, Publ. Astron. Soc. Pac. **104**, 717 (1992).
38. Ph. Podsiadlowski and P. C. Joss, Nature **338**, 401 (1989).
39. C. S. J. Pun, R. P. Kirshner, G. Sonneborn, *et al.*, Astrophys. J., Suppl. Ser. **99**, 223 (1995).
40. J. Rousseau, N. Martin, L. Prevot, *et al.*, Astron. Astrophys., Suppl. Ser. **31**, 243 (1978).
41. T. Shigeyama and K. Nomoto, Astrophys. J. **360**, 242 (1990).
42. I. S. Shklovsky, Pis'ma Astron. Zh. **10**, 723 (1984) [Sov. Astron. Lett. **10**, 302 (1984)].
43. G. Sonneborn, B. Altner, and R. P. Kirshner, Astrophys. J. **323**, L35 (1987).
44. R. S. Sutherland, Mon. Not. R. Astron. Soc. **300**, 321 (1998).
45. V. P. Utrobin, Pis'ma Astron. Zh. **15**, 99 (1989) [Sov. Astron. Lett. **15**, 42 (1989)].
46. V. P. Utrobin, Astron. Astrophys. **270**, 249 (1993).
47. V. P. Utrobin, Astron. Astrophys. **306**, 219 (1996).
48. V. P. Utrobin, Preprint No. 12-98, ITÉF (Inst. of Theoretical and Experimental Physics, Moscow, 1998).
49. V. P. Utrobin and N. N. Chugai, Pis'ma Astron. Zh. **28**, 440 (2002) [Astron. Lett. **28**, 386 (2002)].
50. V. P. Utrobin, N. N. Chugai, and A. A. Andronova, Astron. Astrophys. **295**, 129 (1995).
51. D. A. Verner, G. J. Ferland, K. T. Korista, and D. G. Yakovlev, Astrophys. J. **465**, 487 (1996).
52. D. A. Verner and D. G. Yakovlev, Astron. Astrophys., Suppl. Ser. **109**, 125 (1995).
53. G. S. Voronov, At. Data Nucl. Data Tables **65**, 1 (1997).
54. E. J. Wampler, L. Wang, D. Baade, *et al.*, Astrophys. J. **362**, L13 (1990).
55. L. Wang, Astron. Astrophys. **246**, L69 (1991).
56. A. Weiss, W. Hillebrandt, and J. W. Truran, Astron. Astrophys. **197**, L11 (1988).
57. A. W. Wishart, Mon. Not. R. Astron. Soc. **187**, 59P (1979).
58. S. E. Woosley, Astrophys. J. **330**, 218 (1988).
59. S. E. Woosley, P. A. Pinto, and L. Ensman, Astrophys. J. **324**, 466 (1988).
60. S. E. Woosley, A. Heger, T. A. Weaver, and N. Langer, *SN 1987A: Ten Years Later,* Ed. by M. M. Phillips and N. B. Suntzeff (1997, in press).

Translated by V. Astakhov

Astronomy Letters, Vol. 30, No. 5, 2004, pp. 309–318. Translated from Pis'ma v Astronomicheskiĭ Zhurnal, Vol. 30, No. 5, 2004, pp. 351–361.

Dynamics of the Flows Accreting onto a Magnetized Neutron Star

A. M. Bykov* and A. M. Krasil'shchikov**

Ioffe Physicotechnical Institute, Russian Academy of Sciences, St. Petersburg, 194021 Russia

Received June 26, 2003

Abstract—We investigate the unsteady column accretion of material at a rate $10^{15}\,\mathrm{g\,s^{-1}} \le \dot{M} \le 10^{16}\,\mathrm{g\,s^{-1}}$ onto the surface of a magnetized neutron star using a modified first-order Godunov method with splitting. We study the dynamics of the formation and evolution of a shock in an accretion column near the surface of a star with a magnetic field $5 \times 10^{11} \le B \le 10^{13}$ G. An effective transformation of the accretion flow energy into cyclotron radiation is shown to be possible for unsteady accretion with a collisionless shock whose front executes damped oscillations. The collisionless deceleration of the accreting material admits the conservation of a fraction of the heavy nuclei that have not been destroyed in spallation reactions. The fraction of the CNO nuclei that reach the stellar atmosphere is shown to depend on the magnetic field strength of the star. © *2004 MAIK "Nauka/Interperiodica".*

Key words: *plasma astrophysics, hydrodynamics and shock waves, accretion, neutron stars.*

INTRODUCTION

The accretion onto compact objects has been considered as an effective source of hard X-ray radiation for about forty years (see Zel'dovich 1964; Salpeter 1964; Shakura and Sunyaev 1973).

Several analytical, semianalytical, and numerical models of accretion onto neutron stars (NSs) and black holes have been constructed (see, e.g., Frank *et al.* 2002). However, some of the important questions formulated even in pioneering papers have no clear answers as yet. One of the fundamental questions is the nature of the accreting material: Is it a gas of interacting particles (hydrodynamic regime) or a collection of separate noninteracting particles (free-fall regime)? Zel'dovich (1967) and Zel'dovich and Shakura (1969) considered these two regimes and showed that the radiation spectrum near the stellar surface depends significantly on the accretion regime under consideration.

Up to now, the authors of the models have provided circumstantial qualitative evidence to substantiate a particular regime in the hope that a realistic model supported by experimental evidence can *a posteriori* justify the choice of a regime, at least for a certain domain of parameters of the accretion system. Under which conditions collisionless shocks that decelerate the material as it moves toward the stellar surface arise in an accretion flow is another related question.

Bisnovatyi-Kogan and Fridman (1969) pointed out that a *collisionless* shock could appear in the flow accreting onto a NS if the star possesses a dipole magnetic field of $B \sim 10^8$ G.

The shock that decelerates the flow accreting onto a NS in a binary system plays a key role in the model by Davidson and Ostriker (1973). In their models, Shapiro and Salpeter (1975), Basko and Sunyaev (1976), Langer and Rappoport (1982), and Braun and Yahel (1984) considered the accretion onto a NS under various assumptions about the magnetic field strength of the star and found *steady-state* solutions of the system of hydrodynamic equations for the accretion flow. The models by Shapiro and Salpeter (1975) and Langer and Rappoport (1982) postulate the existence of a *stationary collisionless* shock at a certain height above the surface, which is a parameter of these models. Basko and Sunyaev (1976) demonstrated the accretion regime with a *radiative* shock in the NS atmosphere. In their model, Braun and Yahel (1984) showed that a *stationary collisionless* shock could exist above the surface of a magnetized NS only when the accretion rate is low enough (more specifically, does not exceed a few percent of the Eddington value).

Detailed models for the two-dimensional unsteady *radiation-dominated super-Eddington* accretion onto a magnetized NS have been developed by Arons, Klein, and coauthors (see Klein and Arons 1989; Klein *et al.* 1996; and references therein). The authors of these models show that, if the accretion rate is high enough (more specifically, if the accretion is essentially super-Eddington one), then *nonstationary radiation-dominated* shocks appear and evolve in the column. An important peculiarity of these studies

*E-mail: byk@astro.ioffe.ru
**E-mail: kra@astro.ioffe.ru

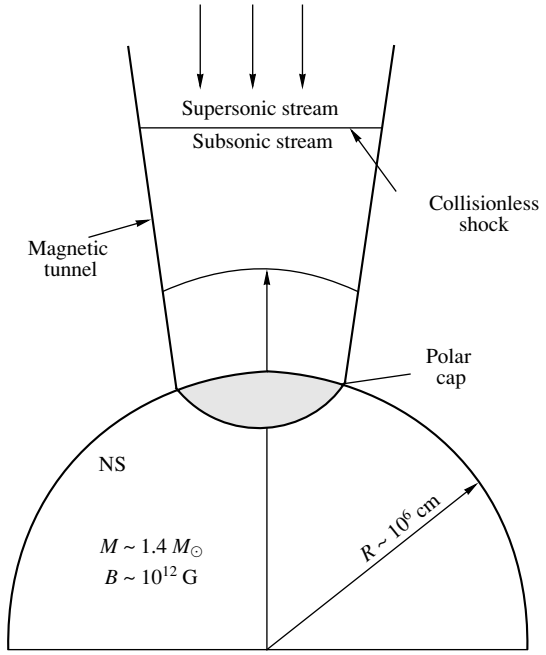

Fig. 1. Geometry of the accretion column.

is that the existence of a shock in the column is not postulated, but is the result of model evolution of the system.

In this paper, we present a numerical model for the *sub-Eddington* one-dimensional unsteady hydrodynamic (in the above sense) accretion onto a magnetized NS. As in the paper by Klein and Arons (1989), we do not postulate the existence of a shock in the column from the outset. Our study is unique in that we construct a hydrodynamic code based on the Godunov method, which allows us to deal with discontinuous flows and, in particular, to describe the shock dynamics.

The model consistently takes into account the kinetics of electron–ion beams in a strong magnetic field. The magnetic field in the column is assumed to be known, but the related processes of matter–radiation interaction play a crucial role in the evolution of the accretion flow.

In Section 1, we present our hydrodynamic model of the accretion flow. In Section 2, based on model profiles of the flow in the column, we consider the destruction probability of CNO nuclei in the accretion flow. The results obtained are discussed below.

1. ACCRETION FLOW HYDRODYNAMICS

Formulation of the Problem

We consider the time evolution of the accretion flow in the magnetic column above the polar cap of a magnetized NS at distances of no larger than several NS radii from its surface. We assume that the accretion is hydrodynamic, because the growth time of magnetohydrodynamic (MHD) instabilities is short under the conditions in question. Under the conditions of strong initial anisotropy of the accretion flow, the multistream instabilities can have characteristic growth rates comparable to the ion plasma frequency, $\omega_{\rm pi} \sim 1.2 \times 10^{12} n_{18}^{1/2}$ s^{-1}. Such growth rates are typical of the particle isotropization processes in collisionless shocks. Note that the cyclotron frequencies are much higher for typical magnetic fields. The characteristic propagation velocity of MHD disturbances is $V_{\rm A} \approx c(1-\alpha)$, where $\alpha = 10^{-11} n_{18} B_{12}^{-2} \ll 1$. This estimate can be obtained from general relations (see, e.g., the book by Velikovich and Liberman 1987). Since there are currently no microscopic simulations of instabilities under typical conditions of NS magnetic fields, we study the accretion flow by assuming that instability grows in a subrelativistic flow at a rate $\omega_{\rm pi}$. The simulations can be used to interpret the observations of X-ray pulsars.

The electrons and ions move in the accretion flow with the same mean (flow) velocity, but have different temperatures.

The NS is assumed to have a constant dipole magnetic field on the time scales under consideration. The geometry of the accretion column is shown in Fig. 1.

Basic Parameters and Equations

The basic model parameters include the mass ($M_\star$) and radius ($R_\star$) of the NS as well as the magnetic field strength ($B_\star$) at its magnetic pole and the accretion rate per unit area of the accretion column base ($\dot{M}/A_0$).

The system of hydrodynamic equations that describe the evolution of the flow may be written as

$$\frac{\partial \rho}{\partial t} + \mathrm{div}(\rho \mathbf{u}) = 0, \qquad (1)$$

$$\frac{\partial (\rho u_\alpha)}{\partial t} + \frac{\partial p}{\partial x_\alpha} + \frac{\partial}{\partial x_\beta}(\rho u_\alpha u_\beta) = \mathcal{F}_\alpha,$$

$$\frac{\partial}{\partial t}\left[\rho_s (E_s + \frac{u^2}{2})\right]$$

$$+\mathrm{div}\left[\rho_s \mathbf{u}(E_s + \frac{u^2}{2}) + p_s \mathbf{u}\right] = \mathcal{Q}_s,$$

where $\rho = \rho_e + \rho_i$, $p = p_i + p_e$, $\mathcal{F}$ and $\mathcal{Q}_s$ denote the momentum and energy sources, and $s = i, e$ is the type of particles.

We supplement this system with the equations of state for each type of particles. We use the equation of state for an ideal gas, $E_s = p_s/[\rho_s(\gamma_s - 1)]$. For

$x_s = k_B T_s/(m_s c^2) \ll 1$, the adiabatic index γ_s may be written as $\gamma_s \approx \gamma_{0s}(1 - x_i)$ (de Groot *et al.* 1980), where $\gamma_{0i} = 5/3$ is a typical nonrelativistic value for particles with three degrees of freedom, and $\gamma_{0e} = 3$, since the electrons in the strong fields under consideration are quasi-one-dimensional.

The electron momentum distribution is one-dimensional, because the characteristic relaxation time of the electron Landau levels is $\sim 10^{-15} B_{12}^{-2}$ s, where $B_{12} = B/10^{12}$ G (see, e.g., Bussard 1980), and it is the shortest time in the system under consideration after the cyclotron time. The radiative decay time of the excited ion Landau levels is $\sim 5 \times 10^{-9} B_{12}^{-2}$ s, and is appreciably longer than the collisionless relaxation time of the ion momenta $\propto \omega_{pi}^{-1}$. Therefore, in this case, the ions are at highly excited Landau levels and may thus be considered three-dimensional and be described quasi-classically.

We consider the *one-dimensional* motion of the accreting plasma along the *dipole lines* of a strong NS magnetic field. In this geometry, system (1) may be rewritten as

$$r^3 \frac{\partial \rho}{\partial t} + \frac{\partial}{\partial r}(r^3 \rho u) = 0, \quad (2)$$

$$r^3 \frac{\partial (\rho u)}{\partial t} + \frac{\partial}{\partial r}[r^3 (p + \rho u^2)] = r^3 \mathcal{F} + 3 r^2 p,$$

$$r^3 \frac{\partial}{\partial t}\left[\rho_s (E_s + \frac{u^2}{2})\right] + \frac{\partial}{\partial r}\left(r^3 \left[\rho_s u (E_s + \frac{u^2}{2}) + p_s u\right]\right) = r^3 \mathcal{Q}_s.$$

The system of equations (2) should be supplemented with initial and boundary conditions. As the initial condition, we consider a column filled with a cold, freely falling gas. The boundary condition in the upper part of the column is the condition for the inflow of a cold supersonic stream, while the boundary condition in the lower part of the column is the condition for the absence of a stream flowing into the star.

Physical Processes in the Accretion Flow

Here, we describe the processes that contribute to the terms $\mathcal{F}$ and $\mathcal{Q}_s$ of system (2).

Since we are considering a single-stream flow, the forces acting on the ions and electrons add up in one force term:

$$\mathcal{F} = F^i + F^e, \; F^i = F^i_{\rm grav} - F_{\rm atm},$$
$$F^e = F^e_{\rm grav} - F_{\rm nonres} - F_{\rm res},$$

where $F^i_{\rm grav}$ and $F_{\rm atm}$ denote the gravity and the viscous force of resistance to the flow (which is effective only in the NS atmosphere); and $F^e_{\rm grav}$, $F_{\rm nonres}$, and $F_{\rm res}$ denote the gravity and the nonresonant and resonant radiation pressure forces, respectively.

The gravitational force acting on a unit volume is

$$F_{\rm grav} = F^e_{\rm grav} + F^i_{\rm grav} = (n m_i + Z n m_e)\frac{G M_\star}{r^2}, \quad (3)$$

where n is the ion density.

To calculate the nonresonant radiation pressure force, we use the following formula from the book by Zheleznyakov (1997):

$$F_{\rm nonres} = n_e \frac{\sigma_T}{c}\frac{\sigma_{ST} T_\gamma^4}{1 + \tau_T}, \quad (4)$$

where n_e is the electron density, σ_{ST} is the Stefan–Boltzmann constant, T_γ is the local temperature of the radiation field, and τ_T is the nonresonant optical depth.

To calculate the resonant radiation pressure force, we numerically integrate the equation of radiative transfer in the cyclotron line, find the energy density of the photon field $U_{\rm phot}$, and determine $F_{\rm res}$ as $dU_{\rm phot}/dr$. Since the column in the cyclotron line is optically thick, the transfer equation may be written as the diffusion equation

$$\nabla \cdot \mathbf{J}_{\rm phot} = S_{\rm phot} + \frac{1}{3}\mathbf{u} \cdot \nabla U_{\rm phot}, \quad (5)$$

where $S_{\rm phot}$ are the cyclotron photon sources, and $\mathbf{J}_{\rm phot} = \frac{4}{3}\mathbf{u} U_{\rm phot} - \kappa \nabla U_{\rm phot}$ is the photon diffusion flux in the line. Since the diffusion of cyclotron photons across the magnetic field is severely hampered (see, e.g., Arons *et al.* 1987), we consider only the parallel component of Eq. (5), which may be written as

$$\frac{1}{r^3}\frac{\partial}{\partial r}\left\{r^3\left[\frac{4}{3}U_{\rm phot} u - \kappa_{||}\frac{1}{r^3}\frac{\partial}{\partial r}\left(r^3 U_{\rm phot}\right)\right]\right\} = S_{\rm phot} + \frac{1}{3}u\frac{1}{r^3}\frac{\partial}{\partial r}\left(r^3 U_{\rm phot}\right), \quad (6)$$

where $\kappa_{||}$ is the diffusion coefficient parallel to the magnetic field. This equation can be integrated by the shooting method. The boundary conditions for it are the following: the cyclotron photons freely escape from the upper boundary of the column, and their number on the stellar surface corresponds to a blackbody spectrum with temperature $T_{\rm eff}$.

To calculate the friction force exerted on the flow from the NS atmosphere, we use the following standard expression for the Coulomb stopping in a dense environment:

$$F_{\rm atm} = \frac{4\pi n_a n_i e^4 Z^2 \ln\Lambda}{m_e u^2}, \quad (7)$$

where Λ is the Coulomb logarithm, n_a is the electron density in the NS atmosphere, and u is the velocity of the accretion flow. A similar expression was used in the paper by Bildsten *et al.* (1992) devoted to the collisional destruction of CNO nuclei in the NS atmosphere.

The forces acting on the flow work on it, and this work is effectively redistribited between the ions and electrons.

Let the external force F^i act on the ions and the external force F^e act on the electrons. It then follows from local electrical neutrality (if the frequencies of the external-force variations are much lower than the characteristic plasma frequencies) that the fluxes of both types of particles are equal, i.e.,

$$(F^e - eE)\frac{n_e}{m_e\nu_{ei}} = (F^i + ZeE)\frac{n_i}{m_i\nu_{ei}},$$

where E is the ambipolar electric field, and ν_{ei} is the effective electron–ion relaxation frequency. Since $n_e = Zn_i$,

$$eE = F^e\frac{1}{\xi+1} - F^i\frac{\xi}{Z(\xi+1)},$$

where $\xi = m_e/m_i$, and the resulting effective force acting on the ions is

$$F^i_{\text{eff}} = (F^i + F^eZ)\frac{1}{\xi+1},$$

while the resulting effective force acting on the electrons is

$$F^e_{\text{eff}} = (F^i + F^eZ)\frac{\xi}{Z(\xi+1)}.$$

The ion energy changes through the following processes:

the small-angle scattering in Coulomb collisions with electrons H_{ie};

the collisional excitation of electron Landau levels Q_{cyc};

the collisional relaxation on electrons of the NS atmosphere Q_{relax};

the work done by the effective force, $F^i_{\text{eff}}u$.

The cyclotron ion cooling was taken into account in the model. Its effect is noticeable if the dipole magnetic field exceeds 5×10^{11} G and if the system is transparent to photons in the proton cyclotron line.

The electron energy changes through the following processes:

the small-angle-scattering in Coulomb collisions with ions H_{ei};

the bremsstrahlung cooling in collisions with ions and electrons, Br_{ei} and Br_{ee};

the excitation of Landau levels in collisions with ions and electrons, Cyc_{ei} and Cyc_{ee};

the Compton processes Q_{compt};

the work done by the effective force $F^e_{\text{eff}}u$.

For details on the calculations of these terms, see the Appendix.

The Method of Numerical Solution

A multicomponent accretion flow onto the NS surface can have discontinuities and, in particular, shocks. For this reason, we chose the standard Godunov method (Godunov 1959; Godunov *et al.* 1976) to solve the problem.

The Godunov method is directly applicable to one-component[1] systems that are described by equations without any sources. To include the sources in Eqs. (2) in the numerical scheme, we use an approach based on the works by Le Veque (1997). It consists in splitting system (2) into two parts: one part describes the conservation of the fluxes along dipole lines and can be integrated using a modified Godunov method, and the other part describes the presence of energy and momentum sources and can be integrated by the Gear method.

The necessity of using this approach stems from the multicomponent nature of the system, which contains two types of particles that interact with each other, with the external magnetic and gravitational fields, and with the radiation field in a complicated way.

We make system (2) dimensionless by multiplying $\mathcal{F}$ by $C_F = \frac{t_\star}{\rho_\star u_\star}$ and $\mathcal{Q}_s$ by $C_Q = \frac{t_\star}{\rho_\star u_\star^2}$, where $t_\star$, $u_\star$, and $\rho_\star$ are the characteristic time, velocity, and density scales, respectively.

Equations (2) in the column are integrated by a combined method that allows the Godunov scheme to be generalized to systems with energy and momentum exchange between its components (the sources in system (2)). We break down the accretion column into spatial cells centered on points $x_{i-1/2}$. From the initial state at time $t=0$ to the state at the current time t, the integration is performed over the steps Δt in each of which the following operations are performed:

(1) The integration of the equations without sources corresponding to the conservation of the fluxes along dipole lines:

$$r^3\frac{\partial\rho}{\partial t} + \frac{\partial}{\partial r}(r^3\rho u) = 0, \qquad (8)$$

[1] The currently available multitemperature methods were described, for example, by Zabrodin and Prokopov (1998).

$$r^3\frac{\partial(\rho u)}{\partial t}+\frac{\partial}{\partial r}[r^3(p+\rho u^2)]=0,$$

$$r^3\frac{\partial}{\partial t}\left[\rho_s(E_s+\frac{u^2}{2})\right]$$
$$+\frac{\partial}{\partial r}\left(r^3\left[\rho_s u\left(E_s+\frac{u^2}{2}\right)+p_s u\right]\right)=0.$$

At this stage, we integrate the system simultaneously in the entire column, i.e., in all cells $x_{i-1/2}$.

(2) The integration of the equations with the momentum and energy sources written for the quantities averaged over the spatial cell:

$$\frac{\partial(\rho_i u_i)}{\partial t}=C_F\mathcal{F}_i+\frac{3}{r_i}p_i, \qquad (9)$$
$$\frac{\partial}{\partial t}\left[\rho_{s_i}(E_{s_i}+\frac{u_i^2}{2})\right]=C_Q\mathcal{Q}_{s_i},$$

where q_i are the values of the physical quantities averaged over cell i, independently in each of the cells $x_{i-1/2}$. At each of the two stages, the integration is performed over the same time interval specified by the Courant condition at the first stage.

Since system (9) is stiff, we use the standard LSODE subroutine (Hindmarsh 1983), in which version B of the Gear method (see, e.g., Gear 1971) is implemented, for its integration. Note that many popular methods for integrating stiff systems that are based on the modified Bulirsch–Stoer method (Press *et al.* 1983) require an explicit specification of the Jacobian of the system. In our case, this leads to significant complications, because system (9) has a complex structure of its right-hand parts that includes the terms specified only in numerical form.

To integrate system (8), we used the capacitive modification of the Godunov method of the first order suggested by LeVeque (1997). The essence of this method is that, if the conservation law for the physical quantity $q(x,t)$ is written in generalized form instead of the classical divergence form,

$$\kappa(x)\frac{\partial q(x,t)}{\partial t}+\frac{\partial f(q(x,t))}{\partial x}=0,$$

where $\kappa(x)$ is a given function of the spatial coordinate that denotes the effective capacity of the region of space under consideration (e.g., the porosity of the medium), then the conventional Godunov difference scheme is inapplicable, and instead of the Godunov standard expression for the grid function q at time $t_0+\Delta t$

$$\tilde{q}_i=q_i-\frac{\Delta t}{\Delta x_i}\left(F_i-F_{i+1}\right),$$

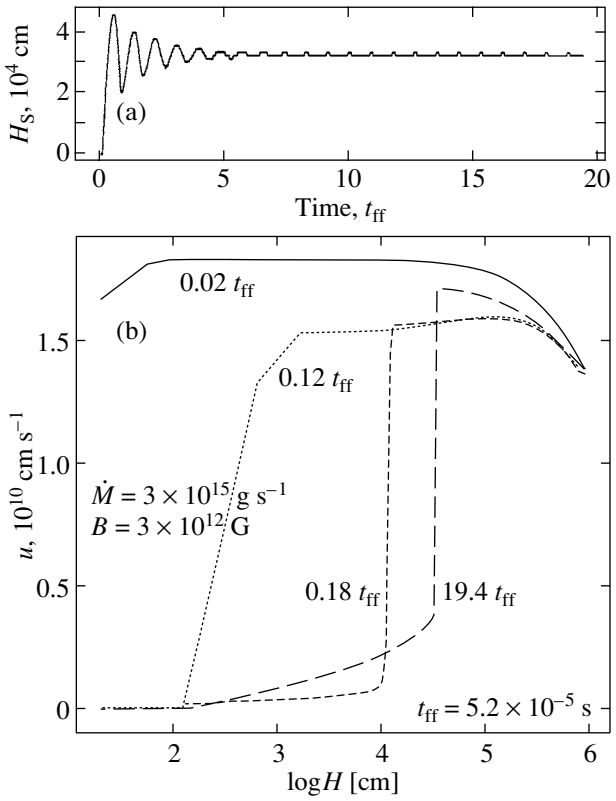

Fig. 2. Evolution of the accretion flow: (a) shock height versus time; (b) evolution of the flow velocity profile.

where F_i is the q flux flowing from cell i into cell $i-1$, we may write

$$\tilde{q}_i=q_i-\frac{\Delta t}{\kappa_i\Delta x_i}\left(F_i-F_{i+1}\right),$$

where Δx_i is the size of cell i, and κ_i is the value of $\kappa(x)$ averaged over cell i.

Results

We have implemented the complex scheme of computations[2] described above and investigated the evolution of the accretion flow for various model parameters.

We have found that strong shocks develop in the column on time scales of $\sim10^{-5}$ s. These shocks execute stable oscillations about their equilibrium positions with periods of $\sim10^{-5}$ s that are damped out in a time of $\sim10^{-3}$ s. A typical example of the evolution of the shock front and the flow velocity profile is shown in Fig. 2.

[2]Some of the computations were carried out under the support of the St. Petersburg Branch of the Interdepartmental Supercomputer Center (http://scc.ioffe.ru/).

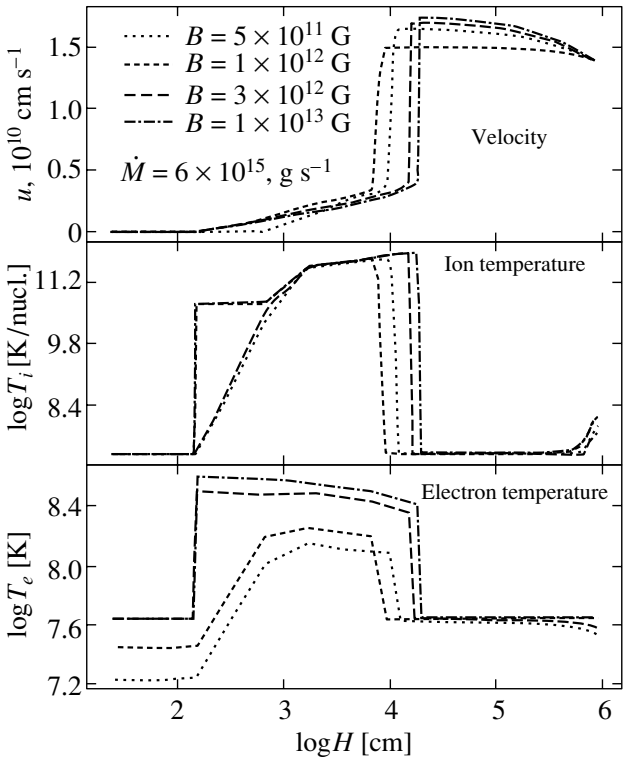

Fig. 3. Dependence of the flow profiles at $\tau = 1.3 \times 10^{-3}$ s on the magnetic field strength.

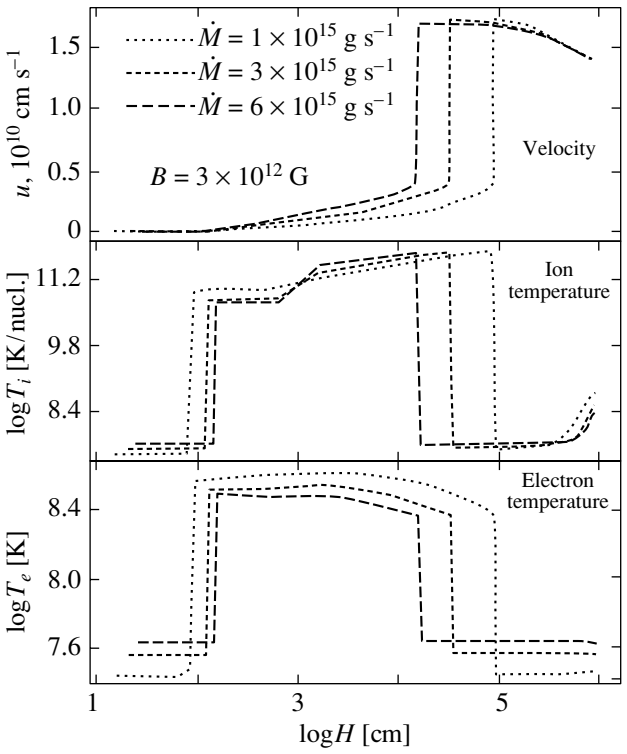

Fig. 4. Dependence of the flow profiles at $\tau = 5 \times 10^{-4}$ s on the accretion rate.

The model flow profiles shown in Figs. 3 and 4 exhibit stable and strong shocks that decelerate and heat the accretion flow. The ions at such shocks heat up much more strongly than the electrons, because they contain the bulk of the flow kinetic energy. However, as the heated ions move further toward the surface, they give up much of their energy to the electrons, which, in turn, release their energy in the form of cyclotron and bremstrahlung photons and give it up to the nonresonant photons in Compton collisions.

In most cases, the compression ratio at the shock fronts slightly exceeds 4 (the maximum value for nonrelativistic single-fluid shocks) because of the mildly relativistic changes in the adiabatic index of the ions heated to several tens of MeV.

An important property of the model is the transformation of a substantial fraction of the flow energy into the energy of photons in an optically thick electron cyclotron line. This fraction is plotted against the NS magnetic field strength in Fig. 5. The pressure of the trapped cyclotron radiation is dynamically significant for the deceleration of the accretion flow. The cyclotron ion cooling is significant for magnetic fields stronger than 5×10^{11} G. In this case, the accretion regime depends significantly on the structural features of the magnetic fields in the NS atmosphere at heights of less than 10^3 cm from the surface. At these heights, the field can differ greatly from a dipole field due to the local fields of higher multipolarity. A nonuniform field structure makes the column transparent to optical and X-ray photons of the proton and electron cyclotron radiation. Figure 6 shows the accretion regimes in the optically thin case where the ion cyclotron radiation freely escapes from the column. Allowing for the cyclotron ion cooling leads to the shock front approaching the NS surface if the dipole magnetic field exceeds 5×10^{11} G. In this case, the radiation spectrum of the system exhibits a prominent optical/ultraviolet proton cyclotron line. Because of the strong deceleration and effective cooling of the flow in the column in the optically thin case, only about half of the accretion flow energy reaches the stellar surface (see Fig. 7).

If the magnetic field has a regular structure, the proton cyclotron line can become optically thick at heights of $\sim 10^3$ cm from the NS surface. In this case, the accretion regimes are similar to those in Fig. 3, since the collisionless relaxation with a high frequency restores the isotropy of the ion distribution function faster than does the radiative change in the transverse (with respect to the field) temperature.

It should be noted that the difference in the shapes of the flow profiles at low and high magnetic field strengths (Fig. 3) stems from the fact that the electron temperature downstream of the shock front is

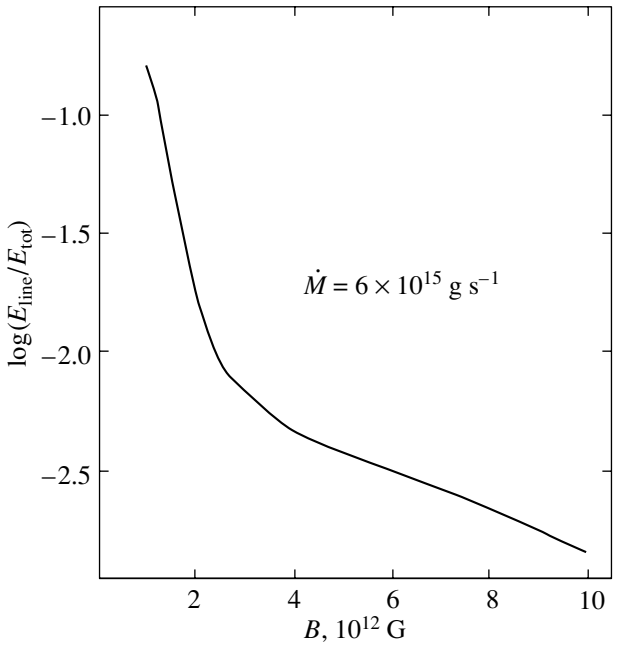

Fig. 5. Logarithm of the fraction of the flow free-fall energy converted into the energy of cyclotron radiation versus magnetic field strength.

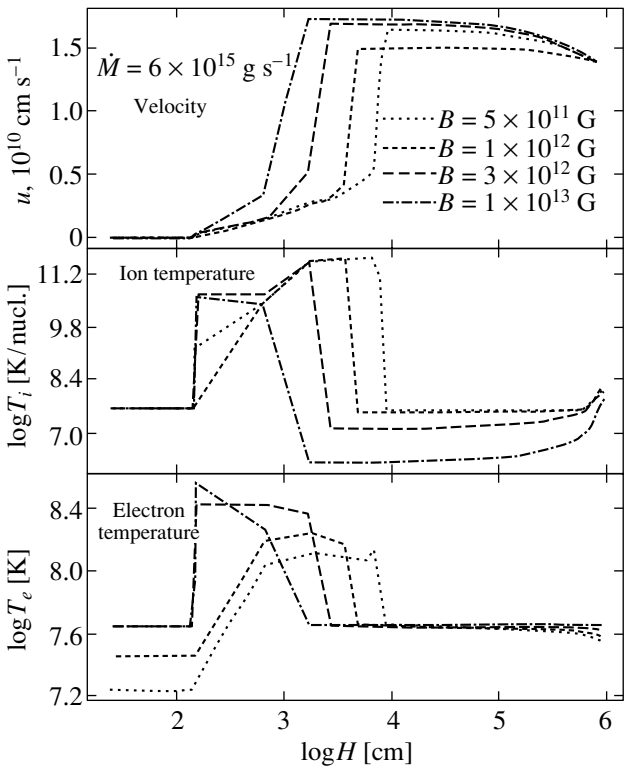

Fig. 6. Dependence of the flow profiles at $\tau = 0.8 \times 10^{-3}$ s on the magnetic field strength for the case where the column is optically thin for the cyclotron photons emitted by ions.

lower for weak fields. Therefore, the gradient in the energy density of the photons trapped in the cyclotron line increases toward the surface, providing a radiative pressure that contributes to a more effective flow deceleration.

2. THE DESTRUCTION OF CNO NUCLEI IN THE ACCRETION COLUMN

The chemical composition of the material that reaches the NS surface is an important question in the theory of accretion flows. This question is important, in particular, for the theory of X-ray bursts, because the CNO nuclei are the catalyst for the thermonuclear hydrogen burning reaction on the NS surface (see Lewin *et al.* (1993) and references therein). It is well known that the spallation reactions of nuclei with energies of several tens of MeV per nucleon or higher in the accretion flows of compact sources may lead to the destruction of nuclei and to a significant decrease in the gamma-ray fluxes in lines (see, e.g., Aharonian and Sunyaev 1984; Bildsten *et al.* 1992). This question was considered by Bildsten *et al.* (1992) for the case where the accretion flow decelerates in a dense NS atmosphere through Coulomb losses. These authors conclude that almost all of the CNO nuclei will be destroyed before they reach the NS surface. However, they note that this conclusion may be invalid in cases where the flow decelerates in the column above the atmosphere.

There is a fundamental possibility of collisionless flow deceleration through collective plasma effects and effective energy removal by electron radiation in a magnetic field. In this case, the thickness of the material traversed by a nucleus as it decelerates to energies of ~10 MeV per nucleon can be appreciably smaller than the thickness traversed by a nucleus in the case of its purely Coulomb deceleration to the same energy. Having constructed the model density, velocity, and ion temperature profiles in the column, we can answer the question of how effective the destruction of CNO nuclei in the accretion flow is and where they are destroyed.

To quantitatively verify this effect, we calculated the destruction probability of a carbon nucleus that was accreting together with the flow (since the nitrogen and oxygen destruction cross sections are close to the carbon destruction cross section, the destruction of these nuclei will be similar).

We numerically integrated the cross section for the destruction of carbon nuclei by protons determined by Read and Viola (1984) and obtained the frequencies of the destroying collisions per unit volume. We then calculated the dependences of the optical depths with respect to destruction and the destruction probabilities on the distance to the NS surface.

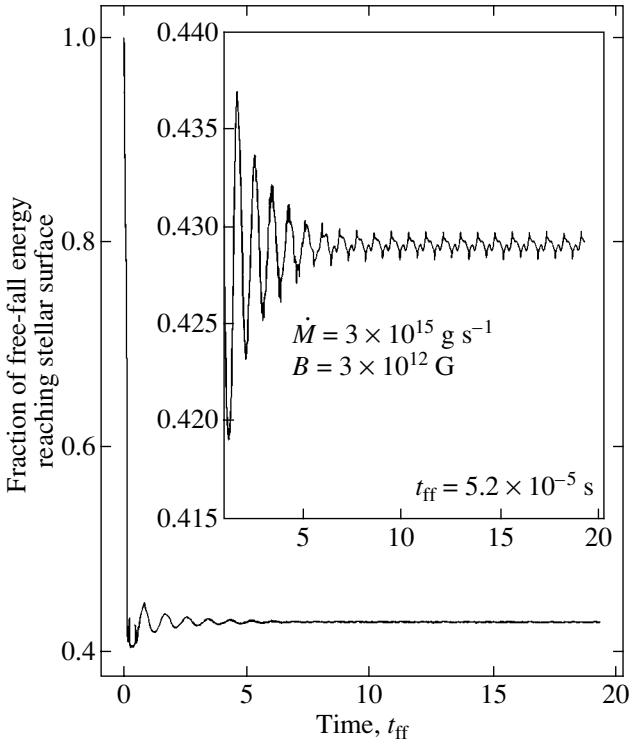

Fig. 7. Time evolution of the fraction of the flow energy that reaches the stellar surface.

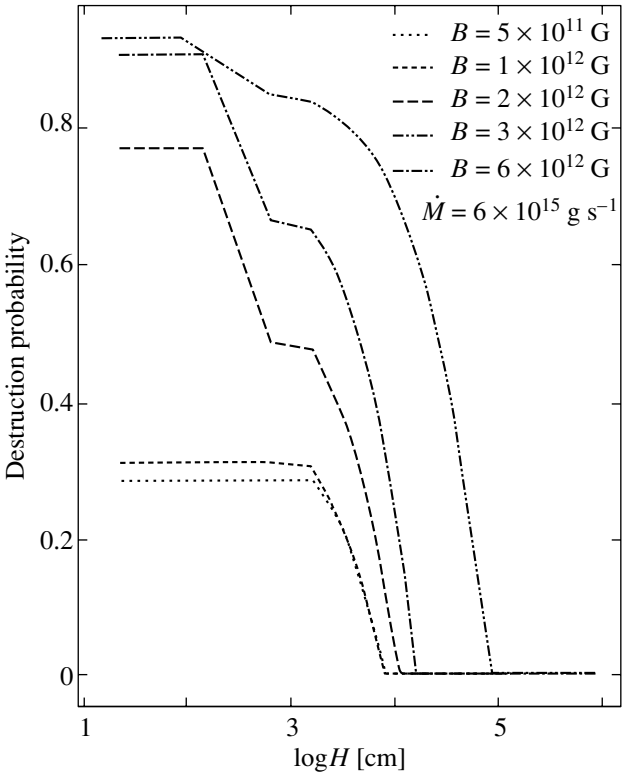

Fig. 8. Destruction probability of a ^{12}C nucleus versus distance to the stellar surface.

The destruction probability of a carbon nucleus is plotted against the distance to the NS surface in Fig. 8 for a set of magnetic field strengths at the NS pole. It follows from this figure that, for moderately strong magnetic fields, a significant fraction of the nuclei can reach the stellar surface and, hence, can be the catalyst for X-ray bursts.

CONCLUSIONS

We have constructed a numeral model for the unsteady accretion of material in a one-dimensional column above the polar region of a magnetized NS. The model gives a two-fluid description of the plasma accretion flow in a strong dipole magnetic field. The model is unique in that it uses the Godunov method for numerically integrating the flows of matter with discontinuities in the form of shocks. Using this method, we have been able to reveal and investigate the time evolution of the shocks in the plasma accretion flow. A steady flow with an accretion shock is established after a period on the order of several plasma free-fall times. The ion temperature abruptly increases at the shock front to $\sim 10^{11}$ K, which weakly depends on the magnetic field strength and the accretion rate. Depending on the magnetic field strength, the electron temperature reaches $(3–5) \times 10^8$ K.

Part of the accretion flow energy transforms into the energy of cyclotron radiation in an optically thick line whose pressure affects significantly the plasma flow deceleration. In this case, a substantial fraction of the flow kinetic energy is released in the form of optically thin radiation without reaching the bottom of the column. It is commonly assumed that the kinetic energy of the flow and the radiation from the optically thin part of the column that reach the bottom of the column transform into blackbody radiation in the optically thick region of the NS atmosphere. The radiation of the accretion flow energy in the optically thin part of the column leads to a tangible decrease in the effective temperature of the blackbody radiation from the polar spot $T_{\rm eff}$. In general, the *a priori* dependence $T_{\rm eff} \propto \dot{M}^{1/4}$ breaks down, since the fraction of the energy radiated in the optically thin part of the column is a complex function of $\dot{M}$.

ACKNOWLEDGMENTS

We wish to thank S.P. Voskoboĭnikov, A.E. Kalina, Yu.A. Kurakin, K.P. Levenfish, A.Yu. Potekhin, Yu.A. Uvarov, D.G. Yakovlev, and the participants of V.S. Imshennik's workshop for their helpful discussions and advice. We are grateful to the referees

for their constructive suggestions. This work was supported by the INTAS-ESA grant no. 99-1627 and the Russian Foundation for Basic Research (project no. 01-02-16654, 03-02-17433, and 03-07-90200).

APPENDIX

THE RATES OF PARTICLE–FIELD ENERGY EXCHANGE

(1) We use the cooling rates in the case of small-angle scattering H_{ei} (and $H_{ie} = -H_{ei}$) from Langer and Rappoport (1982):

$$H_{ei} = 2\sqrt{\frac{2}{\pi}} r_0 n_e n \xi \frac{T_i - T_e}{T_e + \xi T_i} Z^2 \sqrt{\frac{m_e c^2}{k_\mathrm{B}(T_e + \xi T_i)}} \Lambda, \tag{A.1}$$

where Λ is the Coulomb logarithm, and $r_0 = 4\pi r_e^2 m_e c^3$ is the characteristic energy loss scale in this process.

(2) To calculate the cooling rates Q_cyc and Cyc_{ei}, we numerically integrated the total quantum-electrodynamic cross section for the collisional excitation of electron Landau levels in a strong magnetic field from Langer (1981). To obtain an acceptable result over wide ranges of temperatures and magnetic field strengths, we took into account the excitation of the first ten Landau levels in the integration.

(3) To calculate Cyc_{ee}, we used a fitting formula from Langer and Rappoport (1982):

$$Cyc_{ee} = 2.04 r_0 n_e^2 B_{12}^{-1/2} \sqrt{\frac{k_\mathrm{B} T_e}{\hbar \omega_B}} \times \exp\left\{ -\frac{m_e c^2}{k_\mathrm{B} T_e} (\sqrt{1 + 0.04531 B_{12}} - 1) \right\} \times \left(\frac{B_{12}}{5}\right)^{\left(\frac{k_\mathrm{B} T_e}{9597\ \mathrm{keV}}\right)^{0.2}}. \tag{A.2}$$

(4) To calculate the bremsstrahlung cooling rate Br_{ee}, we numerically integrated the cross section from Haug (1975) and derived the fitting formula

$$Br_{ee} \approx 2.5410 \times 10^{-37} T_e^{1.45811} n_e^2 g(B, T_e), \tag{A.3}$$

where $g(B, T_e) = (0.409 - 0.0193 B_{12} - 0.00244 B_{12}^2) \times (k_\mathrm{B} T_e / 10\ \mathrm{keV})^{0.25}$ is the Gaunt factor from Langer and Rappoport (1982).

(5) To calculate the bremsstrahlung cooling rate Br_{ei}, we numerically integrated the cross section from the book by Berestetskii *et al.* (1980) for high electron temperatures and used the fit from Langer and Rappoport (1982) for low electron temperatures:

$$Br_{ei} \approx \begin{cases} 0.36 \alpha r_0 (T_e / T_e^b)^{0.5} n_e n_i Z^2 g(B, T_e), & T_e < T_e^b \\ 0.36 \alpha r_0 (T_e / T_e^b)^{1.2} n_e n_i Z^2 g(B, T_e), & T_e \geq T_e^b, \end{cases} \tag{A.4}$$

where $T_e^b = 5 \times 10^8$ K.

(6) Q_relax denotes the Coulomb relaxation of the accretion flow on electrons of the thin and dense NS atmosphere. We used the simple model of an isothermal atmosphere and determined Q_relax as

$$Q_\mathrm{relax} = -\nu_{ei} \frac{k_\mathrm{B} n_i}{\gamma_i - 1} (T_i - T_\mathrm{atm}), \tag{A.5}$$

where ν_{ei} is the Coulomb collision frequency.

(7) Q_compt denotes the electron cooling in single Compton scatterings. For moderately hard photons ($\frac{\gamma E_\gamma}{m_e c^2} \ll 1$) that scatter nonrelativistic electrons, the energy lost by an electron in a single nonresonant scattering is $\Delta E = -\frac{E_\gamma^2}{m_e c^2} + \frac{4 k_\mathrm{B} T_e E_\gamma}{m_e c^2}$. Since $\langle E_\gamma \rangle = 3 k_\mathrm{B} T_\gamma$, $\langle E_\gamma^2 \rangle = 12 k_\mathrm{B} T_\gamma^2$,

$$Q_\mathrm{compt} = n_e n_\gamma \langle \sigma_\mathrm{T} v_\mathrm{rel} \Delta E \rangle H(B, T_\gamma) = 12 n_e n_\gamma \sigma_\mathrm{T} c k_\mathrm{B} T_\gamma k_\mathrm{B} \frac{T_e - T_\gamma}{m_e c^2} H(B, T_\gamma), \tag{A.6}$$

where $H(B, T_\gamma) = (1 + 0.0165(\hbar \omega_\mathrm{B} / k_\mathrm{B} T_\gamma)^{2.48}) / (1 + 0.0825(\hbar \omega_\mathrm{B} / k_\mathrm{B} T_\gamma)^{2.48})$ is the Gaunt factor for the process under consideration from Arons *et al.* (1987); and n_γ and T_γ are the local density and temperature of the photon field, respectively.

REFERENCES

1. F. A. Aharonian and R. A. Sunyaev, Mon. Not. R. Astron. Soc. **210**, 257 (1984).
2. J. Arons, R. I. Klein, and S. M. Lea, Astrophys. J. **312**, 666 (1987).
3. M. M. Basko and R. A. Sunyaev, Mon. Not. R. Astron. Soc. **175**, 395 (1976).
4. V. B. Berestetskiĭ, E. M. Lifshits, and L. P. Pitaevskiĭ, *Quantum Electrodynamics*, 2nd ed. (Nauka, Moscow, 1980; Pergamon, Oxford, 1982).
5. L. Bildsten, E. E. Salpeter, and I. Wasserman, Astrophys. J. **384**, 143 (1992).
6. G. S. Bisnovatyĭ-Kogan and A. M. Fridman, Astron. Zh. **46**, 721 (1969) [Sov. Astron. **13**, 566 (1970)].

7. A. Braun and R. Z. Yahel, Astrophys. J. **278**, 349 (1984).
8. R. W. Bussard, Astrophys. J. **237**, 970 (1980).
9. K. Davidson and J. P. Ostriker, Astrophys. J. **179**, 585 (1973).
10. J. Frank, A. King, and D. J. Raine, *Accretion Power in Astrophysics* (Cambridge Univ. Press, 2002).
11. C. W. Gear, *Numerical Initial Value Problems in Ordinary Differential Equations* (Prentice-Hall, Englewood Cliffs, 1971).
12. S. K. Godunov, Mat. Sb. **47**, 271 (1959).
13. S. K. Godunov, A. V. Zabrodin, M. Ya. Ivanov, *et al., Numerical Integration of Multidimensional Gas-Dynamic Problems* (Nauka, Moscow, 1976) [in Russian].
14. S. De Groot, W. van Leeuwen, and Ch. van Weert, *Relativistic Kinetic Theory* (North-Holland, Amsterdam, 1980; Mir, Moscow, 1983).
15. E. Haug, Z. Naturforsch. **30**, 1099 (1975).
16. A. C. Hindmarsh, ODEPACK: *A Systematized Collection of ODE Solvers, Scientific Computing,* Ed. by R. S. Stepleman *et al.* (North-Holland, Amsterdam, 1983), p. 55.
17. R. I. Klein and J. Arons, in *Proceedings of the 23rd ESLAB Symposium on Two-Topics in X-ray Astronomy,* Ed. by N. White (ESA, Noordwijk, 1989), p. 89.
18. R. I. Klein, J. Arons, J. Garrett, and J. J.-L. Hsu, Astrophys. J. **457**, L85 (1996).
19. S. H. Langer, Phys. Rev. D **23**, 328 (1981).
20. S. H. Langer and S. Rappoport, Astrophys. J. **257**, 733 (1982).
21. R. J. Le Veque, J. Comput. Phys. **131**, 327 (1997).
22. W. H. G. Lewin, J. van Paradijs, and R. E. Taam, Space Sci. Rev. **62**, 223 (1993).
23. W. H. Press, B. P. Flannery, S. A. Teukolsky, and W. T. Vetterling, *Numerical Recipes in FORTRAN 77: The Art of Scientific Computing* (Cambridge Univ. Press, 1993).
24. S. M. Read and V. E. Viola, At. Data Nucl. Data Tables **31**, 359 (1984).
25. E. E. Salpeter, Astrophys. J. **140**, 796 (1964).
26. N. I. Shakura and R. A. Sunyaev, Astron. Astrophys. **24**, 337 (1973).
27. S. L. Shapiro and E. E. Salpeter, Astrophys. J. **198**, 671 (1975).
28. A. L. Velikovich and M. A. Liberman, *Physics of Shock Waves in Gases and Plasma* (Nauka, Moscow, 1987) [in Russian].
29. A. V. Zabrodin and G. P. Prokopov, Vopr. At. Nauki Tekh., Ser.: Mat. Model. Fiz. Prots. **3**, 3 (1998).
30. Ya. B. Zel'dovich, Dokl. Akad. Nauk SSSR **155**, 67 (1964) [Sov. Phys. Dokl. **9**, 195 (1964)].
31. Ya. B. Zel'dovich, *IAU Meeting XIII* (Prague, 1967).
32. Ya. B. Zel'dovich and N. I. Shakura, Astron. Zh. **46**, 225 (1969) [Sov. Astron. **13**, 175 (1969)].
33. V. V. Zheleznyakov, *Radiation in Astrophysical Plasma* (Yanus-K, Moscow, 1997) [in Russian].

Translated by V. Astakhov

Astronomy Letters, Vol. 30, No. 5, 2004, pp. 319–324. Translated from Pis'ma v Astronomicheskiĭ Zhurnal, Vol. 30, No. 5, 2004, pp. 362–367.

Pulsating Microwave Emission from the Star AD Leo

V. V. Zaĭtsev[1*], A. G. Kislyakov[1,2], A. V. Stepanov[3], B. Kliem[4], and E. Fürst[5]

[1] *Institute of Applied Physics, Russian Academy of Sciences, ul. Ul'yanova 46, Nizhni Novgorod, 603950 Russia*

[2] *Lobachevskiĭ State University, ul. Gagarina 23, Nizhni Novgorod, 603950 Russia*

[3] *Pulkovo Astronomical Observatory, Russian Academy of Sciences, Pulkovo, St. Petersburg, 196140 Russia*

[4] *Astrophysikalisches Institut, An der Sternwarte 16, D-14482 Potsdam, Germany*

[5] *Max-Planck-Institut für Radioastronomie, Auf dem Hügel 69, D-53121 Bonn, Germany*

Received July 10, 2003

Abstract—We have performed a spectral analysis of the quasi-periodic low-frequency modulation of microwave emission from a flare on the star AD Leo. We used the observations of the May 19, 1997 flare in the frequency range 4.5–5.1 GHz with a total duration of the burst phase of about 50 s obtained in Effelsberg with a time resolution of 1 ms. The time profile of the radio emission was analyzed by using the Wigner–Ville transformation, which yielded the dynamic spectrum of low-frequency pulsations with a satisfactory frequency–time resolution. In addition to the noise component, two regular components were found to be present in the low-frequency modulation spectrum of the stellar radio emission: a quasi-periodic component whose frequency smoothly decreased during the flare from ~2 to ~0.2 Hz and a periodic sequence of pulses with a repetition rate of about 2 Hz, which was approximately constant during the flare. We consider the possibility of the combined effect of MHD and LCR oscillations of the radio source on the particle acceleration in the stellar atmosphere and give estimates of the source's parameters that follow from an analysis of the low-frequency modulation spectra. © *2004 MAIK "Nauka/Interperiodica".*

Key words: *stars: properties, classification; flares, radio emission, low-frequency modulation, dynamic spectrum.*

INTRODUCTION

The flare radio emission from the active red dwarf AD Leo, which is 4.85 pc away from the Solar system and has the radius $R = 3.5 \times 10^{10}$ cm (approximately half the solar radius), has been repeatedly observed with large radio telescopes at frequencies of 1.3–5 GHz. The observations revealed quasi-periodic pulsations with periods of 1–10 s against the continuum background (Güdel *et al.* 1989; Bastian *et al.* 1990; Abada-Simon *et al.* 1995; Stepanov *et al.* 2001). The modulation depth in the pulsations can occasionally reach 50%; the radio brightness temperatures lie within the range 10^{10}–10^{13} K and provide evidence for coherent mechanisms of radio emission from the star during its flares. Phenomenologically, the radio pulsations of AD Leo are, to some extent, similar to pulsed type-IV solar radio bursts. This has prompted attempts to explain the pulsations of AD Leo by pulsed modes of plasma instabilities (Güdel *et al.* 1989) and by MHD oscillations of magnetic arches in the stellar corona. The pulsation frequency drift from high to low frequencies (Stepanov *et al.* 2001) provides evidence for the quasi-periodic injection of fast electron beams from the lower stellar atmosphere into the radio source. Zaitsev (1999) attributed the acceleration of electrons to the electric fields that resulted from convective motions at the feet of magnetic loops in the stellar atmosphere, while the modulation of the acceleration process was attributable to oscillations of the loop magnetic field. However, it remains unclear what specific types of free oscillations of coronal magnetic loops (CML) affect the modulation of the radio emission most strongly.

In this paper, we analyze the quasi-periodic low-frequency (LF) modulation of the microwave emission from AD Leo during its flare of May 19, 1997. We applied the Wigner–Ville transformation to the time profile of the radio emission to obtain the dynamic LF pulsation spectra with a high spectral–temporal resolution. We found two regular components in the LF modulation of the radio emission: a harmonic component whose frequency gradually decreased during the flare and a periodic sequence of pulses with an approximately constant repetition rate. In Section 1, we present the results of our spectral analysis of the time profile for the microwave emission of the flare

*E-mail: za130@appl.sci-nnov.ru

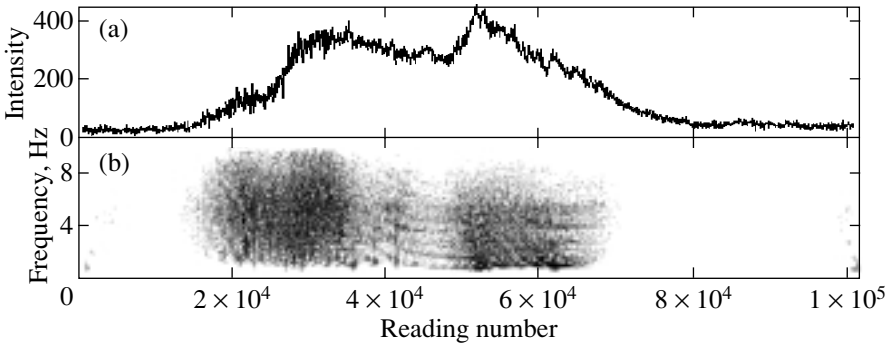

Fig. 1. (a) Time profile of the radio emission from AD Leo at 4.85 GHz in right-hand circular polarization (May 19, 1997, ~18.945 UT). (b) Dynamic low-frequency (0–9 Hz) modulation spectrum for the microwave emission from AD Leo obtained by using the Wigner–Ville transformation.

of May 19, 1997, from AD Leo. In Section 2, we interpret the dynamic spectra and features of the LF pulsations that modulate the microwave emission. In Section 3, we discuss the diagnostic possibilities of the LF pulsations using the flare of May 19, 1997, as an example.

1. OBSERVATIONAL DATA

We studied the flare from the red dwarf AD Leo detected on May 19, 1997 (18.945 UT), in the frequency range 4.6–5.1 GHz with the 100-m Effelsberg radio telescope. Figure 1a shows the time profile of the radio emission at 4.85 GHz. The emission with a flux of 300 mJy at the burst peak is present only in right-hand circular polarization. The total duration of the burst phase is about 50 s. The time resolution of the digital record is 1 ms. The time profile shows fluctuations of the radio flux with a modulation depth from several to 10%; in the dynamic spectrum of the burst in the range 4.6–5.1 GHz, they have the pattern of irregular pulsations with a large frequency drift rate (Stepanov *et al.* 2001). A preliminary Fourier analysis revealed several maxima in the pulsation spectrum; however, it is difficult to draw any conclusions about the nature of the LF modulation from them (see Fig. 4 from Stepanov *et al.* 2001). We applied the Wigner–Ville transformation (see Wigner 1932; Ville 1948) to the time profile of the burst to study the evolution of the LF spectrum with time. The Wigner–Ville transformation is the Fourier transformation of the symmetric shape of the local autocorrelation function for the analytic signal produced by the real signal under study with the signal realization shifted relative to itself (i.e., the integration is over the shift time). This makes it possible to determine the energy distribution of the signal in the time–frequency plane, i.e., the dynamic spectrum of the signal. Although the Wigner–Ville transformation has been known for more than 50 years, it has come into use for processing nonstationary signals only relatively recently (see the review by Cohen 1989).

Figure 1b shows the dynamic LF modulation spectrum of the right-hand-polarized emission. We see from Fig. 1b that, in addition to the noise component, narrow-band ($\Delta\nu/\nu \leq 0.1$) drifting signals in the frequency bands 0.5–2, 1.5–3, 2.5–4, 3.5–5, and 4.5–6 Hz appear in the region where the intensity of the first radio burst decreases. The signals in the dynamic spectrum are nearly equidistant with a band separation of about 1 Hz. Each of the signals exhibits a negative frequency drift. Initially, the frequency drift rate is relatively high ($d\nu/dt \approx -0.3$ Hz s^{-1}) and then decreases sharply to $d\nu/dt \approx -0.05$ Hz s^{-1}. In the flat segments of the dynamic spectrum, the signals show a frequency splitting $\delta\nu \approx 0.2$–0.3 Hz.

Figure 2 shows the dynamic spectrum of the drifting LF signals described above on an enlarged scale. Similar LF modulation signals are also excited on the descending branch of the second radio pulse, but their parameters (the duration and frequency drift rate) differ slightly. This may be interpreted as a "fault" in the parameters of the LF oscillations. The physical cause of this phenomenon could be either a change in the CML parameters after the first emission peak (e.g., through the evaporation of chromospheric plasma) or the turning-on of enhanced emission from another coronal loop. A detailed analysis of this mechanism is beyond the scope of this paper.

2. DISCUSSION

The observed LF oscillations are probably not the natural oscillations of the 100-m radio telescope with a period of ≈1 s, because there is a clear correlation of the occurrence time of the pulsations with the time profile of the radio emission, while the observed frequency drift and the pulsation frequency differ from the eigenfrequency of the radio telescope.

2.1. Interpretation of the Dynamic Spectra

Here, we will determine what types of disturbances yield the dynamic LF pulsation spectra shown in Fig. 2. Since the Wigner–Ville transformation used to obtain these spectra is nonlinear, we need an algorithm that would allow the correspondence between the observed dynamic spectra and the type of LF modulation to be established. In general, this algorithm is worked out by finding the Wigner–Ville diagram from various known signals and comparing their dynamic spectra with the observed spectra. This method was used, in particular, by Zaĭtsev *et al.* (2001a, 2001b) to analyze the LF pulsations of solar microwave bursts. Our modeling shows that the dynamic spectra of Fig. 2 correspond to the simultaneous action of two types of modulation on the radio source: (1) modulation by a narrow-band ($\Delta\nu/\nu \leq 0.1$) harmonic signal whose frequency gradually decreases from ~2 to 0.3–0.5 Hz ($\nu_1 = 2 \rightarrow 0.5$ Hz), which is here called an LFM (linear frequency modulation) signal for short; and (2) modulation by a periodic sequence of short pulses with a repetition rate $\nu_2 \approx 2$ Hz. The periodic sequence of pulses, whose spectrum is a system of equidistant bands (spaced by $\sim\nu_2/2$), interacts with the LFM signal described above and also generates a system of equidistant bands shifted relative to the first system by a frequency $\nu_1/2$. This is because the Wigner–Ville transformation is nonlinear (see, e.g., Shkelev *et al.* 2002).

Thus, we consider below the causes of the simultaneous appearance of two types of modulation in the radio source of AD Leo. The first type is a quasi-harmonic wave with a frequency $\nu_1 = 2 \rightarrow 0.5$ Hz. The second type is a periodic sequence of short pulses with a repetition rate $\nu_2 \approx 2$ Hz.

2.2. Modulation Mechanisms

The analysis of the mechanisms of the radio emission from the flare of May 19, 1997, carried out by Stepanov *et al.* (2001) has shown that, of the two coherent mechanisms (the plasma and maser cyclotron ones), the plasma mechanism of radio emission from CML with a plasma density $n \simeq 2.3 \times 10^{11}$ cm^{-3}, temperature $T = 3 \times 10^7$ K, and magnetic field $B \approx 730$–810 G is most likely.[1] These values are consistent with the available data on the coronas of red dwarfs. Thus, for example, the observed emission measures of the soft coronal X-ray emission (Schmitt 1997; Schmitt *et al.* 1990; Hawley *et al.* 1995) yield temperatures $T > 2 \times 10^7$ K, the estimated plasma densities lie within the range 3×10^{12} cm^{-3} to 5×10^9 cm^{-3} (Monsignori Fossi and Landini 1994; Katsova *et al.* 1987), and the photospheric magnetic fields on AD Leo can reach 3800 G and occupy up to 75% of the stellar surface (Saar and Linsky 1985). The coronas can be highly nonuniform and can include magnetic loops of various scales and intrinsic parameters (White *et al.* 1994). The presence of external convection zones in red dwarfs can probably lead to the generation of powerful electric currents inside magnetic loops, much as is the case in flare CMLs on the Sun (Zaitsev *et al.* 1998).

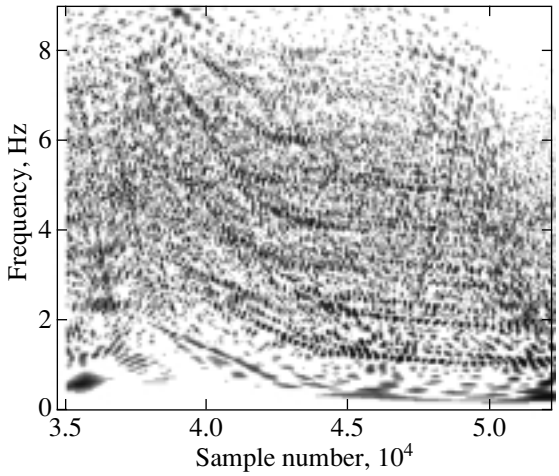

Fig. 2. A portion of the dynamic low-frequency modulation spectrum obtained for times at the descending branch of the time profile for the first radio pulse. Nearly equidistant, frequency-drifting narrow-band signals with frequency splitting are seen.

Below, in analyzing the modulation of the radio emission from AD Leo, we use the above plasma parameters determined by Stepanov *et al.* (2001) for the event of May 19, 1997. For these parameters, the Alfvén velocity in CML is $V_A = B(4\pi n m_i)^{-1/2} \approx 3.5 \times 10^8$ cm s^{-1}, where m_i is the ion mass. Therefore, we may immediately exclude from our analysis the Alfvén and kink CML oscillations as well as the nonlinear generation modes of plasma waves. For the first two types of oscillations, the frequency is of the order of $\nu_A \approx \nu_k \approx V_A/2\ell \approx 2 \times 10^{-2}$ Hz for a loop length $\ell \approx 10^{10}$ cm. This value is approximately an order of magnitude lower than the observed modulation frequency. In contrast, the nonlinear generation modes of plasma waves yield frequencies (Güdel *et al.* 1989) of the order of $\nu_N \approx 0.1\nu_{ei} \approx 10$ Hz, which are much higher than the observed modulation frequency (here,

[1] Here, we use the term "coherent" in the sense that, in this case, the observed emission is related to plasma instabilities, and not to the thermal emission of plasma, as suggested by the high (up to 10^{13} K) effective temperatures of the emission from the active region on the star.

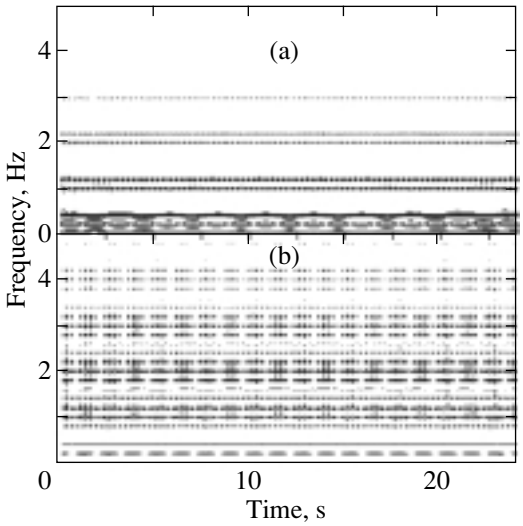

Fig. 3. Modeling of the low-frequency modulation of the radio emission from AD Leo by the Wigner–Ville transformation for signals of two types: the superposition of a periodic sequence of pulses (repetition period 0.5 s) and a sine wave with a frequency of 0.4 Hz (a) and the same sequence of pulses modulated in amplitude by an oscillation with a frequency of 0.4 Hz (b).

$\nu_{ei} \approx 10^2$ Hz is the effective frequency of electron–ion collisions in the radio source of AD Leo).

The best agreement with the observational data is given by radial fast magnetosonic (FMS) CML oscillations with the frequency

$$\nu_{FMS} = \frac{V_A}{r_0}, \quad (1)$$

where $2r_0$ is the loop diameter, and by oscillations of the loop as an equivalent electric circuit with the frequency (Zaitsev *et al.* 1998)

$$\nu_{LCR} \approx \frac{1}{\sqrt{\pi\Lambda}}\left(1 + \frac{c^2 r_0^2 B_z^2}{4I_z^2}\right)^{1/2} \frac{I_z}{2cr_0^2\sqrt{\pi n m_i}}, \quad (2)$$

where

$$\Lambda = \ln\frac{4\ell}{\pi r_0} - \frac{7}{4}, \quad (3)$$

I_z is the total electric current flowing along the loop through its cross section, c is the speed of light, and B_z is the magnetic field strength along the loop axis. The dependence of ν_{LCR} on the current I_z stems from the fact that the equivalent capacity of the loop is determined not only by B_z, but also by the B_φ component of the magnetic field in the loop.

If a flare process takes place in the loop, then the current I_z decreases with time. In this case, the frequency ν_{LCR} also decreases. When the current satisfies the inequality $I_z \ll cr_0B_z/2$, which corresponds to the condition of weak magnetic field twisting in the loop, $B_\varphi \ll B_z$, the frequency ν_{LCR} depends weakly on the current. Thus, at a certain time, the frequency drift rate $d\nu_{LCR}/dt$ must experience a break and decrease sharply. This occurs when the condition $I_z(t) < cr_0B_z/2$ is satisfied. The dynamic spectra in Fig. 2 exhibit a similar time dependence of the frequency drift rate. This circumstance, as well as the possibility of associating the negative frequency drift with a specific physical process (the dissipation of the electric current in the magnetic loop during a flare), allows us to assume that the drifting bands in Fig. 2 are related to the modulation produced by the excitation of oscillations of the magnetic trap as an equivalent electric circuit. Therefore, we assume that

$$\nu_1(t) = \nu_{LCR}(t). \quad (4)$$

It is easy to verify that the frequency ν_{LCR} is always lower than the FMS oscillation frequency ν_{FMS}. Therefore, we will associate the higher of the observed modulation frequencies (more specifically, the repetition rate of short pulses) with the FMS oscillations of the magnetic loop and assume that

$$\nu_2 = \nu_{FMS}. \quad (5)$$

Thus, we assume that precisely this frequency determines the separation between the "equidistant" lines of the dynamic LF pulsation spectrum in Fig. 2.

2.3. Modulation Modes

Two distinct modes of modulation of the radio emission originating in CML are possible:

(1) an independent combined modulation by a periodic sequence of short pulses with frequency ν_{FMS} and by a harmonic LCR oscillation with frequency ν_{LCR} (the superposition of oscillations);

(2) a modulation by short pulses with a repetition rate ν_{FMS}, the amplitude of which periodically varies with frequency ν_{LCR} (the amplitude modulation of pulses).

To determine which of these modes was realized in the event of May 19, 1997, we have compared the Wigner–Ville transformations for these two cases. Figures 3a and 3b present the results of this comparison. Figure 3a shows the dynamic spectrum for the former case (the superposition of oscillations) at $\nu_{FMS} = 2$ Hz and $\nu_{LCR} = 0.4$ Hz, and Fig. 3b shows the dynamic spectrum for the latter case (the amplitude modulation of pulses) at the same frequencies. We see that the Wigner–Ville transformation yields a frequency splitting into two components for the equidistant lines of the spectrum of periodic pulses in the former case and a splitting of a more complex pattern in the latter case. Since we observed a double

splitting in the experiment (see Fig. 2), we conclude that, in the event of May 19, 1997, there was an independent modulation by a harmonic oscillation and by a periodic sequence of short pulses (the superposition of two oscillations).

3. PARAMETERS OF THE FLARE MAGNETIC LOOP IN THE CORONA OF AD Leo

Let us consider the diagnostic possibilities provided by the dynamic LF pulsation spectra of the microwave emission from flares on AD Leo. In Section 2.2, we have already mentioned that our analysis of the mechanism of the microwave emission from the flare of May 19, 1997, led us to conclude that the source of radio emission is probably a CML, with the plasma mechanism and high polarization yielding a ratio of the gyrofrequency to the plasma frequency inside the loop $\omega_{Be}/\omega_p \approx 0.5$. Thus, the Alfvén velocity is

$$V_A = 7 \times 10^8 \frac{\omega_{Be}}{\omega_p} = 3.5 \times 10^8 \text{ cm s}^{-1}.$$

Therefore, the value of $\nu_2 = \nu_{FMS} \simeq 2$ Hz found from the dynamic spectra allows us to determine the CML radius:

$$r_0 = \frac{V_A}{\nu_{FMS}} \simeq 1.75 \times 10^8 \text{ cm}. \quad (6)$$

In this case, the loop thickness, $d \approx 3.5 \times 10^8$ cm, is comparable to that of the solar flare magnetic loops (Bray *et al.* 1991).

Formulas (2)–(4) allow us to estimate the magnetic loop length ℓ, because the LCR oscillation frequency depends on it via the equivalent loop inductance. It follows from (2) that the break in the frequency drift rate occurs at

$$\nu_{LCR}(I_z = cr_0 B_z/2) = \frac{1}{\sqrt{2\pi\Lambda}} \frac{V_A}{r_0}. \quad (7)$$

The frequency of the lower (main) LFM signal at the break time is ~ 0.4 Hz (see Fig. 1b). Assuming that $\nu_{LCR} = 0.4$ Hz and approximating the loop by a circle of radius $R = \ell/2\pi$, we obtain from (7)

$$\ell = 4.2 \times 10^{10} \text{ cm}. \quad (8)$$

The loop height, $h \approx 2R = 1.36 \times 10^{10}$ cm, is more than a third of the stellar radius, which is much larger than the solar flare magnetic loops. Note that the VLBI monitoring of red dwarfs confirms the presence of extended CMLs with sizes of the order of the stellar radius in stars of this type.

Taking $\nu_{LCR}^{max} \approx 2$ Hz (see Fig. 1b), we can estimate the electric current in the magnetic loop at the times corresponding to the peak of the first microwave pulse of the flare from AD Leo (Fig. 1a):

$$I_z^{max} \approx 2\pi c r_0^2 \nu_{LCR}^{max} \sqrt{n m_i \Lambda} \approx 4.5 \times 10^{12} \text{ A}. \quad (9)$$

In this case, the energy of the electric current stored in a magnetic loop with inductance (Alfvén and Carlquist 1967)

$$L \approx R\left(\ln\frac{8R}{r_0} - \frac{7}{4}\right) \approx 4R \simeq 2.7 \times 10^{10} \text{ cm}$$

is

$$W = \frac{LI_z^2}{2c^2} \approx 5.5 \times 10^{33} \text{ erg}. \quad (10)$$

This energy is released in a time of $\sim$1 min (the total duration of the burst phase), which yields an estimate of the rate of energy release $\dot{W} \simeq 10^{32}$ erg s^{-1}. This value is two to three orders of magnitude larger than the rate of energy release in solar flares.

Thus, we may conclude that the sources of flare microwave emission on the red dwarf AD Leo are in many aspects similar to the sources of solar microwave bursts. These are coronal magnetic loops that carry an electric current, which is the source of free energy for flares. The free oscillations of the magnetic loop as an MHD system and, at the same time, an equivalent electric circuit modulate the microwave emission, making it informative with regard to the geometrical sizes of the loop and the electric current inside the loop. The stored energy and the rate of energy release during the flares on AD Leo can exceed the corresponding values for the Sun by two to three orders of magnitude. The cause of this excess may be stronger magnetic fields on the surfaces of red dwarfs and more active surface convection.

ACKNOWLEDGMENTS

This work was supported by the Nonstationary Processes in Astronomy program of the Presidium of the Russian Academy of Sciences, the program Support for Leading Scientific Schools, the Federal Astronomy Program, and the Russian Foundation for Basic Research (project nos. 02-02-16239 and 01-02-16435).

REFERENCES

1. M. Abada-Simon, A. Lecacheux, M. Aubier, and J. Bookbiner, Lect. Notes Phys. **454**, 32 (1995).
2. H. Alfven and P. Carlquist, Sol. Phys. **1**, 220 (1967).
3. T. Bastian, J. Bookbiner, J. Dulk, and M. Davis, Astrophys. J. **353**, 265 (1990).
4. R. J. Bray, L. E. Cram, C. J. Durrant, and R. L. Longhead, *Plasma Loops in the Solar Corona* (Cambridge Univ. Press, London, 1991).
5. L. Cohen, Proc. IEEE **77**, 941 (1989).

6. M. Guedel, A. Benz, T. Bastian, *et al.*, Astron. Astrophys. **220**, L5 (1989).
7. S. L. Hawley, G. H. Fisher, T. Simon, *et al.*, Astrophys. J. **453**, 464 (1995).
8. M. M. Katsova, O. G. Badayan, and M. A. Livshits, Astron. Zh. **64**, 1243 (1987) [Sov. Astron. **31**, 652 (1987)].
9. B. C. Monsignori Fossi and M. Landini, Astron. Astrophys. **284**, 900 (1994).
10. S. H. Saar and J. L. Linsky, Astrophys. J. **299**, L47 (1985).
11. A. V. Stepanov, B. Kliem, V. V. Zaitsev, *et al.*, Astron. Astrophys. **374**, 1072 (2001).
12. E. I. Shkelev, A. G. Kislyakov, and S. Yu. Lupov, Izv. Vyssh. Uchebn. Zaved., Ser. Radiofiz. **45**, 433 (2002).
13. J. H. M. M. Schmitt, Astron. Astrophys. **318**, 215 (1997).
14. J. H. M. M. Schmitt, A. Callura, S. Sciortino, *et al.*, Astrophys. J. **365**, 704 (1990).
15. J. Ville, Cables Transm. **2A**, 61 (1948).
16. S. M. White, J. Lim, and M. R. Kundu, Astrophys. J. **422**, 293 (1994).
17. E. P. Wigner, Phys. Rev. **40**, 749 (1932).
18. V. V. Zaĭtsev, *Proc. VII Russian-Finnish Symp. on Radio Astronomy,* Ed. by A. V. Stepanov (The Main Astron. Obs., St. Petersburg, 1999).
19. V. V. Zaitsev, A. V. Stepanov, S. Urpo, and S. Pohjolainen, Astron. Astrophys. **337**, 887 (1998).
20. V. V. Zaĭtsev, A. G. Kislyakov, S. Urpo, and E. I. Shkelev, Izv. Vyssh. Uchebn. Zaved., Ser. Radiofiz. **44**, 38 (2001a).
21. V. V. Zaĭtsev, A. G. Kislyakov, S. Urpo, and E. I. Shkelev, Izv. Vyssh. Uchebn. Zaved., Ser. Radiofiz. **44**, 756 (2001b).

Translated by G. Rudnitskiĭ

Astronomy Letters, Vol. 30, No. 5, 2004, pp. 325–331. Translated from Pis'ma v Astronomicheskiĭ Zhurnal, Vol. 30, No. 5, 2004, pp. 368–375.

HD 183143: A Hypergiant

E. L. Chentsov*

Special Astrophysical Observatory, Russian Academy of Sciences, Nizhniĭ Arkhyz, 369167 Karachai-Cherkessian Republic, Russia

Received September 29, 2003

Abstract—We present spectroscopic evidence that the luminosity of HD 183143 is higher by one magnitude than thought previously. The star is yet another B6–8 Ia-0 white hypergiant of the Galaxy. Its absolute visual magnitude is close to -8^m, and its distance is close to 2 kpc. We describe spectroscopic manifestations of the nonstationary behavior of its atmosphere and wind. © *2004 MAIK "Nauka/Interperiodica".*

Key words: *stars: properties, classification; stellar wind, HD 183143, radial velocities.*

INTRODUCTION

White hypergiants, the most luminous late B and early A stars, are very rare. Only several such objects are known in our Galaxy: Cyg OB2-12 (B5 Ia-0), HD 168625 (B6 Ia-0), HD 168607 (B9 Ia-0), HD 92207 (A0 Ia-0), HD 223960 (A0 Ia-0), 6 Cas (A2.5 Ia-0), and two LBV variables, HR Car and HD 160529, at certain phases. A candidate for addition to this list is HD 183143 (MWC 317, HT Sge), a bright, highly reddened ($V = 6\overset{m}{.}8$, $(B-V) = 1\overset{m}{.}2$) B7-type star of a very high luminosity. Since its spectrum is rich in diffuse absorption bands of interstellar nature (DIBs), it was used as an introduction to the DIB problem (Herbig 1975, 1995) and has been repeatedly included in spectroscopic DIB atlases (Jenniskens and Desert 1994; Galazutdinov *et al.* 2000; Tuairisg *et al.* 2000). In our view, however, the star itself has not received proper attention.

Half a century ago, HD 183143 was suggested as a standard B7 Ia star in the MK system (Johnson and Morgan 1953). This estimate, which is quite accurate with respect to the spectral type but doubtful with respect to the luminosity class, has since been used in the overwhelming majority of papers. The problem is that it is based on low-dispersion spectrograms taken on blue-sensitive plates; this did not allow the peculiarities of the spectrum to be noticed. However, 20 years earlier, the star was presented in the first part of the MWC catalog, which contained stars with emissions in the hydrogen lines (Merrill and Burwell 1933). If we also consider the second part of the MWC catalog (Merrill and Burwell 1943), then we will find, in addition to HD 183143, only three supergiants of the luminosity class Ia in the range of spectral types B5–B8 in these catalogs: HD 34085, HD 166937, and HD 199478. They all show emissions only in the Hα line; these emissions are much weaker than those in HD 183143 (Andrews 1968). According to the existing relationship between the intensity of the Hα emission and the absolute magnitude for B supergiants (Andrews 1968; Rosendhal 1973), HD 183143 is brighter than the above stars by a whole magnitude. This alone makes it possible to classify it as a hypergiant (luminosity class Ia-0). Moreover, the spectrum of HD 183143 also exhibits emission in the Hβ line; the β index corresponds to $M_v < -8\overset{m}{.}0$, i.e., again to the luminosity of a hypergiant (Lindemann and Hauck 1973; Neckel and Klare 1976).

An enhanced level of photometric and spectral variability, a natural result of enhanced luminosity, has been noted for HD 183143. According to HIPPARCOS photometry, the amplitude of the brightness variations in HD 183143 is twice the average amplitude for B supergiants of the luminosity class Ia (Adelman *et al.* 2000). Long-term moderate-dispersion spectroscopy of HD 183143 has revealed variations of its Hβ profile, from absorption to emission-flooded, as well as variability of the profiles of some of the absorptions (Copeland and Heard 1963).

Unfortunately, the luminosity of HD 183143 is difficult to estimate from its trigonometric parallax or from the star's membership in a cluster (association) because of its large distance and its position in the Galaxy.

According to the HIPPARCOS catalog (ESA 1997), the parallax of HD 183143 is $2.7 \pm 0.8 \times 10^{-3}$ arcsec. However, if the star is the corresponding 370 pc away, then, given interstellar extinction, it falls into the luminosity class Ib or even II ($M_v = -5^m$)! Such a low luminosity is incompatible with the

*E-mail: echen@sao.ru

Log of spectra and heliocentric radial velocities

Date	R	$\Delta\lambda$, Å	V_r, km s^{-1}		
			$r \to 1$	He I 5876 Å	Hα
May 5, 1993	64 000	5650–6870	15	20	−45, 25
May 14, 1997	40 000	4100–8900	13	20	−10
June 11, 1997	40 000	4100–8900	13	18	−70; −25, 50
August 30, 1997	45 000	4100–10 000	18	28	−120, −25
June 5, 1999	25 000	5160–6720	10	17	−47
June 7, 2001	15 000	4550–7840	9	14	−55, 75
July 29, 2002	70 000	4560–5980	20	11	
September 24, 2002	64 000	5450–6700	11	20	−21

peculiarities of the star's spectrum described below; moreover, it would certainly have been noticed by the creators of the MK system. However, the HIPPARCOS data are not accurate enough for stars farther than 0.5–0.6 kpc. This can be seen from the survey of nearby associations by de Zeeuw *et al.* (1999), but is particularly clearly demonstrated using supergiants of the Perseus arm: their distance of at least 2 kpc is confirmed by the splitting of interstellar lines by 40 km s^{-1} (see the classic paper by Munch 1957). Let us compare, for example, HD 14143 (B2 Ia) and HD 14331 (B0 III), on the one hand, with HD 13841 (B2 Ib) and HD 13866 (B2 Ib), on the other hand. They all belong to the Per OB1 association, which is 2.3 kpc away (Humphreys 1978), but the ESA (1997) catalog gives parallaxes of $0.69 \pm 0.78 \times 10^{-3}$ and $0.02 \pm 1.03 \times 10^{-3}$ arcsec for the first pair of stars and $1.83 \pm 0.92 \times 10^{-3}$ and $2.92 \pm 0.83 \times 10^{-3}$ arcsec for the second pair, respectively. In this case, the last supergiant turns out to be a subdwarf! The parallaxes of the two white hypergiants in the Galaxy's second quadrant, HD 168607 and HD 168625, which are 2 kpc away, were also overestimated in ESA (1997): $2.0 \pm 1.2 \times 10^{-3}$ and $2.4 \pm 1.2 \times 10^{-3}$ arcsec.

HD 183143 is located between the local Orion–Cygnus arm and the Carina–Sagittarius arm (its Galactic coordinates are $l = 53\overset{\circ}{.}3$ and $b = 0\overset{\circ}{.}6$), and it cannot be attributed to any particular group: there are no associations within $30^\circ < l < 59^\circ$ in the Humphreys catalog (1978).

However, the distance to HD 183143 can be judged from the radial velocities of the star itself and the interstellar clouds on its line of sight as well as from the relation between the distance and interstellar extinction.

Below, we provide spectroscopic evidence that allows us to classify HD 183143 as a white hypergiant.

SPECTROSCOPIC DATA AND ITS REDUCTION

We used eight spectra of HD 183143, all of which were taken with high-resolution CCD echelle spectrographs. The dates on which they were obtained, the spectral resolutions, and the covered spectral ranges are given in the first three columns of the table. We used the PFES spectrograph at the prime focus of the 6-m BTA telescope at the Special Astrophysical Observatory (Panchuk *et al.* 1998) on June 7, 2001, the LYNX spectrograph at the Nasmyth focus of the same telescope (Panchuk *et al.* 1999) on June 5, 1999, and the NES spectrograph, its replacement (Panchuk *et al.* 2002), on July 29, 2002. The spectrographs at the coudè foci of the 1-m Special Astrophysical Observatory telescope (Musaev 1996) and the 2-m Mt. Terskol Observatory telescope (Musaev *et al.* 1999) were used in 1997: the first on May 14 and June 11 and the second on August 30, 1997. Finally, the spectra of May 5, 1993, and September 24, 2002, were taken at the McDonald Observatory using a spectrograph at the Cassegrain focus of the 2.1-m telescope (McCarthy *et al.* 1993).

After the extraction of one-dimensional spectra from two-dimensional images, the reduction of the spectra, which included the continuum placement, the construction of dispersion curves (from the spectra of a hollow-cathode Th–Ar lamp or radial-velocity standard stars), spectrophotometric and position measurements, was performed using the DECH20 software package (Galazutdinov 1992). In particular, this package, allows the positions

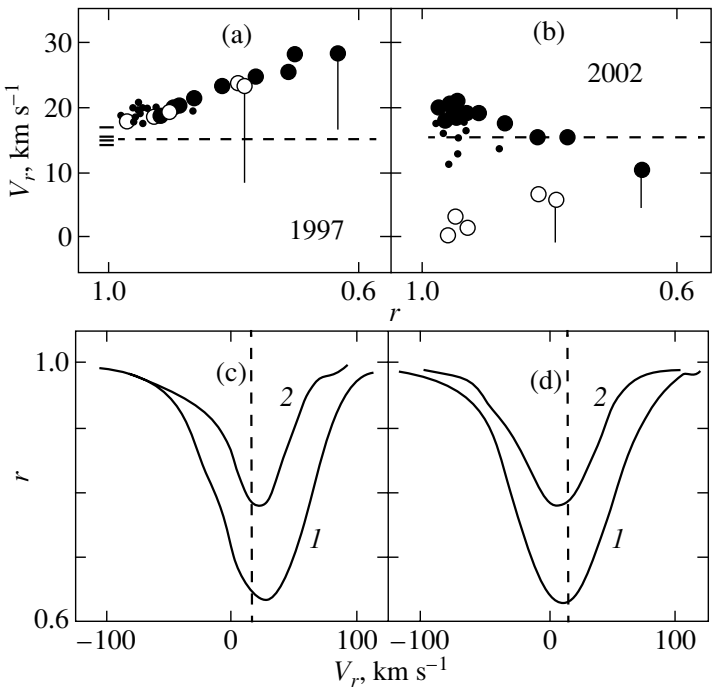

Fig. 1. Relations between the heliocentric radial velocity V_r for the line core and its central residual intensity r (a, b) and the corresponding profiles of He I 5875 Å (*1*) and Fe II 5169 Å (*2*) in the spectra of August 30, 1997 (a, c) and July 29, 2002 (b, d). Each symbol corresponds to an individual line: the filled circles are He I, C II, N II, Al III absorptions; the open circles are Fe II lines; the dots are S II lines; and the horizontal bars are Fe II emissions in the 1997 spectrum. The vertical bars indicate the direction and magnitude of the shifts in the wings relative to the cores. The dashed straight lines indicate the star's center-of-mass velocity.

of individual features in lines to be determined by matching the direct and mirror profile images. The instrumental shifts between the comparison spectra and the spectra of the object being studied were removed using the telluric O_2 and H_2O lines. An estimate of the residual systematic errors, which is of relevant interest in comparing the data obtained with different instruments over nine years, was also made using interstellar Na I lines and narrow DIBs. For the lowest-resolution spectrum taken with the PFES suspension spectrograph, the disregarded shift does not exceed 2 km s^{-1}, and the possible shifts of the remaining spectra are within 1 km s^{-1}. The system of laboratory (for close blends, effective) wavelengths used in measuring the radial velocities is the same as that in the atlas by Chentsov *et al.* (2003).

SPECTROSCOPIC PECULIARITIES AND SPECTRAL VARIABILITY OF HD 183143

The spectrum of HD 183143 in the range 4800–6700 Å is presented in graphical and tabulated forms in the atlas by Chentsov *et al.* (2003); it was obtained by averaging two of the eight spectra used in this paper. The radial velocities measured from individual lines in the spectrum of HD 183143 and the profile shapes of the strongest of them vary with the line intensity and time. The pattern of the former and the latter variations is illustrated by the last three columns of the table and Figs. 1 and 2.

In this paper, we use only the heliocentric radial velocities V_r. Their values, which are given in the table and shown in Figs. 1a and 1b, were measured from the cores of absorptions or the absorption components of Hα. By this we mean the bottom parts of the profiles, where the intensity gradient is still fairly high. For example, for the He I 5876 Å line (Figs. 1c and 1d), they are limited to the range of residual intensities $0.65 < r < 0.7$.

Figures 1a and 1b show sample $V_r(r)$ relations. The filled circles, which represent the weak C II, N II, Al III lines and the deeper He I lines, form distinct chains. These chains are horizontal for main sequence stars and even for Ib supergiants; they acquire a slope for higher-luminosity supergiants (Chentsov 2000). The V_r values in the fourth column of the table were obtained by extrapolating the left ends of the chains to $r = 1.0$, i.e., to the continuum level. The fifth column gives the V_r values for the deepest absorption in the He I 5876 Å line (the circles at the right ends of the chains in Figs. 1a and 1b).

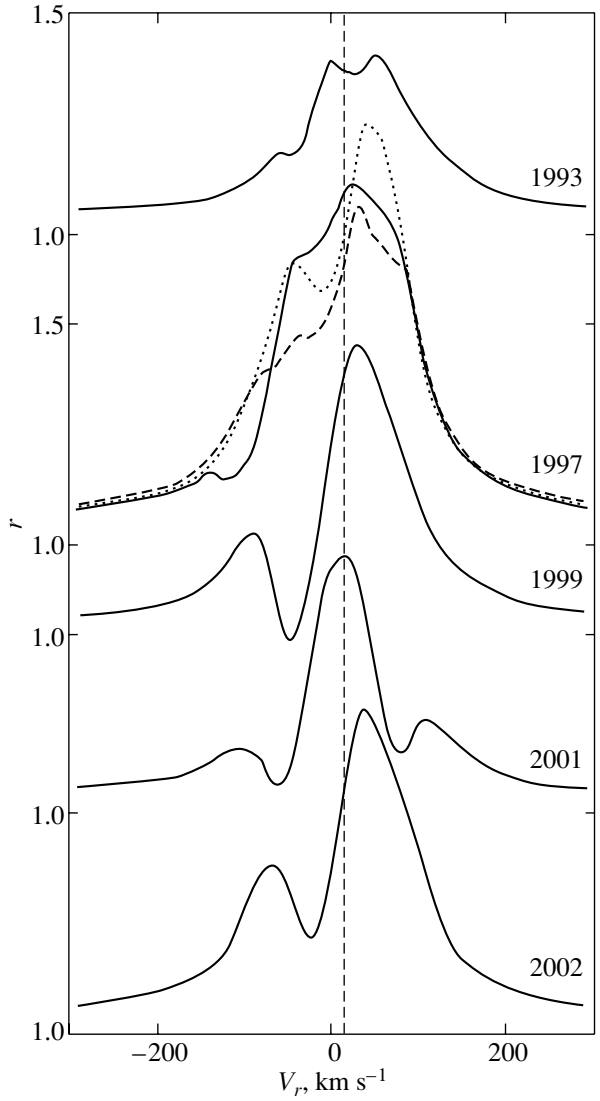

Fig. 2. Hα profiles in the spectra of HD 183143 taken, from top to bottom, on May 5, 1993, May 14, 1997 (dotted line), June 11, 1997 (dashed line), August 30, 1997 (solid line), June 5, 1999, June 7, 2001, and September 24, 2002. The vertical straight line corresponds to V_{sys}.

In the spectrum taken on August 30, 1997, the FeII and SII absorptions (the open circles and the dots, respectively) also fit well into the chain outlined by these lines; the scatter of symbols in Fig. 1a is mainly attributable to measurement errors. The deeper the absorption, the higher the velocity derived from it: the right end of the chain is higher than its left end. Such a slope of the $V_r(r)$ relation is encountered in seven of the eight cases; the chain slope is the opposite only in the spectrum of July 29, 2002 (Fig. 1b).

The center-of-mass velocity of a star (also called the systemic velocity V_{sys}) is of great importance in analyzing the atmosphere kinematics and in estimating its distance. For HD 183143, it can be found from the near-infrared Fe II emissions (7496 Å, 7513 Å, and others; the horizontal bars in Fig. 1a) and from the parts of the Hα profile undistorted by absorption components (see Fig. 2). The value found in this way, $V_{sys} = 15 \pm 2$ km s^{-1}, is indicated by the dashed straight lines in Figs. 1 and 2.

The V_r values for the weakest absorptions, which carry information about the deepest observable atmospheric layers, deviate from V_{sys} toward both lower and higher values, possibly because of the pulsations experienced by these layers. The variations of the velocity with time for these lines are smaller than those for the strongest lines formed in the upper atmosphere and at the base of the wind. The mean velocity from the fourth column of the table (14 km s^{-1}) is equal to V_{sys}, within the error limits.

The positive shifts of strong lines relative to weak lines are indicative of the compression of the atmosphere, but they can also result from the existence of a system of upflows and downflows in it. Recall that we are dealing with the cores of strong absorptions, while the line asymmetry provides evidence for expansion: the upper parts of the profiles are blueshifted relative to their lower parts. This can be immediately seen from Figs. 1c and 1d and is indicated by the vertical line segments in Figs. 1a and 1b. The velocity derived from the upper part of the FeII 5169 Å profile in the spectrum of August 30, 1997 is several km s^{-1} lower than V_{sys}; the velocity measured from the extended blue wing is lower by almost 100 km s^{-1}. The atmospheric expansion of HD 183143 shows up even more clearly in the spectrum of July 29, 2002 (Figs. 1b, 1d): not only the wings, but also the cores of strong absorptions exhibit negative shifts; even the weak S II lines, not to mention the Fe II lines, formed above the C II and N II lines are blueshifted relative to them. It should be noted that late-B Ia supergiants also show an increase of the velocity with line intensity, but their characteristic type of asymmetry is opposite to that observed for HD 183143: the wings are redshifted relative to the cores (Chentsov 2000). The described combination of differential line shifts and their profile shapes is encountered only in hypergiants.

The anomalous intensity of the emissions in the first terms of the Balmer series for HD 183143 has already been noted in the Introduction. Figure 2 shows the features of the Hα profile and the detected profile variations; both make HD 183143 similar to the B5–B6 hypergiants Cyg OB2-12 and HD 168625 (Klochkova *et al.* 2003). Apart from the high emission intensity, all three stars are characterized by broad Thomson wings, comparatively low wind velocities, and the frequent occurrence of unshifted or even redshifted components, in addition to the blueshifted components. The change of the

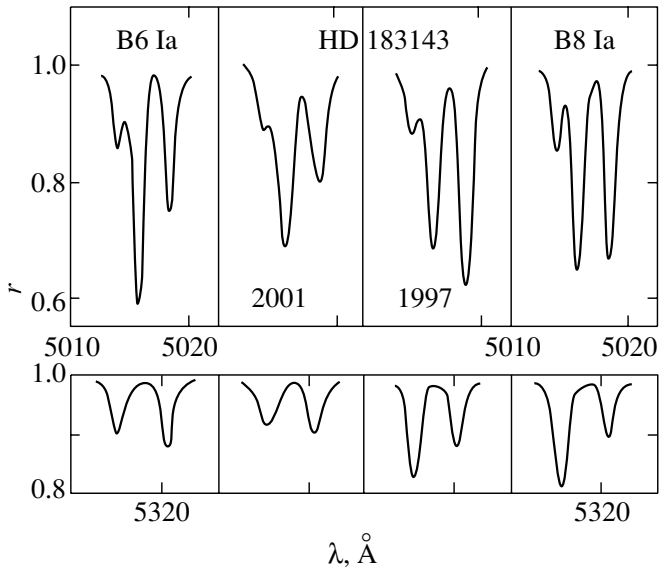

Fig. 3. Pairs of neighboring lines, He I 5015 / Fe II 5018 (top) and Fe II 5316 / S II 5320 (bottom), in the spectra of HD 183143 and the comparison stars HD 15497 (B6 Ia), HD 183143 (June 7, 2001), HD 183143 (May 14, 1997), and β Ori (B8 Ia).

direct P Cyg profile to the inverse profile, as well as the coinciding of their features in the same line, has recorded in some of the LBVs at the phases of maximum visual brightness, i.e., when their spectra become similar to those of white hypergiants (Wolf and Stahl 1990; Stahl *et al*. 2003).

The summer of 1997 is the only season when three Hα-containing spectra were taken. Their profiles are superimposed on each other without a vertical shift in Fig. 2. Here, we can see the sequential phases of the formation of absorption components near the top of the profile and their gradual recession from it, slipping down along the blue wing: within three and a half months, V_r decreased from -10 to -120 km s^{-1}. This effect, which was originally discovered at P Cyg, is also known only for a few blue and white hypergiants.

The depths and equivalent widths of the absorptions in the spectrum of HD 183143 vary with time, as do their positions, and this variation is anomalously large for a B supergiant. The quantitative spectral classification based on our spectra has revealed variations of the spectral type within B6–B8. They are seen from Fig. 3, for which two pairs of neighboring lines were selected: He I 5015 Å with Fe II 5018 Å and Fe II 5316 Å with S II 5320 Å. The intensity ratios of the lines in these pairs are good classification criteria: in the spectra of supergiants, the S II absorptions are deepest near the B6 subtype, the He I absorptions become weaker toward the later subtypes, while the Fe II absorptions become stronger. However, Fig. 3 also shows that the spectral variability of HD 183143 can hardly be reduced only to a response to a change in effective temperature. Whereas for the comparison stars (whose spectra are shown in Fig. 3), its decrease is accompanied both by a strengthening of the Fe II lines and by a weakening of the He I and S II lines, the latter remain almost constant for HD 183143. Only the Fe II lines exhibit significant variations; they may be affected by a nonstationary stellar wind.

Clearly, almost all of the above effects require detailed study; this demands more frequent, preferably weekly observations. HD 183143 is a very promising object for spectroscopic monitoring.

LUMINOSITY AND DISTANCE

The set of spectroscopic peculiarities described above, which makes HD 183143 similar to a few hypergiants rather than to numerous B supergiants (the large amplitudes of the radial-velocity and spectral-type variations, the large differential line shifts, the extended blue wings of strong absorptions, the strong Hα emission, and the low-velocity wind Hα absorptions, including the "moving" dips in its blue wing) suggests that the luminosity of HD 183143 is very high, exceeding the luminosity of a B7 Ia supergiant.

As was noted in the Introduction, the intensity of the emissions in the first Balmer lines corresponds to $M_v < -8^m$, i.e., to the luminosity class Ia-0 (Humphreys and McElroy 1984). M_v can also be estimated from the luminosity dependences of the amplitude of the temporal V_r variations and the mutual line shifts for supergiants and hypergiants (Chentsov 1978). Substituting our values, 11 and 20 km s^{-1}, respectively, in these dependences, we again obtain $M_v < -8^m$. Finally, the luminosity

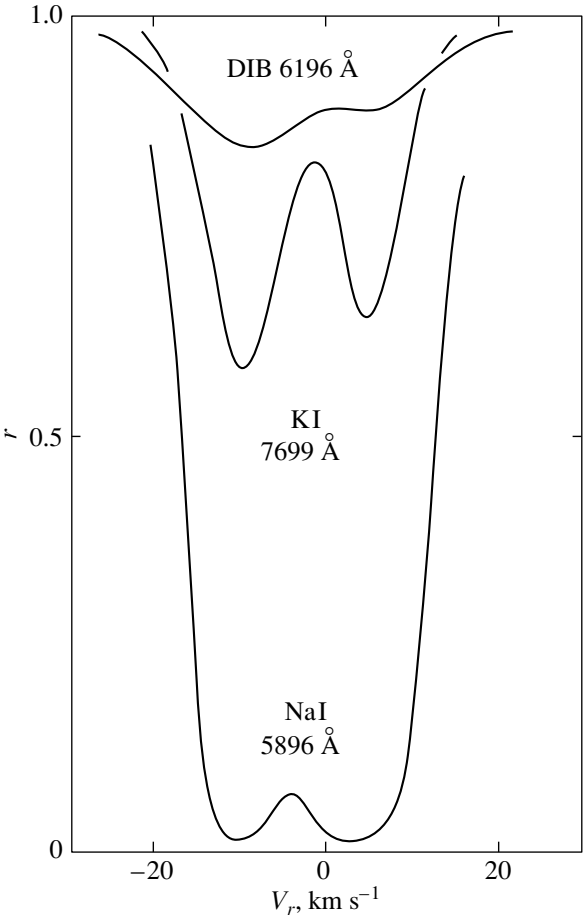

Fig. 4. Profiles of the interstellar Na I and K I lines and the 6196 Å band in the spectrum of HD 183143 at spectral resolutions of no lower than 60 000.

level of a hypergiant is also evidenced by the large equivalent width of the OI 7773 Å triplet: 1.75 Å as estimated by Faraggiana *et al.* (1988) and 1.85 Å as estimated from our data.

The luminosity determinations from the dependence of interstellar extinction A_v on distance d and from the kinematic distance are also consistent with these estimates.

The first method yields only a lower limit for the distance. In the survey by Neckel and Klare (1980), the Milky Way field containing HD 183143 is very large (about 40 square degrees), and the extinction in it is nonuniform. However, a refinement of the $A_v(d)$ plot using stars in a smaller (8 square degrees) field near HD 183143 did not change the estimate. Based on the color excess $E(B-V) = 1\overset{m}{.}28$ (Herbig 1993) and the corresponding extinction $A_v = 4\overset{m}{.}0$, we obtained $d > 1.0$ kpc.

The differences in the spectral resolutions are not very significant when comparing the profiles of fairly broad spectral lines obtained on different dates, but they appreciably affect the profiles of interstellar lines. The mean kinematic distance to interstellar gas clouds on the line of sight to HD 183143 can also be estimated by using moderate-resolution spectra, but the contribution from the farthest (and most interesting to us) clouds will not be taken into account in this case. The Na I and K I lines in the moderate-resolution spectra taken on June 5, 1999, and June 7, 2001, are not resolved into components and yield $V_r = -2$ km s^{-1}. However, we see from Fig. 4 that the profiles of not only these lines but also the narrow DIBs obtained with a sufficiently high resolution are split. However, the separation between the components is much smaller than that in the Galaxy's second quadrant, only about 13 km s^{-1}. The velocity toward HD 183143 increases with distance, at least up to 2 kpc (Brand and Blitz 1993); whereas the V_r value derived from the profile as a whole is also -2 km s^{-1}, yielding $d = 1.0$ kpc, the position of the red component corresponds to $d = 1.5$ kpc. Finally, the velocity of the star itself (15 km s^{-1}) corresponds to its distance close to 2.0 kpc. Of course, an individual star can have a peculiar velocity component along the line of sight. In our case, an allowance for the V_r overestimation by 10 km s^{-1} decreases the distance to 1.5 kpc. According to the above estimate, a distant clump of interstellar matter lies at this distance from us (but certainly closer than the star).

Given the interstellar extinction $A_v = 4\overset{m}{.}0$, $M_v = -7\overset{m}{.}2$, $-8\overset{m}{.}0$, and $-8\overset{m}{.}7$ correspond to $d = 1.0$, 1.5, and 2.0 kpc for HD 183143, respectively. Thus, HD 183143 must have the luminosity of a hypergiant even at a distance of 1.5 kpc.

CONCLUSIONS

The spectroscopic history of HD 183143 in the last decades has been dramatic and instructive. Many investigators have devoted their attention only to the interstellar matter on the line of sight to the star. At the same time, the star itself as a unique object with an extremely high luminosity and pronounced instability has been ignored.

Spectroscopy provides various and quite convincing bits of evidence that HD 183143 may be considered yet another Galactic white hypergiant. The star's luminosity exceeds the luminosity of ordinary Ia supergiants by a whole magnitude. This follows from the various spectroscopic instability manifestations pertaining both to the stellar atmosphere and to the stellar wind. The pattern and degree of these manifestations allow us to reliably distinguish a supergiant from a hypergiant and to attribute HD 183143 to the latter. This is also confirmed by the distance to the

star estimated using the only method currently available, i.e., from the differential rotation of the Galaxy.

Note also that HD 183143 is one of the visually brightest stars among the white hypergiants of the northern sky; it is accessible to high-resolution spectroscopy even with moderate-size telescopes. Thus, it is hoped that, in the near future, it will become a very helpful and actively used object in studies of the evolution of massive stars and their mass-loss mechanisms.

ACKNOWLEDGMENTS

I am grateful to V.E. Panchuk, G.A. Galazutdinov, F.A. Musaev, A.S. Miroshnichenko, J. Krelowski for providing the spectroscopic data and to N.S. Tavolzhanskaya for preparing the manuscript for publication. This study was supported by the Russian Foundation for Basic Research (project no. 02-02-16085a), the Astronomy Program, and the Extended Objects in the Universe basic research program of the Department of Physical Sciences of the Russian Academy of Sciences (the Spectroscopy of the Extended Envelopes of Stars at Late Evolutionary Phases subprogram).

REFERENCES

1. S. J. Adelman, K. Yuce, and S. Engin, Inf. Bull. Var. Stars, No. 4946 (2000).
2. P. J. Andrews, Mem. R. Astron. Soc. **72**, 35 (1968).
3. J. Brand and L. Blitz, Astron. Astrophys. **275**, 67 (1993).
4. E. L. Chentsov, Soobshch. SAO **21** (1978).
5. E. Chentsov, *IAU Coll. 169: Variable and Non-Spherical Stellar Winds in Luminous Hot Stars,* Ed. by B. Wolf, O. Stahl, and A. W. Fullerton (Springer-Verlag, Berlin, 2000), p. 206.
6. E. L. Chentsov, S. V. Ermakov, V. G. Klochkova, *et al.*, Astron. Astrophys. **397**, 1035 (2003).
7. J. A. Copeland and J. F. Heard, Publ. David Dunlap Obs. **2**, 317 (1963).
8. R. Faraggiana, M. Gerbaldi, C. van't Veer, and M. Floquet, Astron. Astrophys. **201**, 259 (1988).
9. G. A. Galazutdinov, Preprint No. 92, SAO (Special Astrophysical Observatory, Nizhniĭ Arkhyz, 1992).
10. G. A. Galazutdinov, F. A. Musaev, J. Krelowski, and G. A. H. Walker, Publ. Astron. Soc. Pac. **112**, 648 (2000).
11. G. H. Herbig, Astrophys. J. **196**, 129 (1975).
12. G. H. Herbig, Astrophys. J. **407**, 142 (1993).
13. G. H. Herbig, Astron. Astrophys. Rev. **33**, 19 (1995).
14. R. M. Humphreys, Astrophys. J., Suppl. Ser. **38**, 309 (1978).
15. R. M. Humphreys and D. B. McElroy, Astrophys. J. **284**, 565 (1984).
16. P. Jenniskens and F. X. Desert, Astron. Astrophys., Suppl. Ser. **106**, 39 (1994).
17. H. Johnson and W. W. Morgan, Astrophys. J. **117**, 313 (1953).
18. ESA, *The Hipparcos and Tycho Catalogues,* SP-1200 (1997).
19. V. G. Klochkova, E. L. Chentsov, N. S. Tavolzhanskaya, and G. A. Proskurova, Preprint No. 183, SAO (Special Astrophysical Observatory, Nizhniĭ Arkhyz, 2003).
20. E. Lindemann and B. Hauck, Astron. Astrophys., Suppl. Ser. **11**, 119 (1973).
21. J. K. McCarthy, A. Brendan, A. Sandiford, *et al.*, Publ. Astron. Soc. Pac. **105**, 881 (1993).
22. P. W. Merrill and C. G. Burwell, Astrophys. J. **78**, 87 (1933).
23. P. W. Merrill and C. G. Burwell, Astrophys. J. **98**, 153 (1943).
24. F. A. Musaev, Pis'ma Astron. Zh. **22**, 795 (1996) [Astron. Lett. **22**, 715 (1996)].
25. F. A. Musaev, G. A. Galazutdinov, A. V. Sergeev, *et al.*, Kinemat. Fiz. Neb. Tel **15**, 3 (1999).
26. G. Munch, Astrophys. J. **125**, 42 (1957).
27. T. Neckel and G. Klare, Astron. Astrophys. **52**, 77 (1976).
28. T. Neckel and G. Klare, Astron. Astrophys., Suppl. Ser. **42**, 251 (1980).
29. V. E. Panchuk, I. D. Najdenov, V. G. Klochkova, *et al.*, Bull. SAO **44**, 127 (1998).
30. V. T. Panchyuk, V. G. Klochkova, I. D. Naidenov, *et al.,* Preprint No. 139, SAO (Special Astrophysical Observatory, Nizhniĭ Arkhyz, 1999).
31. V. T. Panchyuk, N. E. Piskunov, V. G. Klochkova, *et al.,* Preprint No. 169, SAO (Special Astrophysical Observatory, Nizhnii Arkhyz, 2002).
32. J. D. Rosendhal, Astrophys. J. **186**, 909 (1973).
33. O. Stahl, T. Gaeng, C. Sterken, *et al.*, Astron. Astrophys. **400**, 279 (2003).
34. S. O. Tuairisg, J. Cami, B. H. Foing, *et al.*, Astron. Astrophys., Suppl. Ser. **142**, 225 (2000).
35. B. Wolf and O. Stahl, Astron. Astrophys. **235**, 340 (1990).
36. P. T. de Zeeuw, R. Hoogerwere, and J. H. J. de Bruijne, Astron. J. **117**, 354 (1999).

Translated by N. Samus'

Astronomy Letters, Vol. 30, No. 5, 2004, pp. 332–342. Translated from Pis'ma v Astronomicheskiĭ Zhurnal, Vol. 30, No. 5, 2004, pp. 376–386.

Line Variability in the Spectrum of Supergiant α Cam

A. Kh. Rzayev[1,2*] and V. E. Panchuk[1]

[1] *Special Astrophysical Observatory, Russian Academy of Sciences, Nizhniĭ Arkhyz, 357147 Karachai-Cherkessian Republic, Russia*

[2] *Shamakha Astrophysical Observatory, National Academy of Sciences of Azerbaijan, village of Yu. Mamedaliev, Azerbaijan*

Received June 23, 2003

Abstract—CCD spectra taken with the PFES and CEGS echelle spectrographs attached to the 6-m Special Astrophysical Observatory (Russian Academy of Sciences) telescope and the 2-m Shamakha Astrophysical Observatory (National Academy of Sciences of Azerbaijan) telescope, respectively, were used to study the line-profile variations in the spectrum of the hot supergiant α Cam. No fast ($\leq$1.5 h) line-profile and radial-velocity variations were found. Some of the systematic effects that cause spurious variability are considered. The Hα-profile variability appears symmetric relative to the radial velocity of the star's center of mass and is attributable to variable blueshifted and redshifted emission and/or absorption components superimposed on a variable photospheric profile. The Hα line shows evidence of a large-scale mass ejection from the stellar surface, which is also traceable in other spectral lines. The He II 4686 line exhibits an inverse P Cyg profile, while the red wing of the He I 5876 line shows weak and variable emission. The fast (on characteristic time scales of shorter than an hour) variability of the He II 4686 profile that was previously revealed by our observations (Kholtygin *et al.* 2000) is called into question. A comparison of the observational data on the variability of ultraviolet and optical line profiles for the supergiant αCam suggests that nonradial motions are mainly responsible for the radial-velocity and line-profile variability.

Key words: *stars—variable and peculiar; supergiant stars.*

INTRODUCTION

Short-term (on the order of a day) variability of the envelopes of some of the OB stars was first revealed by extraatmospheric studies of their UV spectra (see, e.g., Prinja and Howarth 1986). The introduction of highly efficient optical detectors, the advent of telescopes specially designed for spectroscopic monitoring, and the ensuing large-scale observations of hot OB stars (Fullerton 1991; Kaper *et al.* 1996, 1997, 1999; Wolf *et al.* 1999; Rauw *et al.* 2003) have shown that line-profile variability on characteristic time scales from several hours to several days is a common property of these objects.

Evidence of a nonstationary and inhomogeneous stellar wind shows up both in line-profile variability (a change in the slope of the blue wing or even a shift in the blue part of the line core) and in the appearance of discrete absorption components (Underhill 1975), their development and migration away from the core to the blue part of the line (Chentsov 1995).

The current mass-loss models (Cherepashchuk 1990; Lepine *et al.* 1996; Kostenko and Kholtygin 1998; Fullerton 1999; Kaper *et al.* 1999) are also critical, in particular, to the characteristic variability time scale in the spectra of OB stars. The choice between models and their further improvement are related to an increase in the amount of observational data for specific objects and to the extension of detailed spectroscopic studies of hot stars to other spectral subtypes and luminosity classes. It is also important to estimate the minimum characteristic time scale of the spectroscopic variability. Whereas special-purpose small-diameter spectroscopic telescopes with optical-fiber spectrographs are effectively used to study the variability on time scales of longer than a day (see, e.g., Mandel 1988), it is desirable to use larger telescopes to search for fast variability. The multipurpose 6-m BTA telescope is equipped with instrumentation (Panchuk *et al.* 2002) that, in particular, allows the fast line-profile variability to be investigated over the range of spectral resolutions $R = 4000-75\,000$.

The star αCam is a typical O9.5 Iaf supergiant with a high rotational velocity, $v \sin i \approx 85$ km s^{-1}

* E-mail: abid@sao.ru

(Conti and Ebbets 1977). This runaway star (Blaaw 1961; Stone 1979) also arouses considerable interest because it may be a close binary with a degenerate secondary component. Having analyzed its radial-velocity variations, Lee (1913), Bohannan and Garmany (1978), and Zeĭnalov and Musaev (1986) each suggested different periods (≈7, 47, and 4 days, respectively). However, the hypothesis about periodic radial-velocity variations has not been confirmed (Stone 1982; Musaev and Snezhko 1988). The radial-velocity variability is now interpreted as a result of the object's physical variability that distorts the line profiles.

Numerous observations performed in several stages with spectral resolutions of $R \sim 16\,000$ and 32 000 and a signal-to-noise ratio of no lower than $S/N = 200$ have revealed the variability of the Hα and He I 6678 line profiles (Ebbets 1980, 1982). The minimum time scale on which the Hα profile was suspected to be variable is 3 h, while variability on the 6-h time scale was recorded with confidence. Significant profile variations were found only a day later. In the He I 6678 line, (mainly) the slope of the blue wing varied.

The UV spectra of α Cam taken in 1978 over 72 h (Lamers *et al.* 1988) revealed variability in the resonance lines on a characteristic time scale of about 7 h. This variability was explained in terms of stellar-wind inhomogeneities. Based on the UV spectra taken in 1991 over 5 days, Kaper *et al.* (1996) found no significant variations in the line profiles. Significant Hα-profile variability was found in the optical ($R =$ 22 000) spectra that accompanied the UV observations (Kaper *et al.* 1996). The emission and absorption components of the P Cyg Hα profile exhibited significant variations over 4 days (Kaper *et al.* 1997), but the variations on a time scale of 3–6 h discovered by Ebbets (1980) have never been confirmed.

Photographic spectra are also suitable for studying the variability on a time scale of a day or more. Based on the spectrograms taken with the coudè spectrograph of the 2-m Shamakha Astrophysical Observatory telescope over several years, Zeĭnalov *et al.* (1986) found variability of the Hα and He I 5876 lines. Weak emission was detected in the red wing of the He I 5876 line.

Fullerton *et al.* (1996), who studied 30 bright early-type O stars, including α Cam, showed that variability of the profiles and radial velocities of the C IV λ5801, 5812 Å, and He I 5876 lines on a time scale from several hours to several days was a common property for most of the O stars.

Based on 65 CCD spectra taken over a year with a resolution of $R = 15\,000$ (10 of them were obtained with $R = 22\,000$), Markova (2002) investigated the variations in the Hα and He I 6678 profiles. No fast Hα-profile variations were found. It was noted that the Hα profiles were similar in shape and intensity to the profiles obtained by Ebbets (1980) and Kaper *et al.* (1997). Variations were observed in the central parts of the Hα and He I 6678 profiles over velocity ranges of $\pm$300 and $\pm$200 km s^{-1}, respectively, and were symmetric about the line center. An analysis of the variability of these two lines provided clear evidence for continuous wind activity. This evidence implied a deviation from spherical symmetry and the presence of large-scale short-term wind density perturbations that could be modulated by rotation. The variability patterns and periods differ for different observing seasons (summer and winter) and require an explanation that includes various forms and scales of wind perturbation.

Our goal here is to study the fast line-profile variability in the spectrum of α Cam using CCD spectra taken with the 6-m Special Astrophysical Observatory (SAO) telescope. The rationale and scientific aspects of this study were clearly explained by Kholtygin *et al.* (2003). CCD spectra taken with the 2-m Shamakha Astrophysical Observatory (ShAO) at the coudè focus have also been used for this purpose.

OBSERVATIONS AND DATA REDUCTION

As part of our program of searching for fast variability in the spectra of hot stars (an application by A.F. Kholtygin), one of us (V.E. Panchuk) carried out observations with the 6-m SAO telescope in February 1997. In particular, 20 spectra of α Cam were obtained with the prime-focus echelle spectrograph (PFES) equipped with a 1160 × 1040-pixel CCD array (Panchuk *et al.* 1998) over 1.5 h. A comparison spectrum was taken only at the beginning and at the end of the series of spectral exposures for the star. The spectral resolution was $R = 15\,000$, and the interval between neighboring exposures was 2.5–3 min; each echelle image was read off for 100 s. The simultaneously recorded spectral range was 4330–8300 Å. The signal-to-noise ratio was $S/N \geq 150$ and $S/N \geq 350$ for the blue (near H γ) and red (near Hα) spectral regions, respectively. To take into account the influence of the telluric spectrum, we additionally obtained the spectra of a rapidly rotating hot star. These observational data were primarily studied by the applicant; the reduction of one echelle order (the wavelength range 4658–4720 Å) led Kholtygin *et al.* (2000) to conclude that there was fast variability in the spectral intervals from 0.5 to 50 Å. Below, we present the results of our analysis of these observational data that are based on our reduction of the spectra in 2003.

Heliocentric radial velocities of the lines in the spectrum of α Cam

Line or group of lines	V_r, km s^{-1}				
	Feb. 24, 1997	Oct. 15, 1999	Oct. 16, 1999	Aug. 1, 2000	Aug. 28, 2000
	I^{*a}	I^{*a}_{15}	I^{*a}_{16}	I^{*a}_{01}	I^{*a}_{28}
Hα[b]	90.0 ± 1.2	150.0 ± 0.7	133.0 ± 1.0	96.5 ± 1.5	111.0 ± 1.0
Hα[c]	–	-168.0 ± 2.0	-170.0 ± 1.5	-170.5 ± 2.0	-184.0 ± 2.5
				-95.5 ± 0.8	
Hβ	-31.9 ± 2.0	-27.0 ± 1.2	-18.0 ± 0.9	-27.0 ± 1.0	-19.0 ± 2.0
Hγ	-39.2 ± 3.5	-24.0 ± 1.5	-23.8 ± 1.2	-37.0 ± 1.5	-30.0 ± 1.8
He I 6678	-5.0 ± 0.7	5.0 ± 1.0	5.4 ± 0.9	6.0 ± 0.7	7.7 ± 0.5
He I 5876[b]	–	170.0 ± 2.0	170.6 ± 2.6	170.3 ± 0.5	169.1 ± 1.8
He I 5876[c]	-26.1 ± 1.2	-7.4 ± 0.9	-6.5 ± 0.8	-9.3 ± 0.9	-1.0 ± 1.0
He I	13.0 ± 2.0	11.6 ± 0.5	13.3 ± 1.0	13.3 ± 2.0	20.0 ± 2.5
He II 4686[b]	-100.6 ± 3.0	–	–	–	–
He II 4686[c]	31.0 ± 2.0	–	–	–	–
He II	18.0 ± 1.5	10.0 ± 1.5	28.0 ± 1.0	30.0 ± 2.0	22.0 ± 1.5
C III 5695[b]	12.9 ± 1.1	11.2 ± 0.9	15.0 ± 0.9	14.3 ± 1.1	14.4 ± 0.7
C III	21.3 ± 2.0	14.0 ± 0.8	20.0 ± 2.0	26.0 ± 2.0	17.0 ± 2.1
C IV	22.2 ± 0.9	20.0 ± 1.5	29.0 ± 1.0	25.0 ± 1.0	13.0 ± 1.0
Interstellar lines	-7.4 ± 0.7	–	–	–	–
Interstellar lines	-5.3 ± 2.2	-6.3 ± 2.0	-5.4 ± 1.5	-5.0 ± 2.2	-4.8 ± 2.0

[*a] Introduced to denote the line profiles in the figures.
[b] Emission line.
[c] Absorption line.

To estimate the variability on characteristic time scales shorter than one hour, we used the spectra taken by one of us (A.Kh. Rzayev) with the CEGS echelle spectrograph equipped with a 580×530-pixel CCD array and mounted at the coudè focus of the 2-m ShAO telescope (Musaev 1993). At least two spectra were obtained on each night with a resolution of $R = 36\,000$ (see the table). The exposure time was 10–15 min; the signal-to-noise ratio was S/N ≥ 150 and S/N ≥ 100 for the red and blue spectral regions, respectively.

The reduction of the BTA echelle images (dark-current subtraction, stray-light removal, pixel-to-pixel nonuniformity correction, etc.) was performed using the MIDAS software package. This package was adapted by Klochkova (1994) to the different echelle spectrographs designed in the Laboratory of Stellar Spectroscopy at SAO and modified to eliminate the relative shifts of individual echelle frames (Yushkin 2002). These shifts arise mainly from instabilities of the spectrograph and the optical detector. For PFES, the flexure effects of the suspension spectrograph dominate over the position instability of the detector proper (Panchuk *et al.* 2001). The indi-

vidual echelle spectral orders (vectors) were reduced using the DECH20 software package (Klochkova and Galazutdinov 1991; Galazutdinov 1992).

Peculiarities of the reduction procedure for the coudè echelle spectra taken with the 2-m ShAO telescope and results of our study of the accuracy of photometric and position line measurements can be found in the papers by Rzayev *et al.* (1999a, 1999b). The technique for measuring the radial velocities of spectral lines was described previously (Rzayev 2002). Since most of the stellar lines in the spectrum of α Cam are asymmetric, their radial velocities were measured at different levels of the line profile. When averaged over the entire profile, these determinations correspond to the level at half the line depth. The radial velocities estimated from the interstellar Na I D_1 and D_2 doublet lines and the K I 7699 line are in good agreement. The radial velocities determined from diffuse interstellar bands (DIBs), even from such intense bands as those at λ5780 and 5797 Å, show a noticeable scatter and, in comparison with interstellar lines, yield systematic velocity differences, on average, about 2 km s^{-1} (see the table). This scatter is probably attributable to the new effective DIB wavelengths (Galazutdinov *et al.* 2000) that we used.

We checked the systematic errors of the line radial-velocity measurements by using our measurements of the H_2O and O_2 telluric lines. The rms deviation from the mean determined from 40 telluric lines is -0.2 ± 0.6 and 0.4 ± 0.9 km s^{-1} for the spectra taken with the coudè echelle spectrograph of the 2-m ShAO telescope and the prime-focus echelle spectrograph the 6-m SAO telescope, respectively.

Detecting weak and (or) extended spectral features is related to the continuum placement procedure. The placement of the continuum level was checked by comparing it with the continuum level in the neighboring orders. The initial data for such comparisons was the echelle spectrum of an incandescent lamp.

In general, the reduction of echelle spectra (particularly those obtained with suspension spectrographs) requires a deeper understanding of the spectrum observation and reduction processes with allowance made for the design and operational features of the telescope and the spectrograph. Ignoring this circumstance may lead to erroneous results and hasty conclusions.

RESULTS OF THE OBSERVATIONS

In the visible wavelength range, the He I λ6678, 5875 Å, He II 4686, and Hα line profiles are known to be most sensitive to stellar-wind variations in hot stars. Our measurements, based on all of the 20 PFES spectra obtained over 1.5 h, suggest that (to within the accuracy of the continuum placement) these lines exhibit no fast radial-velocity and profile variations. To study the remaining lines, we selected the 11 spectra with the largest signal-to-noise ratios. In order not to overload the table and the figures, we present the results obtained only from these 11 spectra. We found no fast variations in the coudè spectra taken over 30–40 min either. Therefore, the coudè spectra taken during one night were subsequently averaged. The table and the figures present the results averaged over the coudè spectra for each night.

The lines and groups of lines studied are listed in the table. For the PFES spectra, the group designated as He I includes the λ4387, 4471, 4713, 4921, 5015, 5047, and 7065 Å lines. All of the lines from this group show the same radial velocity. The velocities measured from the He I λ6678 and 5876 Å lines, which differ significantly from the mean radial velocity for the He I group, are presented in the table separately. The He II group includes the λ4541, 4686, and 5411 Å lines. Each of the C III and C IV groups includes two lines, λ4647, 4650 and 5801, 5811 Å, respectively.

The dimensions of the CCD array (580 × 530 pixels) in the coudè spectrograph of the 2-m ShAO telescope are too small to cover the entire spectral range, both in the direction of crossed dispersion and in the length of one order (Rzayev *et al.* 1999a). Therefore, some of the lines measured with PFES lie outside the CCD frame of the coudè spectrograph, and they are marked by a dash in the table.

The PFES profiles of the selected lines obtained over 1.5 h for the 11 spectrograms are shown in Figs. 1a–4a and Fig. 5. Variations no larger than 1.0% of the mean profile level are seen in the Hα profile. In the list of 11 spectra, we specially included two spectra (of the 20 spectra with the smallest S/N ratios taken at the beginning and at the end of our observations) that exhibited the apparent spurious systematic variations at a radial velocity of about -250 km s^{-1} to be considered in the next section. Neither do the variations in the profiles of other lines exceed 1%. Before comparing our results with those of other authors, let us consider the influence of some of the factors (atmospheric dispersion and turbulence, telescope behavior, spectrograph flexure, signal noise, and spectrum reduction peculiarities) on the radial-velocity and equivalent-width determinations and on the above profile variations.

SYSTEMATIC EFFECTS

Let us estimate the effect of atmospheric dispersion using 0.04 arcsec at 100 Å in yellow light for a

zenith distance of 45° as a guide. At the wavelengths at the edges of one echelle order (180 Å in length for Hα), the effective centers of the stellar image can be separated by atmospheric dispersion by no more than 0.07 arcsec. Given the image scale at the prime focus (8 arcsec mm^{-1}) and the wide spectrograph slit (1.43), this value corresponds to the change in the separation between the lines at the edges of the spectral order by 6.3 μm. At a reciprocal linear dispersion of 11 Å mm^{-1} for Hα, the mismatch between the radial velocities determined from these lines is 3 km s^{-1}. For the opposite wings of a line that occupies 3–4% of the length of the echelle order, the effect reduces to 0.1 km s^{-1}. The estimate was made for the limiting case where the directions of the atmospheric dispersion and echelle dispersion vectors coincided. The slit width during the PFES observations was 0.45 arcsec at 2-arcsec seeing, and the mean zenith distance was 33°; the slit was directed along the atmospheric dispersion vector. Thus, the insignificant effect of atmospheric dispersion on the profile shape of a broad line was virtually eliminated.

The diameter of the telescope objective is much larger than the correlation radius of the amplitude fluctuations in a plane perpendicular to the direction of wave propagation; i.e., as a result of atmospheric turbulence, the total luminous flux fluctuates only slightly. The averaging action of the objective of a large telescope eliminates the effect of atmospheric turbulence both on the positions of spectral lines and on the shape of the energy distribution. Our numerical estimates show that this assertion is also valid for the case where the location of the focal plane of the telescope differs from the location of the slit plane.

As any electromechanical construction, the BTA has a spectrum of eigenfrequencies. Even in the absence of telescope motion corrections, quasi-periodic shifts in the centers of the stellar images with an amplitude of 0.3–0.4 arcsec are observed in the frequency range 0.7–0.9 Hz (Balega *et al.* 1990). The problem of holding the center of the stellar image on the spectrograph slit was solved by creating a local corrector (Ivanov *et al.* 2001), but no such correction was applied in the 1997 observations under consideration. The exposure time on PFES was 30–40 s; during this time, the center of the stellar image made about ten oscillations, which, incidentally, further reduced the atmospheric dispersion effect. Apart from the oscillations, there is also a systematic slippage of the average position of the stellar center from the slit, which was eliminated only in 1999 (Shergin 2000). In our observations, we compensated for this slippage by manual correction; this generated oscillations with the dominant harmonics at frequencies 0.8–1.0 and 0.4 Hz for the azimuth and zenith distance axes, respectively. At the minimum correction rate, the amplitude of these oscillations reaches 1 arcsec and the decay time is 25 s; i.e., it is almost equal to the exposure time. Therefore, the position of the telescope was corrected at the beginning of the signal readout from the CCD array, i.e., between the exposures. Let us estimate the effect of oscillations in the position of the stellar disk relative to the slit center on the shifts of spectral lines by assuming that there were 9 and 10 oscillations symmetric about the slit center during the neighboring exposures. Whereas one oscillation shifts the effective center of slit illumination by a third of the slit width, which corresponds to a change in radial velocity by 6.6 km s^{-1}, ten oscillations reduce the effect by at least an order of magnitude. Thus, the fact that the stellar image oscillations are not identical can provide a radial velocity difference between the neighboring exposures of several tenths of km s^{-1}. As in the case of the atmospheric dispersion effect, the effect of oscillations decreases as the seeing deteriorates.

The spectral line shift due to the flexure of the PFES suspension spectrograph is a linear function of the zenith distance Z (Panchuk *et al.* 2001); a change in Z by one degree corresponds to a systematic radial-velocity shift by 0.6 km s^{-1}. The time of our observations of α Cam was chosen in such a way that the change in Z between the centers of the neighboring exposures did not exceed 0°.01, which corresponds to a systematic error of only 0.006 km s^{-1}. The systematic errors due to the instabilities of the detector unit used were studied by Klochkova *et al.* (1999) and Panchuk *et al.* (2001); their value is about 0.05 km s^{-1} for the neighboring exposures of α Cam.

Construction flexures can also affect the filling pattern of the spectrograph optics, which, in principle, distorts the energy distribution along the order. Since the flexures were eliminated almost completely in our observations, this effect is also negligible.

At a high level of the accumulated signal and for fairly broad lines, the measurement errors of the line equivalent widths and residual intensities are determined mainly by the accuracy of the continuum placement. These errors do not exceed 4% for the PFES spectra, where the energy concentration within the order changes greatly, and 2% for the coudè spectra, where the energy distribution along the order is flatter.

Variations from spectrum to spectrum also show up in the intensities of telluric lines. Near Hα, the telluric spectrum is represented mainly by weak water-vapor lines. We will estimate the possible intensity variations of these lines by using the results of a daily monitoring of the water content in the atmosphere

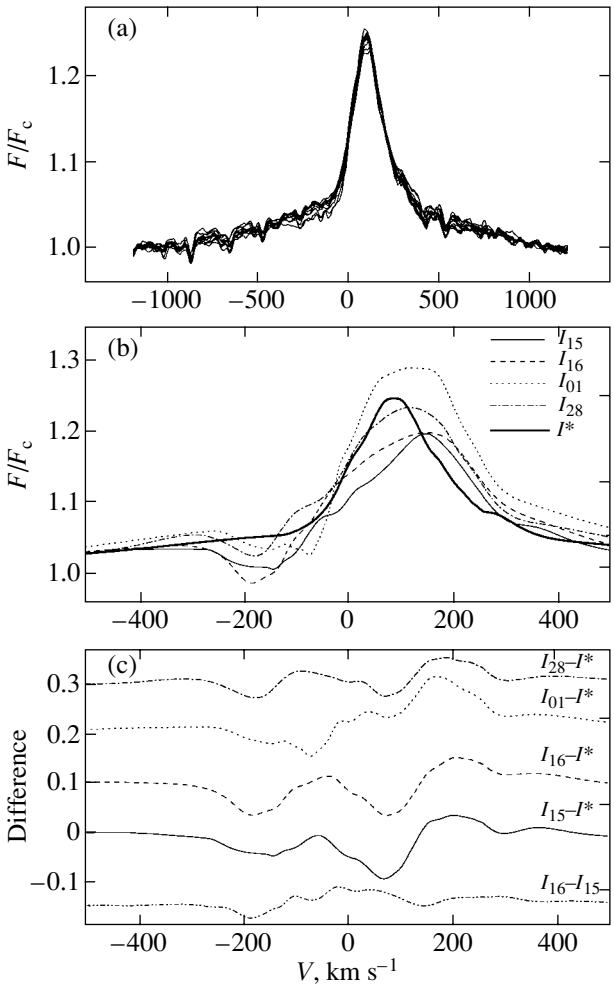

Fig. 1. Hα profiles in the spectrum of α Cam: (a) obtained on February 25, 1997, with the PFES spectrograph of the 6-m SAO telescope; (b) obtained with the CEGS spectrograph of the 2-m ShAO telescope, and the mean of the 11 profiles (I^*) shown in Fig. 1a. The notation of the profiles is the same as that in the table; (c) the differences between the individual CEGS profiles and the mean of the 11 (PFES) profiles. Apart from the profile difference ($I_{15}-I^*$), all of the curves in Fig. 1c were spaced apart along the vertical axis.

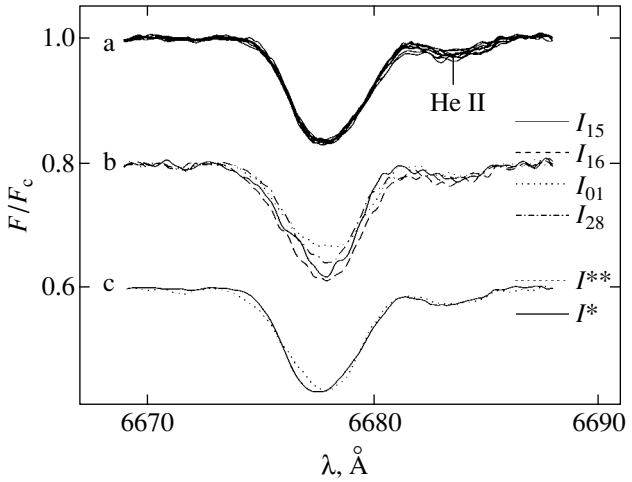

Fig. 2. He I 6678 line profiles in the spectrum of α Cam: (a) and (b) same as Figs. 1a and 1b; (c) I^*, same as Fig. 1b: I^{**}, the mean of the four profiles shown in Fig. 2b. Curves (b) and (c) were displaced downward along the vertical axis.

above the 6-m BTA telescope performed by one of us (V.E. Panchuk) over 11 months (Bergner *et al.* 1978). Let us assume that the change in the intensities of water-vapor lines from spectrum to spectrum is real, i.e., is not the result of errors in the continuum placement. In this case, the typical changes in the line depth are a factor of 1.5 to 2. Based on both the line intensities and the precipitated water level in the atmosphere (1–2 mm) characteristic of February at SAO, we find that these lines are definitely located in the linear segment of the curve of growth. This implies that the line intensity and the number of water vapor molecules change proportionally. We conclude that the total water vapor content will change by several tens of percent in 2 to 3 min, whereas the maximum rate of change of the water content recorded at SAO is 20–25% per hour (Bergner *et al.* 1978). Consequently, the change in the intensities of water-vapor lines from spectrum to spectrum (Fig. 1a) results mainly from the errors in the continuum placement; we estimated these errors from telluric lines (≈1%). Thus, the fast intensity variations (∼1%) on the line profiles in the spectrum of α Cam are systematic in origin.

SPECTROSCOPIC VARIABILITY

The hydrogen lines and all of the He I lines show a common trend over 1.5 h: a decrease in the radial velocity, on average, by about 4 km s^{-1}. For the Hβ and Hγ lines, this decrease is 5 and 6 km s^{-1}, respectively. The large errors of the mean radial velocities estimated from the Hβ and Hγ lines (see the table) are attributable precisely to this decrease. Other lines (C III, C IV, He II, etc.) exhibit no radial-velocity variations, which indirectly confirms that the systematic errors considered above are insignificant. Thus, given the measurement errors, no fast radial-velocity variations (from spectrum to spectrum) have been found.

The Hα emission wings in all our spectra extend to ±1200 km s^{-1} (Fig. 1a). The Hα profiles obtained at the coudè focus of the 2-m ShAO telescope and the mean PFES profile (in what follows, we mean the average of 11 spectra) are shown in Fig. 1b. The PFES spectra taken on the same date exhibit a pure emission profile that resembles the profiles obtained by

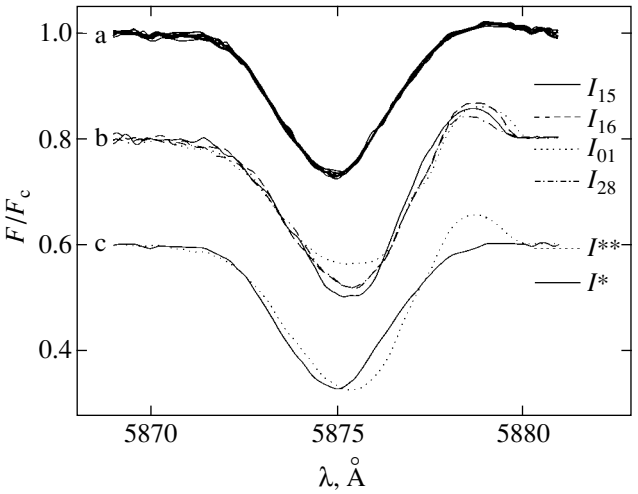

Fig. 3. Same as Fig. 2 for the He I 5876 line.

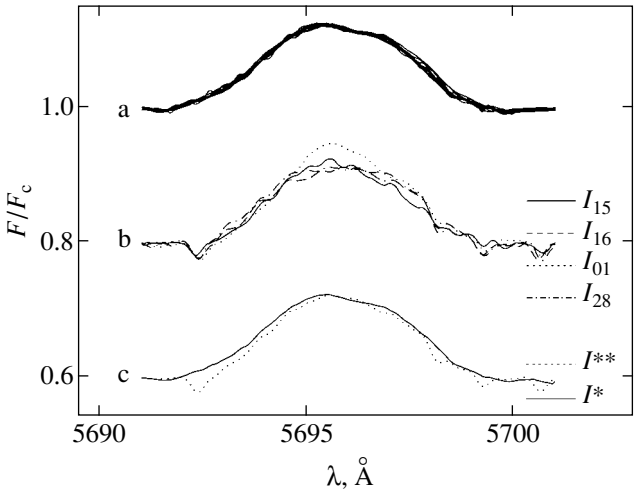

Fig. 4. Same as Fig. 2 for the C III 5695 line.

Markova (2002; Fig. 1, January–February), while the coudè spectra for all four dates exhibit direct P Cyg profiles with variable emission and absorption components. To reveal the main Hα variability regions, we subtracted the mean PFES profile from these four profiles; the corresponding profile differences are shown in Fig. 1c. No variations are observed in the wings where $|V_r| \geq 500$ km s^{-1}, as in the papers by Ebbets (1980) and Markova (2002). Changes in the absorption component occur at radial velocities of -180 ± 20 and -70 ± 10 km s^{-1}, while changes in the emission component occur near 200 ± 20 and 90 ± 10 km s^{-1}. The time difference between the October 15 and 16, 1999 exposures is 23 h; the Hα profile changed appreciably over this period (Fig. 1b). Figure 1c shows the difference between these neighboring profiles. We see that the main changes occur at radial velocities of -180 and 150 km s^{-1}. Note that the feature at a radial velocity of -60 km s^{-1} is not the remnant of a telluric line, but is evidence of real variability; see Fig. 1c ($I_{16} - I_{15}$).

The variability pattern and range (on the radial-velocity scale) confirm the results of the pioneering study by Ebbets (1980), who found the main changes in the Hα profile in the ranges from -300 to -100 and from 100 to 200 km s^{-1} for the absorption and emission components, respectively. Such changes in the Hα profile were pointed out by Kaper *et al.* (1997) and Markova (2002).

The He I λ6678 and 5876 Å line profiles are shown in Figs. 2 and 3, respectively. No fast ($\leq$1.5 h) profile and radial-velocity variations with time have so far been found. In the coudè spectra, He I 6678 (within the limits outside the measurement errors) exhibits intensity and width variations, while the slope of its blue wing remains constant. Symmetric, highly blueshifted absorption profiles are observed for the He I 5876 line in the PFES spectra (Fig. 3a). In contrast, the coudè spectra (as in the paper by Fullerton *et al.* 1996) exhibit a P Cyg profile with variable absorption and emission components (Fig. 3b). As in the case of the He I 6678 line, the line intensity and width vary, while the slope of its blue wing remains constant. The mean PFES and coudè profiles of these two He I lines are compared in Figs. 2c and 3c. We see that the slopes of the blue and red halves of the absorption profile also change on a long time scale. Since the red wing of the He I 6678 line is blended with the He II 6683 line, the presence of an emission component cannot be judged (Fig. 2).

C III-5695, the second strongest emission line in the spectrum of α Cam after Hα, is probably also sensitive to stellar-wind variations. The PFES spectra of this line are shown in Fig. 4a. No fast profile and radial velocity variations over time have so far been found. Two small bulges that correspond to mean radial velocities of -8.0 ± 5.0 and 60.0 ± 5.0 km s^{-1} are clearly seen in the profile. The coudè spectra exhibit small profile and radial velocity variations (Fig. 4b). The amplitude of the radial velocity variations was estimated from our data to be about 4 km s^{-1}. The profile varies at radial velocities of -5.0 ± 5.0 and 90.0 ± 10 km s^{-1}. On August 1, 2000, when the most intense emission was observed in the Hα line (Fig. 1b), the intensity of the C III-5695 line was also at a maximum (Fig. 4b). The mean PFES and coudè profiles are compared in Fig. 4c. From them, we may conclude with confidence that the equivalent width on long time scales varies primarily through the line width rather than the line intensity. Note that the behavior of the two unidentified emission features in the

spectrum of α Cam is similar to that of the C III 5695 emission line. Assuming that these emission lines originate in the same atmospheric layers and show the same radial velocity, we have determined the effective wavelengths for them. The effective wavelengths derived from the 11 PFES spectra in this way are $\lambda 4485.836 \pm 0.011$ and 4504.178 ± 0.021 Å. From the table by Kaufmann and Martin (1993), they correspond to the S IV 4485.609 and S IV 4504.095 lines.

The He II 4686 line exhibits an inverse P Cyg profile. According to Kholtygin *et al.* (2000), after the reduction of these spectra, this line has a direct P Cyg profile that shows fast variations over time. We emphasize that the He II 4686 line is located in a segment of the PFES echelle frame where unreliable continuum placement without an additional check can lead to noticeable changes in the profile from spectrum to spectrum. As we see from Fig. 5, no fast (less than 1.5 h) profile variations are observed in our data. The small variations ($r \leq 0.005$) are most likely related to the continuum placement procedure. In analyzing these observations of α Cam, Kholtygin *et al.* (2000) used a variety of frequency filtering, the WPS method that was successfully used to analyze the wind inhomogeneities in Wolf–Rayet stars (Lepine *et al.* 1996). This method works with the spectroscopic signal obtained by subtracting the individual spectra from the mean spectrum; thus, the continuum placement procedure is unnecessary. The method provides information about the square of the amplitude of the mean deviation at a selected frequency; i.e., it allows the dominant spatial frequency to be isolated. Kholtygin *et al.* (2000) isolated three variable components from the power spectrum constructed for the wavelength range $\lambda\lambda 4658$–4720 Å: a small-scale component with the dominant frequency corresponding to the 0.25 Å interval; a medium-scale component with an interval of about 4 Å; and a large-scale component with an interval of about 50 Å. We associate the dominant spatial interval of the noise component with the sampling step (the reciprocal linear PFES dispersion in the order under consideration is 0.11 Å pixel^{-1}) and with the presence of a defective array column in the spectral range being studied. In our opinion, the large-scale component contains information only about the length of the part (62 Å) of the spectral order in which the energy distribution can slightly vary from spectrum to spectrum due to the nonideal repetition of the procedure for "cutting" the vectors out of the echelle frame. The medium-scale component corresponds to an interval that almost coincides with the full width of the P Cyg profile, which is direct as implied by the data from Kholtygin *et al.* (2000) and inverse as implied by our data. Kholtygin *et al.* (2003), who carried out a study

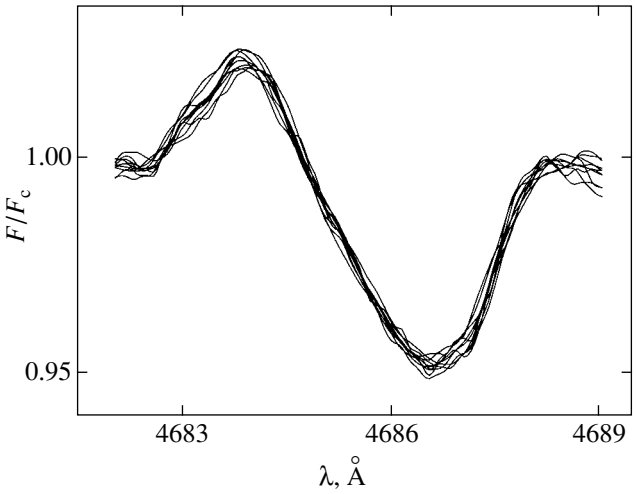

Fig. 5. He II 4686 line profiles taken on February 25, 1997, with the PFES spectrograph of the 6-m SAO telescope.

with a spectral resolution of $R = 40\,000$, provided no information about the shape and variability of the He II 4686 line profile in the spectrum of α Cam. Therefore, we believe that the physical interpretation of the medium-scale component is premature.

DISCUSSION

Based on a detailed analysis of the variations in the C IV $\lambda 5801$, 5812 Å, and He I 5876 line profiles, Fullerton *et al.* (1996) established that these lines originated in different atmospheric layers (the first two lines originated in deep photospheric layers, while the last line originated in the layers where the stellar wind flows out), and that the patterns and behaviors of their variability were identical. This means that the profile variability of these lines was caused by the same processes. By comparing the parameters of these variabilities and their distributions in the H–R diagram, they showed that these variabilities were caused by nonradial pulsations. Independent simulations also showed that the observed line profile variabilities were caused by nonradial pulsations (Fullerton *et al.* 1996; Fig. 1).

The He I 5876 and He I 6678 profile variabilities that we found (Figs. 2b and 3b) as well as the profiles of other absorption features listed in the table are very similar to those found by Fullerton *et al.* (1996; Figs. 1 and 2). Therefore, the line profile variability in the atmosphere of α Cam is attributable to nonradial pulsations.

The radial velocities of the He I 5876 and He I 6678 lines are even more negative than those for the group

of He I lines (see the table). This suggests that the absorption components of these lines originate in layers that are continuously expanding relative to the underlying atmospheric layers. These facts for the He I 5876 and He I 6678, respectively, were also pointed out by Fullerton *et al.* (1996) and Markova (2002). In contrast to these authors, who analyzed two or three lines, our data cover a wide spectral range, which allows us to study various lines or groups of lines. A comparison of their radial velocities in the table indicates that the radial velocity is stratified in the atmosphere of α Cam; i.e., the expansion velocity increases from lower to upper atmospheric layers. As we see from the table, the radial velocities themselves, their mean values and amplitudes differ for different atmospheric layers (where these lines originate), suggesting that the pulsation parameters probably differ for different atmospheric layers.

If we take 11 km s^{-1} (Gies and Bolton 1986) as the radial velocity of the star's center of mass, we find that variations in the absorption and emission components of the Hα line, on average, occur at radial velocities that are symmetric relative to the radial velocity of the star's center of mass. On August 1, 2000, when the emission was strongest in the Hα line, we observed not only an enhancement of the emission in the C III 5695, S IV 4485, and S IV 4504 lines, but also the lowest intensities for all of the absorption lines. A large-scale mass ejection may have been observed at this time; this ejection is also traceable in other spectral lines.

At this time, the blue wing of the Hα line exhibited two absorption components with radial velocities of about -171 and -96 km s^{-1} (see Fig. 1b and the table). Fullerton *et al.* (1996) pointed out that the nonradial pulsations of lower atmospheric layers accompanied the changes in the wind structure. The presence of a second low-velocity (since this takes place in the layers where the stellar wind originates) component is probably consistent with this explanation.

The samples of Hα profile variability that were obtained by us and by Markova (2002) are as follw:

June–July: cases with alternations of strengthened and weakened emission components relative to the star's center of mass;

December–January: two wavelike variabilities, one with a strengthened emission component and the other with a weakened emission component;

the sudden appearance of a blueshifted strengthened emission component (June–July) and a blueshifted strengthened absorption component (December–January);

others closely resemble the samples of V/R variability observed for BA supergiants (Kaufer *et al.* 1996). Therefore, we have concluded that the Hα profile variability in the spectrum of the supergiant α Cam is symmetric relative to the radial velocity of the star's center of mass and is the result of variable blueshifted and redshifted emission and/or absorption components superimposed on a variable photospheric profile.

Glatzel *et al.* (1999) showed that there are strange-mode instabilities in a massive star similar to α Cam that generate perturbations at the base of the wind. These instabilities provide the star with nonradial oscillations and generate large-scale wind structures of various geometries that can be modulated by rotation. Consequently, as was pointed out by Fullerton *et al.* (1996), the observed changes in the structure of the wind from α Cam could be attributed in part to the nonradial pulsations of the underlying atmospheric layers.

CONCLUSIONS

It should be noted that, due to its high luminosity and position in the sky ($\delta = 66°$), the supergiant α Cam is a convenient object for observations, and in many cases it has been included in the list of hot O stars being studied. However, the line profile variability in the spectrum of this star differs from that of other O stars.

In the ultraviolet, the line profile variability pattern for α Cam also differs greatly from that for similar O stars. For example, the UV spectrum of the similar supergiant 19 Cep (O9.5 Ib) clearly shows discrete absorption components, their variability and migration over the profile (Kaper *et al.* 1997). At the same time, based on the UV spectrograms obtained for α Cam over five days, the above authors not only detected no discrete absorption components, but also found no significant variations in the broad line profiles.

Gathier *et al.* (1981) recognized that their evidence for the presence of narrow discrete absorption components in the Si III, Si IV, N V, and O VI line profiles (based on Copernicus data) was unreliable. On the other hand, based on the same IUE data, de Jager *et al.* (1981), Prinja and Howarth (1986), and Lamers *et al.* (1988) provided conflicting evidence for the profile variability of intense resonance lines.

The foregoing indicates that, in contrast to other O stars, no clear evidence for the existence of discrete absorption components and line profile variability has been found in the UV spectrum of α Cam.

Our studies have revealed no fast line profile and radial velocity variations in the spectrum of α Cam. Significant variability is observed only on a time scale

of a day or more. The Hα profile variability is symmetric relative to the radial velocity of the star's center of mass and is the result of variable blueshifted and redshifted emission and/or absorption components superimposed on a variable photospheric profile. A large-scale mass ejection from the stellar surface is occasionally observed; this ejection is also traceable in all spectral lines.

The data on the profile and radial velocity variability obtained from optical spectra suggest that the line profile variations in the spectrum of α Cam are probably attributable to nonradial pulsations. As Ledoux (1951) showed, rapid rotation is a necessary condition for the existence of stable pulsations. The pulsation parameters probably differ for different atmospheric layers.

ACKNOWLEDGMENTS

We wish to thank M.V. Yushkin for help with spectrogram reduction and V.G. Klochkova and E.L. Chentsov for a discussion of the results. This work was supported in part by the Russian Foundation for Basic Research (project no. 02-02-16085) and the Extended Objects in the Universe program of fundamental research of the Department of Physical Sciences of the Russian Academy of Sciences.

REFERENCES

1. I. I. Balega, Yu. Yu. Balega, V. A. Vasyuk, and V. G. Orlov, Astrofiz. Issled. (Izv. Spets. Astrofiz. Obs.) **29**, 67 (1990).
2. Yu. K. Bergner, A. V. Krat, S. M. Morozov, *et al.,* Astrofiz. Issled. (Izv. Spets. Astrofiz. Obs.) **10**, 52 (1978).
3. A. Blaaw, Bull. Astron. Inst. Netherl. **15**, 265 (1961).
4. B. Bohannan and C. D. Garmany, Astrophys. J. **223**, 908 (1978).
5. E. L. Chentsov, Astrophys. Space Sci. **232**, 217 (1995).
6. A. M. Cherepashchyuk, Astron. Zh. **67**, 955 (1990) [Sov. Astron. **34**, 481 (1990)].
7. P. S. Conti and D. Ebbets, Astrophys. J. **213**, 438 (1977).
8. D. Ebbets, Astrophys. J. **235**, 97 (1980).
9. D. Ebbets, Astrophys. J., Suppl. Ser. **48**, 399 (1982).
10. A. W. Fullerton, *ESO Workshop: Rapid Variability of OB-stars: Nature and Diagnostic Value*, Ed. by D. Baade (1991), p. 3.
11. A. W. Fullerton, *IAU Coll. No. 169: Variable and Non-spherical Winds in Luminous Hot Stars*, Ed. by B. Volf, O. Stahl, and A. W. Fullerton; Lect. Notes Phys. **523**, 3 (1999).
12. A. W. Fullerton, D. R. Gies, and C. T. Bolton, Astrophys. J., Suppl. Ser. **103**, 475 (1996).
13. G. A. Galazutdinov, Preprint No. 92, SAO RAN (Special Astrophysical Observatory, Russian Academy of Sciences, Nizhniĭ Arkhyz, 1992).
14. G. A. Galazutdinov, F. A. Musaev, J. Krelowski, and G. A. H. Walker, Publ. Astron. Soc. Pac. **112**, 648 (2000).
15. R. Gathier, H. J. G. J. M. Lamers, and T. P. Snow, Astrophys. J. **247**, 173 (1981).
16. D. R. Gies and C. T. Bolton, Astrophys. J., Suppl. Ser. **61**, 419 (1986).
17. W. Glatzel, M. Kiriakidis, S. Chemigovskij, *et al.*, Mon. Not. R. Astron. Soc. **303**, 116 (1999).
18. A. A. Ivanov, V. E. Panchuk, and V. S. Shergin, Preprint No. 155, SAO RAN (Special Astrophysical Observatory, Russian Academy of Sciences, Nizhniĭ Arkhyz, 2001).
19. L. Kaper, H. F. Henrichs, J. Nichols, *et al.*, Astron. Astrophys., Suppl. Ser. **116**, 257 (1996).
20. L. Kaper, H. F. Henrichs, and A. W. Fullerton, Astron. Astrophys. **327**, 281 (1997).
21. L. Kaper, H. F. Henrichs, J. Nichols, and J. H. Telting, Astron. Astrophys. **344**, 231 (1999).
22. A. Kaufer, O. Sthal, B. Wolf, *et al.*, Astron. Astrophys. **305**, 887 (1996).
23. V. G. Klochkova, private communication (1994).
24. V. G. Klochkova and G. A. Galazutdinov, Preprint No. 71, SAO RAN (Special Astrophysical Observatory, Russian Academy of Sciences, Nizhniĭ Arkhyz, 1991).
25. V. G. Klochkova, S. E. Ermakov, V. E. Panchuk, *et al.,* Preprint No. 137, SAO RAN (Special Astrophysical Observatory, Russian Academy of Sciences, Nizhniĭ Arkhyz, 1999).
26. A. F. Kholtygin, F. V. Kostenko, N. A. Kudryashova, and L. M. Oskinova, *Thermal and Ionization Aspects of Flows from Hot Stars: Observation and Theory*, Ed. by H. J. G. L. M. Lamers and A. Sapar; Astron. Soc. Pac. Conf. Ser. **204**, 227 (2000).
27. A. F. Kholtygin, D. N. Monin, A. E. Surkov, and S. N. Fabrika, Pis'ma Astron. Zh. **29**, 222 (2003) [Astron. Lett. **29**, 175 (2003)].
28. F. V. Kostenko and A. F. Kholtygin, Astrofizika **41**, 423 (1998).
29. H. J. G. J. M. Lamers, T. P. Snow, C. de Jager, and A. Langerwerf, Astrophys. J. **325**, 342 (1988).
30. P. Ledoux, Astrophys. J. **114**, 373 (1951).
31. S. Lepine, A. F. J. Moffat, and R. N. Henriksen, Astrophys. J. **466**, 392 (1996).
32. O. J. Lee, Astrophys. J. **37**, 1 (1913).
33. H. Mandel, *IAU Symp. No. 132: The Impact of Very High S/N Spectroscopy on Stellar Physics,* Ed. by G. Cayrel de Strobel and M. Spite (Kluwer Acad., 1988), p. 9.
34. N. Markova, Astron. Astrophys. **385**, 479 (2002).
35. F. A. Musaev, Pis'ma Astron. Zh. **19**, 776 (1991).
36. F. A. Musaev and L. I. Snezhko, Pis'ma Astron. Zh. **14**, 163 (1988) [Sov. Astron. Lett. **14**, 68 (1988)].
37. V. E. Panchuk, I. D. Najdenov, V. G. Klochkova, *et al.*, Bull. Spec. Astrophys. Observ. **44**, 127 (1998).

38. V. E. Panchyuk, V. G. Klochkova, M. V. Yushkin, *et al.,* Preprint No. 159, SAO RAN (Special Astrophysical Observatory, Russian Academy of Sciences, Nizhniĭ Arkhyz, 2001).
39. V. E. Panchyuk, V. G. Klochkova, N. E. Piskunov, *et al.,* Preprint No. 170, SAO RAN (Special Astrophysical Observatory, Russian Academy of Sciences, Nizhniĭ Arkhyz, 2002).
40. R. K. Prinja and I. D. Howarth, Astrophys. J., Suppl. Ser. **61**, 357 (1986).
41. G. Rauw, M. de Becker, and J. M. Vreux, Astron. Astrophys. **399**, 287 (2003).
42. A. Kh. Rzayev, Bull. Spec. Astrophys. Observ. **54**, 66 (2002).
43. A. Kh. Rzayev, N. O. Gasanov, Kh. M. Mikailov, *et al.,* Tsirk. Shamakh. Astrofiz. Obs., No. 95, 3 (1999a).
44. A. Kh. Rzayev, Kh. M. Mikailov, M. É. Shyukyurov, *et al.,* Tsirk. Shamakh. Astrofiz. Obs., No. 97, 3 (1999c).
45. R. C. Stone, Astrophys. J. **232**, 520 (1979).
46. R. C. Stone, Astrophys. J. **261**, 208 (1982).
47. V. S. Shergin, private communication (2000).
48. A. B. Underhill, Astrophys. J. **199**, 691 (1975).
49. B. Volf, O. Stahl, and A. W. Fullerton, *IAU Toll. No. 169: Variable and Non-Spherical Winds in Luminous Hot Stars*; Lect. Notes Phys. **523**, 424 (1999).
50. M. V. Yushkin, Candidate's Dissertation in Mathematical Physics (Nizhniĭ Arkhyz, 2002).
51. S. K. Zeĭnalov and F. A. Musaev, Pis'ma Astron. Zh. **12**, 304 (1986) [Sov. Astron. Lett. **12**, 125 (1986)].
52. S. K. Zeĭnalov, F. A. Musaev, and E. L. Chentsov, Astrofiz. Issled. (Izv. Spets. Astrofiz. Obs.) **21**, 3 (1986).

Translated by V. Astakhov

Astronomy Letters, Vol. 30, No. 5, 2004, pp. 343–348. Translated from Pis'ma v Astronomicheskiĭ Zhurnal, Vol. 30, No. 5, 2004, pp. 387–392.

Reproducible Characteristics of the Solar Wind Acceleration

N. A. Lotova[1*], K. V. Vladimirskiĭ[2], V. N. Obridko[1], and I. A. Subaev[2]**

[1] *Institute of Terrestrial Magnetism, Ionosphere, and Radiowave Propagation, Russian Academy of Sciences, Troitsk, Moscow oblast, 142190 Russia*

[2] *Lebedev Institute of Physics, Russian Academy of Sciences, Leninskiĭ pr. 53, Moscow, 117924 Russia*

Received September 30, 2003

Abstract—In experiments that were regularly carried out in 1999–2002 with Pushchino radio telescopes (Russian Academy of Sciences), the study of the radial dependence of the scattering of radio emission from compact natural sources was extended to regions of circumsolar plasma farther from the Sun. Based on a large body of data, we show that, apart from the standard transonic acceleration region located at distances of 10–40 $R_\odot$ from the Sun, there is a region of repeated acceleration at distances of 34–60 $R_\odot$ attributable to the equality between the solar wind velocity and the Alfvénic velocity. The repetition in the trans-Alfvénic region of the characteristic features of the radial stream structure observed in the transonic region (the existence of a precursor, a narrow region of reduced scattering that precedes a wide region of enhanced scattering) suggests that the main characteristic features of the resonant acceleration of solar wind streams are preserved up to distances of the order of 60 $R_\odot$. © *2004 MAIK "Nauka/Interperiodica".*

Key words: *Sun, circumsolar plasma, solar wind, transonic and trans-Alfvénic solar wind regions.*

INTRODUCTION

Studying the sources and formation processes of solar wind streams is one of the pressing problems in modern solar physics. Experimental studies of the circumsolar-plasma acceleration mechanisms are related mainly to the potentialities of the sounding method and to scintillation or radio-wave scattering observations. In both cases, the emission from compact natural sources is used. Attention is focused on regions at small distances from the Sun where the stream structure is formed and where the solar wind streams are accelerated.

An important result of previous studies was the detection of the transonic transition region, whose existence was not predicted by the theory, where the main acceleration takes place and where the solar-wind stream becomes supersonic (Lotova *et al.* 1985, 1998; Lotova 1988, 1992). The transition region is located at radial distances of $\sim$10–40$R_\odot$ from the Sun, where $R_\odot$ is the solar radius. In the transition region, the flow is mixed: the subsonic and supersonic streams coexist and interact in space. Of unquestionable interest is the extension of studies to regions of interplanetary plasma farther from the Sun in order to clarify the subsequent fate of the flow and its stream structure. In 1999–2002, regular studies of the solar wind were extended to radial distances up to 60–70$R_\odot$. A considerable amount of data to be discussed below were accumulated in these experiments.

THE REGIONS OF INTENSE SOLAR WIND ACCELERATION

The following radio wave scattering parameters are studied in radio-astronomical experiments: the scattering angle $2\theta(R)$ and the scintillation index $m(R)$ (Lotova *et al.* 1985; Lotova 1988). The transition region is detected here as an extended region of enhanced scattering. Figure 1 shows examples of the transition region localization, as determined from the radial dependence of the scattering angle $2\theta(R)$; the scale is logarithmic on both axes. Figure 1a shows the observations of the sources 3C 215 ($\triangle$) and 3C 225 ($\bigcirc$) at $\lambda = 2.7$ m in August 2001. Figure 1b shows the observations of the sources 3C 133 ($\bigcirc$), 3C 154 ($\triangle$), 3C 162 ($\square$), and 3C 172 ($\triangledown$) at $\lambda = 2.9$ m in June 1991. The open symbols in Fig. 1 correspond to the phase at which the source approaches the Sun (eastern hemisphere), and the filled symbols correspond to the recession phase (western hemisphere). In Fig. 1, we clearly see a wide region of enhanced scattering; it is revealed by a comparison with the asymptotic dependence, $2\theta(R) \sim R^{-1.6}$, typical of the subsonic solar wind region (Lotova *et al.* 1997).

An important structural feature of the radial dependence of scattering is the precursor of the transition region—a narrow region of sharply reduced

[*] E-mail: helen@izmiran.rssi.ru
[**] E-mail: solter@izmiran.rssi.ru

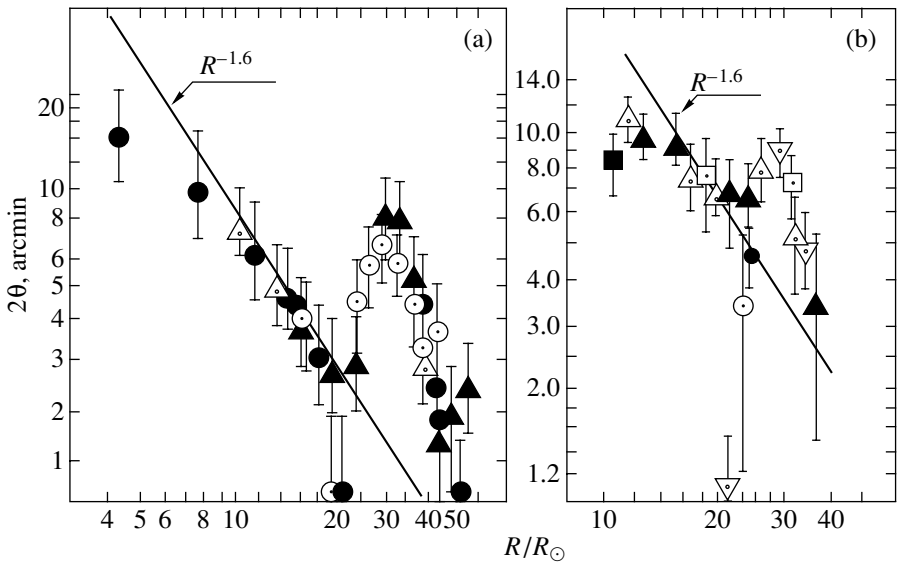

Fig. 1. Localization of the transonic transition region of the solar wind.

scattering that precedes the wide region of enhanced scattering (Fig. 1). The precursor region is observed both when studying the radial dependence of the scattering angle $2\theta(R)$ and when measuring the scintillation index $m(R)$. The width of the precursor region is small. In a typical series of daily scattering measurements, the precursor region corresponds to one-day observations, a result of the measurements being reduced by more than a factor of 2 compared to the scattering level in the subsonic region. This reduction in scattering is real and exceeds significantly the order of magnitude of the possible deviations related to instrumental measurement errors. The observations of the subsequent days yield a result that exceeds the scattering level in the subsonic region. Fast changes in scattering in the precursor region correspond to fast changes in the state of the matter and to fast changes in the solar wind stream velocity. Rough order-of-magnitude estimates of these changes can be obtained by using the standard continuity equation constructed by assuming that the flow is spherically symmetric (Muhleman and Anderson 1981). As applied to the processes without significant changes in the distance from the Sun, the equation has the following simple form:

$$N(R)V(R) = \text{const},$$

where N is the electron plasma density, and V is the solar-wind flow velocity. Thus, a rapid doubling of the flow velocity and then a rapid decrease in velocity when the initial scattering level is recovered follow from the twofold decrease in scattering in the precursor region.

Of course, the mechanism of the rapid variations in the state of the circumsolar plasma in the precursor region requires further detailed study. Since the available experimental data tell us little about the particular features of the process, the problem appears to be difficult. In the complex problem of studying the formation of supersonic solar wind streams, the very existence of the precursor effect turned out to be quite useful. The small width of the precursor region allows us to use the quantity R_p—the distance from the Sun at which this effect arises—in determining the inner boundary of the transition region. The location of this boundary is used as a parameter that describes the intensity of the solar wind acceleration (Lotova *et al.* 1995a, 1995b).

Previously, we considered the parameters of the solar wind flow at relatively short distances from the Sun, $R \sim 10$–$30R_\odot$. Our study of the radial dependence of the flow velocity over a wider distance range shows that the solar wind acceleration is not continuous and monotonic. This conclusion was first drawn by Muhleman and Anderson (1981) from experimental data on the delay of radio signals and, accordingly, on the distribution of matter along the path connecting the Viking spacecraft to the ground-based station. The deviation of the electron density from the inverse-square dependence on the radial distance from the Sun made it possible to reveal two zones of intensive solar wind stream acceleration, near 20 and $50R_\odot$. The complex, nonmonotonic pattern of the acceleration process was subsequently confirmed by direct methods of measuring the solar wind velocity (Yakovlev *et al.* 1980, 1988; Efimov *et al.* 1990; Tokumaru *et al.* 1995; Efimov 1994). More complete

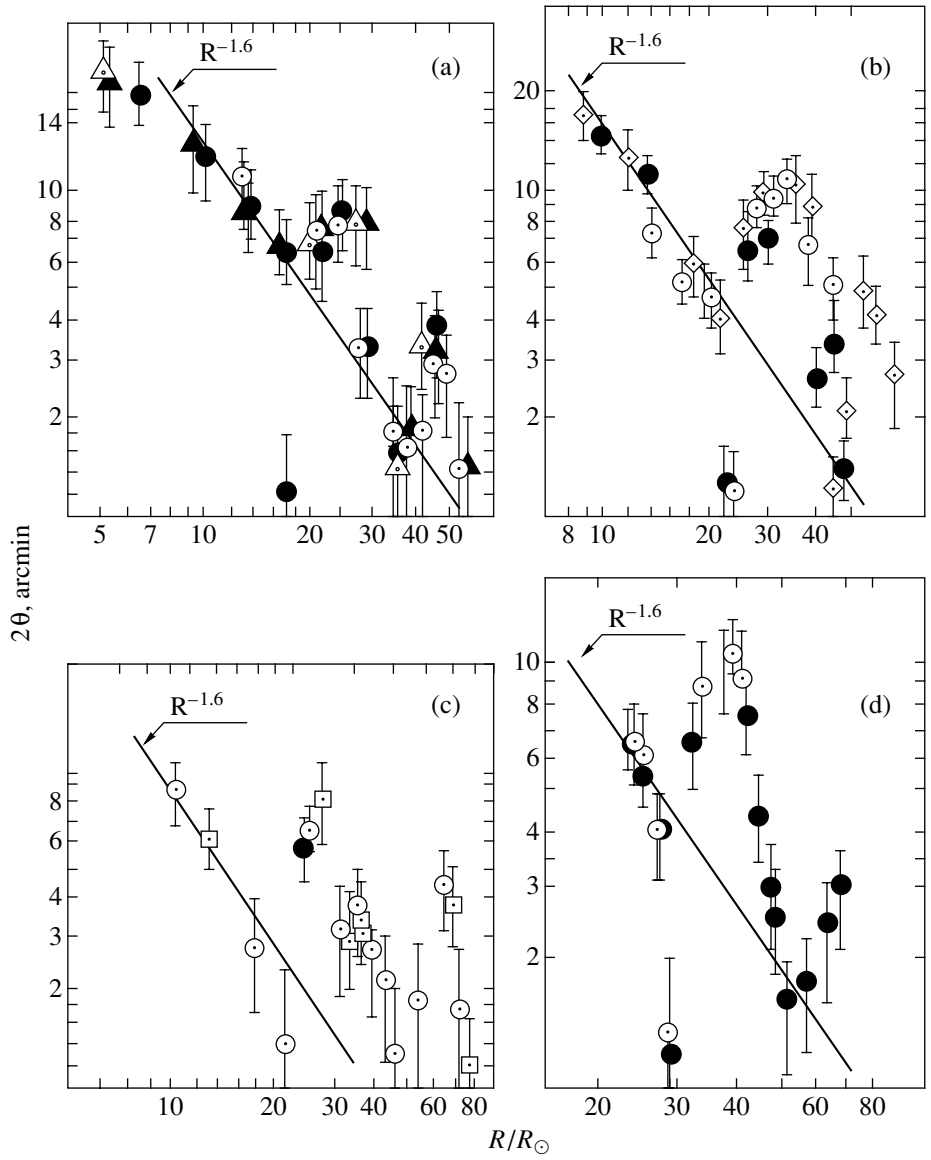

Fig. 2. Examples of the radial dependence of the scattering angle.

diagnostics of the solar wind acceleration requires continuous series of data on the radial dependence of the solar wind velocity over a wide range of radial distances, $R \approx 3$–$80R_\odot$, compared with radio wave scattering data. Figure 2 shows the results of our experiments, examples of the radial dependence of the scattering angle $2\theta(R)$ measured over a wide range ($R \approx 5$–$70R_\odot$). The symbols used here for various sources are: in Fig. 2a, for the observations of the sources 3C2 (◯), 3C5 (△) in March 2000; in Fig. 2b, for the observations of 3C144 (◯), 3C166 (◇) in June 2000; in Fig. 2c, for the observations of 3C2 (◯), 3C5 (□) in March 2001; and in Fig. 2d, for the observations of 3C138 (◯) in June 2000. The open and filled symbols, as in Fig. 1, distinguish the observations referring to the phase when the source approaches to and recedes from the Sun. We see from Fig. 2 that, apart from the known transition region, enhanced scattering is repeated in regions farther from the Sun, at distances $R \sim 40$–$70R_\odot$; the same structural features that determine the flow acceleration in the transition region are repeated here: the narrow region of reduced scattering that precedes the wide region of enhanced scattering.

The results of our observations in the period 1999–2002 are summarized in the table. The table lists the experiment number, the sounding source, the date on which the transition-region precursor was observed, and its coordinates: the sounded hemisphere (E/W), the distance from the Sun R_{p_1}, and the heliolatitude φ_1; and the date of detection of the second precursor

Positions of the scattering minima R_{p_1} and R_{p_2} in the transonic and Alfvénic regions in the solar-wind acceleration process

N	Source	E/W	Date	$R_{p_1}/R_\odot$	φ_1, deg	Date	$R_{p_2}/R_\odot$	φ_2, deg
1	3C2	E	Mar. 18, 1999	15.5	−12	Mar. 13, 1999	34.0	−6.5
2	3C5	E	Mar. 20, 1999	16.5	−6.7	Mar. 15, 1999	35.0	−4.2
3	3C2	E	Mar. 17, 2000	17.5	−11.1	Mar. 11, 2000	38.0	−5.9
4	3C2	W	Mar. 24, 2000	17.5	−7.0	Apr. 1, 2000	38.0	−2.0
5	3C5	E	Mar. 19, 2000	18.0	–	Mar. 13, 2000	36.0	−4.1
6	3C5	W	Mar. 28, 2000	19.0	–	Apr. 3, 2000	38.0	0.3
7	3C133	W	June 20, 2000	23.5	30.5	June 21, 2000	47.5	18.1
8	3C138	W	June 15, 2000	28.0	−51.2	June 24, 2000	52.0	−0.6
9	3C144	W	June 21, 2000	22.5	−5.0	June 29, 2000	50.5	1.9
10	3C154	E	June 18, 2000	23.0	17.9	June 12, 2000	43.0	6.0
11	3C166	E	June 26, 2000	21.5	−23	June 19, 2000	46.0	−14.1
12	3C207	W	Aug. 6, 2000	25.5	−40	Aug. 15, 2000	54.0	−14.6
13	3C208	W	Aug. 10, 2000	26.0	−25.3	Aug. 19, 2000	56.0	−8.8
14	3C212	W	Aug. 11, 2000	27.0	−18.2	Aug. 18, 2000	48.0	−8.2
15	3C228	W	Aug. 23, 2000	21.0	8.2	Aug. 30, 2000	44.0	7.7
16	3C2	E	Mar. 16, 2001	21.0	−9.3	Mar. 9, 2001	45.0	−5.3
17	3C5	E	Mar. 18, 2001	22.0	−5.5	Mar. 11, 2001	45.0	−3.8
18	3C154	E	June 20, 2001	18.0	26.3	June 14, 2001	38.0	8.1
19	3C172	E	–	∼18.0	–	June 25, 2001	38.0	7.8
20	3C207	W	Aug. 4, 2001	21.0	−53.6	Aug. 13, 2001	46.0	−18.0
21	3C208	W	Aug. 8, 2001	19.0	−37.6	Aug. 15, 2001	42.0	−12.3
22	3C275	W	Oct. 10, 2001	21.5	−6.4	Oct. 17, 2001	47.5	−4.6
23	3C279	W	Oct. 14, 2001	21.5	−3.1	Oct. 21, 2001	46.0	−3.3
24	W31(2)	E	Dec. 21, 2001	17.0	56.3	Dec. 30, 2001	26.0	22
25	W31(2)	W	Dec. 27, 2001	17.5	40.3	Jan. 1, 2002	34.0	15
26	3C2	E	Mar. 17, 2002	18.5	−10.5	Mar. 11, 2002	38.0	−6.0
27	3C5	E	Mar. 19., 2002	18.5	−6.2	Mar. 15, 2002	38.0	−4.0
28	3C207	W	Aug. 1, 2002	18.0	−79.5	Aug. 8, 2002	36.0	−24.0
29	3C208	E	Aug. 1, 2002	17.5	−52.0	Aug. 13, 2002	36.0	−16.0
30	3C215	W	Aug. 13, 2002	23.0	5.4	Aug. 19, 2002	45.0	4.6
31	3C225	E	Aug. 11, 2002	18.0	−2.0	Aug. 24, 2002	33.0	3.2
32	3C225	W	Aug. 22, 2002	21.5	3.4	Aug. 28, 2002	43.0	3.1
33	3C228	W	Aug. 22, 2002	16.0	17.3	Aug. 27, 2002	34.0	9.4
34	IRC-20 431	W	Dec. 29, 2002	18.0	7.0	Jan. 2, 2003	34.0	0.0
35	W28 A2(1)	W	Dec. 27, 2002	18.0	−14.0	Dec. 31, 2002	34.0	−11.0
36	W31(2)	W	Dec. 28, 2002	20.0	32.0	Jan. 3, 2003	40.0	12.0

R_{p_2} and its coordinates: E/W, R_{p_2}, and φ_2. The data in the table show that there are persistent regions of intense acceleration with identical structural features in the circumsolar plasma. In the transitional region, these features were related to the flow acceleration near the critical sonic point and to the subsequent flow deceleration (Lotova *et al.* 1992, 1993). Based on the repetition of structural features of the transition region in more distant regions of the medium, it would be natural to associate the second region with the recurrent, additional flow acceleration near the Alfvénic critical point. Thus, the solar wind flow acceleration is not continuous and monotonic: in the discrete regions determined by the critical points, the above rapid changes in velocity of both signs arise.

CORRELATION BETWEEN THE TWO REGIONS OF FLOW ACCELERATION

The data of the table show that the positions of the R_{p_1} and R_{p_2} precursors change over wide ranges: $R_{p_1} \approx 16$–$27R_\odot$ and $R_{p_2} \approx 34$–$56R_\odot$. These data allow us to study the correlation between the spatial positions of the flow acceleration regions. In Fig. 3, the position of the R_{p_2} precursor is plotted against the position of the R_{p_1} precursor: △ = the fast flows associated with the streamer periphery or with local coronal holes; ● = the slow flows identified with the main body of the streamer; ◯ = the slower flows identified with the ray structure of the white corona (LASCO, C2, SOHO); and ◊ = the slowest flows identified with equatorial coronal holes. The flow types were determined from the correlation diagram that relates the position of R_{in}, the inner boundary of the transition region, to $|B_R|$, the magnetic field strength on the source surface, $R = 2.5R_\odot$. The correlation analysis that reveals various branches in the $R_{in}(|B_R|)$ dependence was complemented with calculations of the coronal magnetic field topology and with SOHO data on the white-corona structure (Lotova *et al.* 2002). Figure 3 shows that a common $R_{p_2}(R_{p_1})$ correlation is observed for the flows of different types. The slowest flows (◯) dominate in the upper part of this dependence, while the fast flows (△) dominate in its lower part.

DISCUSSION AND RESULTS

Our study of the radial dependence of radio-wave scattering by two independent methods of observations—using the scattering angle $2\theta(R)$ and the scintillations $m(R)$—over the wide range of radial distances ($R \approx 5$–$70R_\odot$) where the supersonic solar wind is formed reveals persistent discrete regions in which the main and additional intense flow acceleration takes place. The positions of these regions on the radial distance scale are defined as the positions of narrow regions with sharply reduced scattering (precursors) followed by wide regions with enhanced scattering. These regions arise when the flow velocity is equal to the magnetic sound velocity or the Alfvénic velocity, which leads us to conclude that intense flow acceleration results from the resonant interaction between waves and plasma particles. The existence of a common correlation independent of the flow type between the spatial positions of the regions of main and additional acceleration suggests that the flow type determined by the initial conditions in the solar corona, the magnetic field structure and strength at the base of the streamline is preserved in the complex acceleration process up to distances of ~ 60–$70R_\odot$.

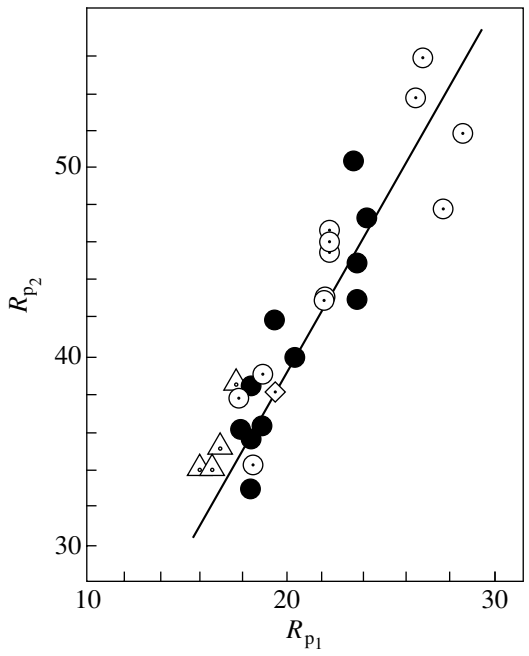

Fig. 3. Spatial position of the R_{p_2} precursor as a function of the R_{p_1} position.

ACKNOWLEDGMENTS

The observations were carried out with the RT-22 radio telescopes (registration number 01-10) and DKR-1000 (registration number 01-09). This work was supported by the Astronomy program, the Russian Foundation for Basic Research (project no. 01-02-16308), and the Presidential Program for Leading Scientific Schools (project no. 00-15-96661).

REFERENCES

1. A. I. Efimov, Space Sci. Rev. **70**, 397 (1994).
2. A. I. Efimov, I. V. Chashei, V. I. Shishov, and O. I. Yakovlev, Kosm. Issled. **28**, 581 (1990).

3. N. A. Lotova, Sol. Phys. **117,** 399 (1988).
4. N. A. Lotova, in *Proceedings of the 3rd COSPAR Colloquium: Solar Wind Seven,* Ed. by E. Marsch and R. Schwenn (Pergamon, 1992), p. 217.
5. N. A. Lotova, D. F. Blums, and K. V. Vladimirskii, Astron. Astrophys. **150**, 266 (1985).
6. N. A. Lotova, Ya. V. Pisarenko, and O. A. Korelov, Issled. Geomagn. Aeron. Fiz. Solntsa **32**, 78 (1992).
7. N. A. Lotova, O. A. Korelov, and Ya. V. Pisarenko, Issled. Geomagn. Aeron. Fiz. Solntsa **33**, 10 (1993).
8. N. A. Lotova, V. N. Obridko, K. V. Vladimirskiĭ, *et al.*, Sol. Phys. **205**, 149 (2002).
9. N. A. Lotova, K. V. Vladimirskiĭ, I. Yu. Yurovskaya, *et al.,* Astron. Zh. **72**, 109 (1995a) [Astron. Rep. **39**, 90 (1995a)].
10. N. A. Lotova, K. V. Vladimirskiĭ, I. Yu. Yurovskaya, and O. A. Korelov, Astron. Zh. **72**, 757 (1995b) [Astron. Rep. **39**, 675 (1995b)].
11. N. A. Lotova, K. V. Vladimirskii, and O. A. Korelov, Sol. Phys. **172**, 225 (1997).
12. N. A. Lotova, K. V. Vladimirskiĭ, and Ya. V. Pisarenko, Dokl. Ross. Akad. Nauk **360**, 1 (1998) [Dokl. Phys. **43**, 359 (1998)].
13. D. O. Muhleman and J. D. Anderson, Astrophys. J. **247**, 1093 (1981).
14. M. Tokumaru, H. Mori, T. Tanaka, and T. Kondo, J. Geomagn. Geoelectr. **47**, 1113 (1995).
15. O. I. Yakovlev, A. I. Efimov, V. M. Razmanov, and V. K. Shtrykov, Astron. Zh. **57**, 790 (1980) [Sov. Astron. **24**, 454 (1980)].
16. O. I. Yakovlev, A. I. Efimov, and S. N. Rubtsov, Astron. Zh. **65**, 1290 (1988) [Sov. Astron. **32**, 672 (1988)].

Translated by G. Rudnitskii

Astronomy Letters, Vol. 30, No. 5, 2004, pp. 349–356. Translated from Pis'ma v Astronomicheskiĭ Zhurnal, Vol. 30, No. 5, 2004, pp. 393–400.

Periodic Orbits in the General Three-Body Problem and the Relationship between Them

V. V. Orlov[1*], A. V. Petrova[1], A. V. Rubinov[1], and A. I. Martynova[2]

[1] *Astronomical Institute, St. Petersburg State University, Universitetskiĭ pr. 28, St. Petersburg, Peterhof, 198504 Russia*

[2] *St. Petersburg Academy of Forestry Engineering, Institutskiĭ per. 5, St. Petersburg, 194021 Russia*

Received October 24, 2003

Abstract—We study the regions of finite motions in the vicinity of three simple stable periodic orbits in the general problem of three equal-mass bodies with a zero angular momentum. Their distinctive feature is that one of the moving bodies periodically passes through the center of mass of the triple system. We consider the dynamical evolution of plane nonrotating triple systems for which the initial conditions are specified in such a way that one of the bodies is located at the center of mass of the triple system. The initial conditions can then be specified by three parameters: the virial coefficient k and the two angles, φ_1 and φ_2, that characterize the orientation of the velocity vectors for the bodies. We scanned the region of variation in these parameters $k \in (0,1)$; $\varphi_1, \varphi_2 \in (0,\pi)$ at steps of $\Delta k = 0.01$; $\Delta\varphi_1 = \Delta\varphi_2 = 1^\circ$ and identified the regions of finite motions surrounding the periodic orbits. These regions are isolated from one another in the space of parameters $(k, \varphi_1, \varphi_2)$. There are bridges that correspond to unstable orbits with long lifetimes between the regions. During the evolution of these metastable systems, the phase trajectory can "stick" to the vicinity of one of the periodic orbits or move from one vicinity to another. The evolution of metastable systems ends with their breakup. © *2004 MAIK "Nauka/Interperiodica"*.

Key words: *celestial mechanics, three-body problem, periodic orbits.*

INTRODUCTION

The search for periodic solutions plays an important role in studying the dynamics of triple systems (see, e.g., Davoust and Broucke (1982), the review by Hadjidemetriou (1984), and the book by Marchal (1990)). According to the KAM theory, stable periodic orbits must be surrounded by finite-motion trajectories.

It is of interest to study the location of finite-motion regions in the space of initial conditions (masses, coordinates, and velocities of the components). The space considered has a large number of dimensions, $D = 21$, making it impossible to search for stability regions via direct scanning of the entire space. The center-of-mass integrals allow the dimension of the space to be reduced down to $D = 15$. Restricted motions appear to be possible only in systems with negative total energy $E < 0$. This fact imposes additional constraints on the part of the space of initial conditions to be considered; however, the number of dimensions remains too large.

At the same time, we can analyze various sections of the region of initial conditions by invoking some additional considerations, e.g., the information about the known periodic solutions.

Consider, e.g., the general problem of three equal-mass bodies with zero total angular momentum. Three types of stable periodic orbits are known for this problem (see von Schubart (1956); Broucke (1979); Moore (1993), and Chenciner and Montgomery (2000)).

The first orbit was found in the rectilinear three-body problem, and Hénon (1977) proved its stability.

Broucke (1979) numerically discovered several periodic orbits in the isosceles problem of three equal-mass bodies. One of these orbits is surrounded by a "tube" consisting of finite-motion trajectories (Zare and Chesley (1998); Orlov *et al.* (2002)) and appears to be stable.

The third of the orbits mentioned above has the shape of the figure eight. Its stability was proved by Simó (2002). Orlov *et al.* (2003) analyzed a series of sections in the vicinity of the figure eight and confirmed that this orbit is surrounded by finite-motion trajectories.

Thus the general three-body problem with equal-mass components and zero angular momentum has at least three likely stable periodic orbits surrounded

[*] E-mail: vor@astro.spbu.ru

by tubes of finite-motion trajectories. A question arises whether these tubes are interconnected or whether they are isolated manifolds. We analyze this problem in our paper.

METHOD OF SIMULATIONS

We first point out that all three orbits under study (Fig. 1) have a common property: in the course of the motion one of the bodies (or each of the three bodies) passes periodically through the center of mass of the triple system. We can use this property to reduce the dimension of the set of initial conditions. In particular, let us analyze such trajectories in the three-body problem with zero angular momentum, where the evolution starts with one of the bodies located at the center of mass of the triple system.

We use the system of units where the masses of bodies are equal to $m_1 = m_2 = m_3 = 1$, the gravitational constant is $G = 1$, and the total energy of the triple system is equal to $E = -1$. All the bodies move in the XY plane.

For such systems, the following relations are satisfied at the initial time instant:

$$\sum_{i=1}^{3} \mathbf{r}_i = 0, \quad (1)$$

$$\sum_{i=1}^{3} \dot{\mathbf{r}}_i = 0,$$

$$\sum_{i=1}^{3} [\mathbf{r}_i \times \dot{\mathbf{r}}_i] = 0,$$

$$\frac{1}{2}\sum_{i=1}^{3} \dot{\mathbf{r}}_i^2 - \sum_{i<j} \frac{1}{r_{ij}} = -1.$$

Here, $\mathbf{r}_i$ $(i = 1, 2, 3)$ is the radius-vector of i-th body in the barycentric coordinate system and r_{ij} are the mutual distances between the bodies.

Suppose that body m_3 is at the center of mass of the system. In this case we have $\mathbf{r}_3 = 0$. We can turn the coordinate system so as to align all three bodies along the X-axis. All bodies have equal masses and therefore $x_1 + x_2 = 0$. The fact that the angular momentum of the triple system is equal to zero, combined with the condition of the immobility of the center of mass, implies that $\dot{y}_1 = \dot{y}_2, \dot{y}_3 = -2\dot{y}_1, \dot{x}_3 = -\dot{x}_1 - \dot{x}_2$.

As a result, we have only four quantities $\{x_1, \dot{x}_1, \dot{x}_2, \dot{y}_1\}$ so far left undetermined. Let us substitute them into the energy integral to obtain

$$\dot{x}_1^2 + \dot{x}_2^2 + \dot{x}_1\dot{x}_2 + 3\dot{y}_1^2 - \frac{5}{2|x_1|} = -1. \quad (2)$$

Let us assume, for the sake of definiteness, that body m_1 is located left of the central body, i.e., $x_1 < 0$. Then

$$x_1 = -\frac{5}{2}(\dot{x}_1^2 + \dot{x}_2^2 + \dot{x}_1\dot{x}_2 + 3\dot{y}_1^2 + 1)^{-1}. \quad (3)$$

As a result, three velocity components $\{\dot{x}_1, \dot{x}_2, \dot{y}_1\}$ determine completely the initial conditions. We can use instead of these velocities other parameters, which vary within finite intervals.

One such parameter is the virial coefficient, which is equal to the kinetic-to-potential energy ratio $k \in \{0, 1\}$. The cases $k = 0, 1$ correspond to triple collisions, and we do not consider them here.

Another two parameters determine the directions of motion of the two outer bodies m_1 and m_2. Let us introduce two angles φ_1 and φ_2 such that

$$\tan\varphi_1 = \frac{\dot{y}_1}{\dot{x}_1}, \quad \tan\varphi_2 = \frac{\dot{y}_2}{\dot{x}_2} = \frac{\dot{y}_1}{\dot{x}_2}. \quad (4)$$

Because of the symmetry of motions, it is sufficient to analyze the velocity vectors directed into the upper half-plane, i.e., $\varphi_1, \varphi_2 \in [0°, 180°]$. We can then write velocities $\{\dot{y}_1, \dot{x}_1, \dot{x}_2\}$ in terms of the parameters introduced

$$\dot{y}_1 = \sqrt{\frac{k/(1-k)}{3 + \frac{1}{\tan^2\varphi_1} + \frac{1}{\tan^2\varphi_2} + \frac{1}{\tan\varphi_1 \operatorname{tg}\varphi_2}}}, \quad (5)$$

$$\dot{x}_1 = \frac{\dot{y}_1}{\tan\varphi_1},$$

$$\dot{x}_2 = \frac{\dot{y}_1}{\tan\varphi_2}.$$

The remaining velocity components can be expressed in terms of the condition of the immobility of the center of mass and the area integral:

$$\dot{y}_2 = \dot{y}_1, \quad (6)$$

$$\dot{y}_3 = -2\dot{y}_1,$$

$$\dot{x}_3 = -\dot{x}_1 - \dot{x}_2.$$

The coordinates x_1 and x_2 can be found from Eq. (3) and the integral of center of mass (recall that $x_3 = 0$).

Note that equations (5) become singular at $\varphi_1 = 90°$ and $\varphi_2 = 90°$. At $\varphi_1 = 90°$ we set

$$\dot{y}_1 = \sqrt{\frac{k/(1-k)}{3 + \frac{1}{\tan^2\varphi_2}}}, \quad (7)$$

$$\dot{x}_1 = 0.$$

We correspondingly obtain for $\varphi_2 = 90°$

$$\dot{y}_1 = \sqrt{\frac{k/(1-k)}{3 + \frac{1}{\tan^2\varphi_1}}}. \quad (8)$$

$$\dot{x}_2 = 0$$

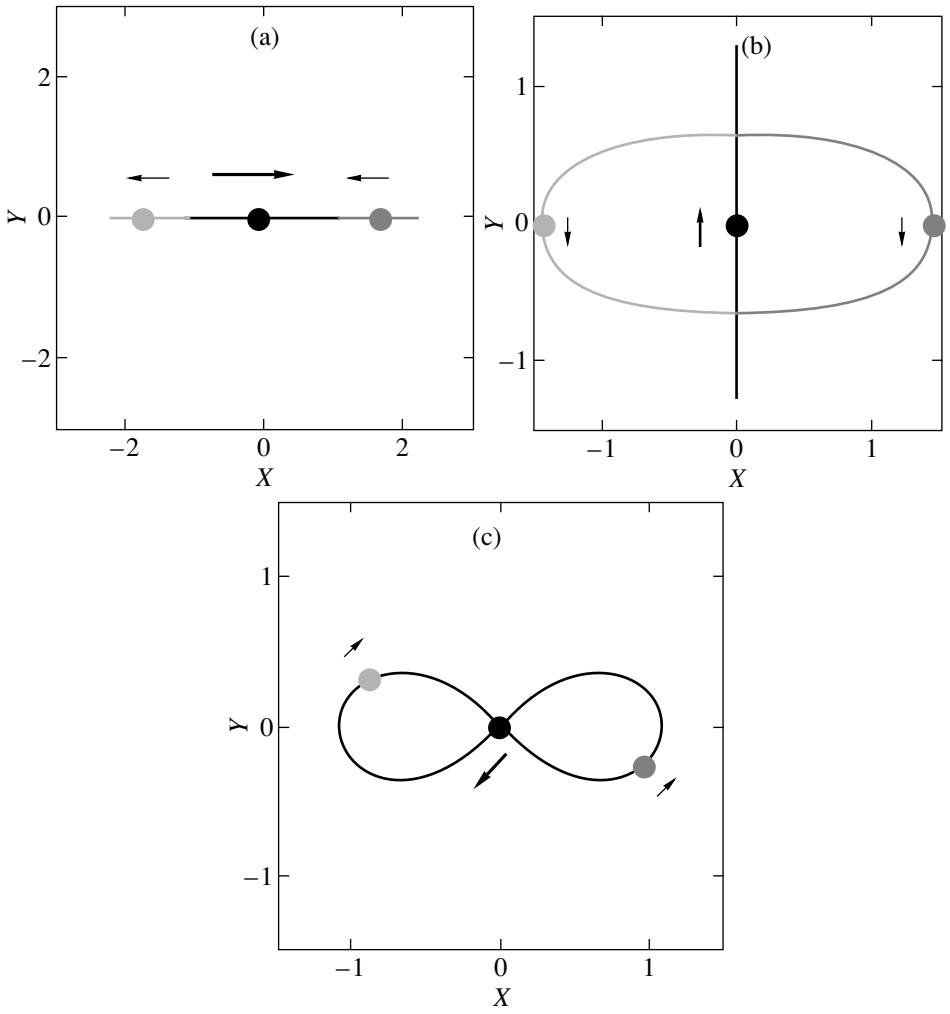

Fig. 1. Von Schubart (a), Broucke (b), and figure-eight (c) orbits in barycentric coordinates.

The remaining components of velocities and coordinates can be computed in the same way as above.

Note also that the cases

$$\varphi_1 + \varphi_2 = 180^\circ \tag{9}$$

correspond to triple collisions, and we do not consider them here.

As a result, we scan the region of initial conditions

$$k \in (0,1); \quad \varphi_1, \varphi_2 \in (0^\circ, 180^\circ); \quad \varphi_1 + \varphi_2 \neq 180^\circ \tag{10}$$

in steps $\Delta k = 0.01$ and $\Delta\varphi_1 = \Delta\varphi_2 = 1^\circ$ in order to identify the finite-motion regions around stable periodic orbits and analyze how the shapes and sizes of these regions vary in response to the variation of parameters (10).

For each variant of initial conditions, we perform computations until the maximum mutual distance $r_{\max}$ exceeds $5d$, where d is the mean size of the triple system

$$d = \frac{m_1m_2 + m_1m_3 + m_2m_3}{|E|} = 3, \tag{11}$$

or until the evolution time exceeds 1000τ, where τ is the mean crossing time

$$\tau = \frac{(m_1 + m_2 + m_3)^{5/2}}{(2|E|)^{3/2}} = \frac{9\sqrt{3}}{2\sqrt{2}}. \tag{12}$$

We assumed that a system with a lifetime of $>1000\tau$ may have finite motions. In the systems of the first kind, we fixed the time T, when condition $r_{\max} > 5d$ was satisfied. After this, the evolution of the triple system passes into the "triple encounter–ejection" mode (see, e.g., Orlov *et al.* (2001)), which ends with the breakup of the system—the escape of one of the bodies into a hyperbolic orbit.

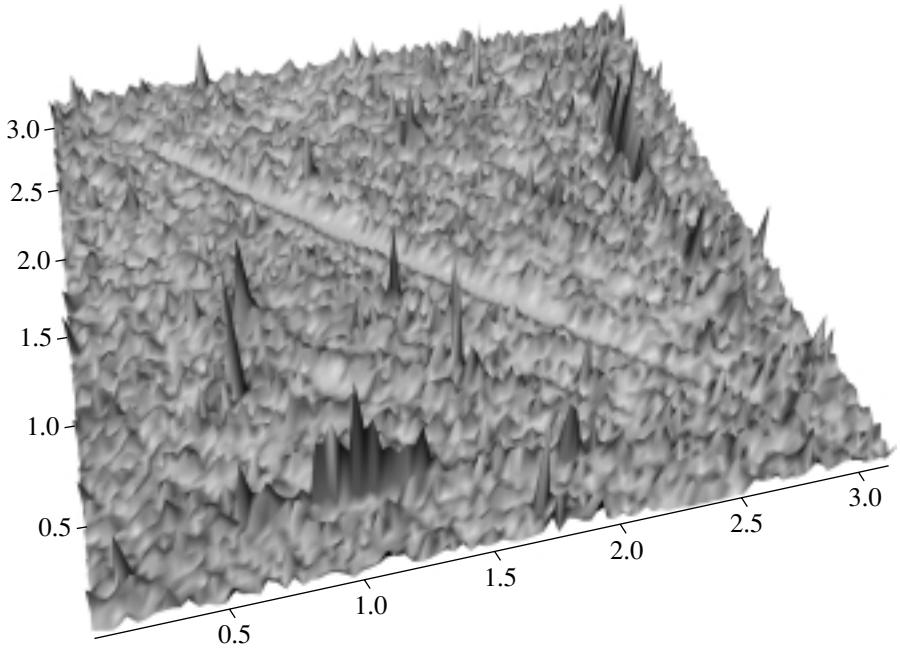

Fig. 2. The structure of relief $T(\varphi_1, \varphi_2)$ at $k = 0.1$.

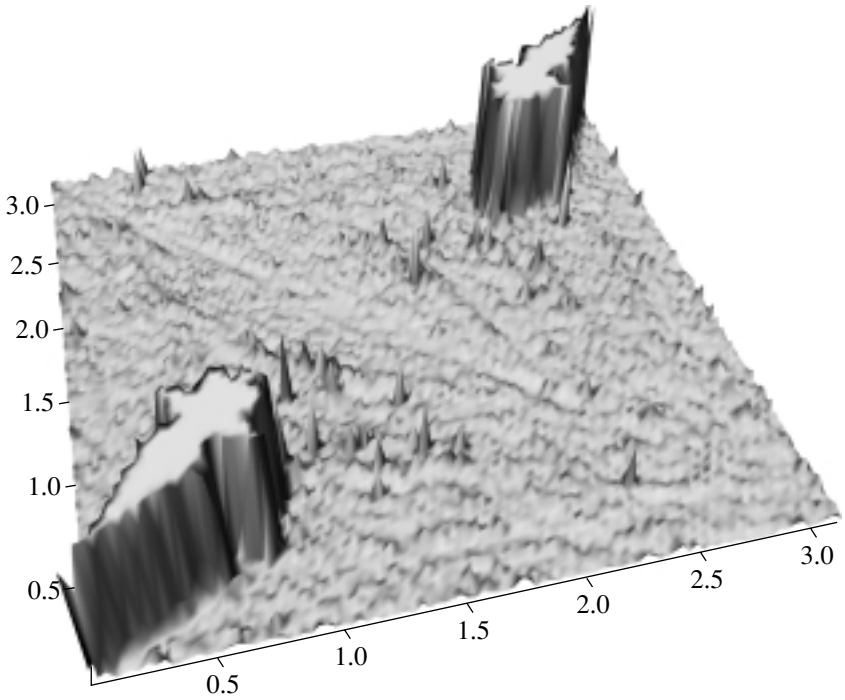

Fig. 3. The structure of relief $T(\varphi_1, \varphi_2)$ at $k = 0.2$.

RESULTS

It is convenient to represent the results of a three-dimensional scanning of the region of initial conditions in the space of parameters $(k, \varphi_1, \varphi_2)$ as two-dimensional sections (φ_1, φ_2) at fixed k. Figures 2–6 show the evolution of sections as a function of increasing virial coefficient. The figures have the form of reliefs: "highland" areas correspond to longer evolution of the system until the criterion $r_{\max} > 5d$ is satisfied. The upper plateaus correspond to systems where this condition was not satisfied during time

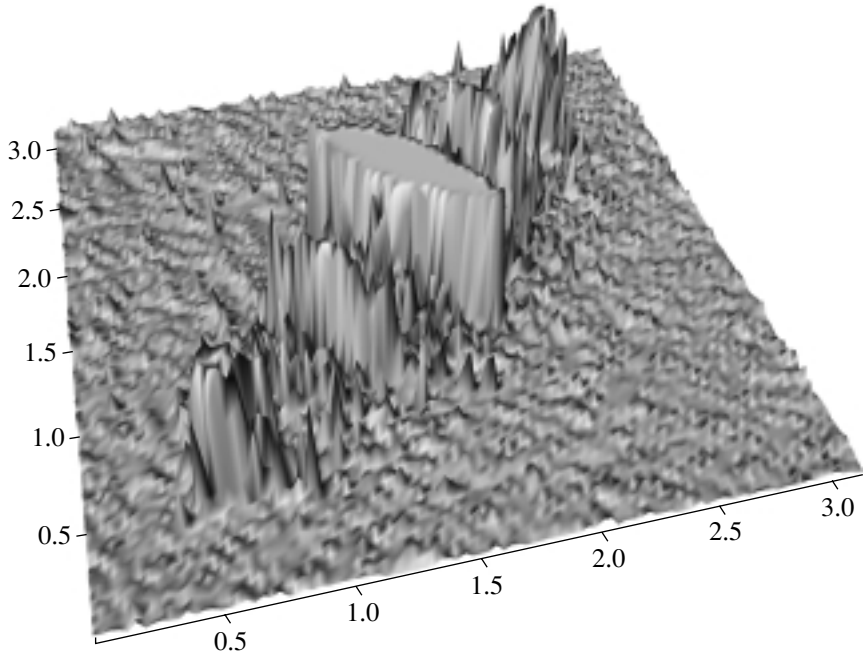

Fig. 4. The structure of relief $T(\varphi_1, \varphi_2)$ at $k = 0.4$.

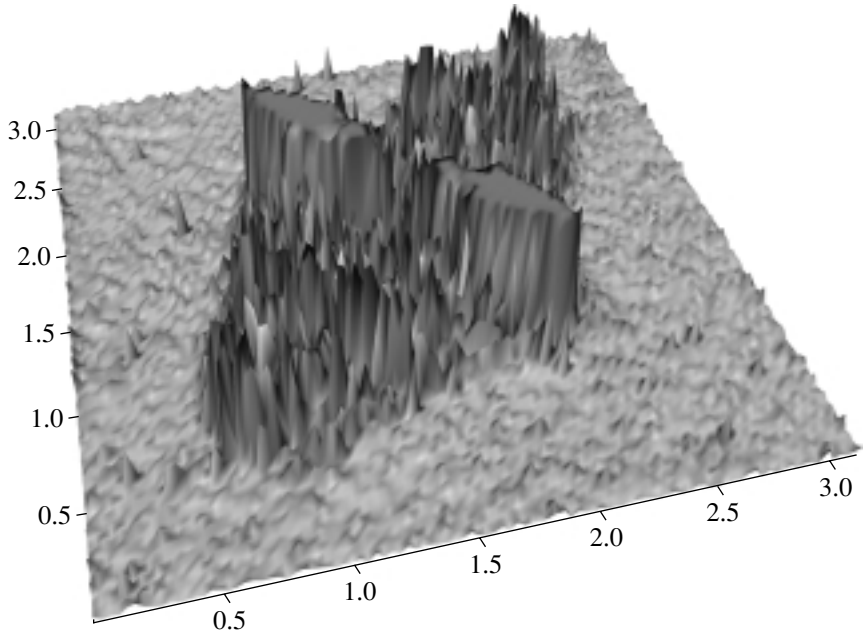

Fig. 5. The structure of relief $T(\varphi_1, \varphi_2)$ at $k = 0.46$.

1000τ. Such systems may have finite motions in the vicinity of stable periodic orbits.

The figures must be symmetric with respect to the line of triple collisions, $\varphi_1 + \varphi_2 = 180°$. This symmetry provides an additional check for the accuracy of the computations.

We found no triple systems with $T > 1000\tau$ at small k (Fig. 2). It appears that at such k, there are no regions of initial conditions under which motions remain for a long time within the region where $r_{\max} < 5d$. At $k \approx 0.15$ finite-motion regions appear in the lower left and upper right corners. The regions stretch out toward each other along the main diagonal $\varphi_1 = \varphi_2$ (Fig. 3). At $k \approx 0.25$ the regions separate from points $\{\varphi_1, \varphi_2\} = \{0°, 0°\}$ and $\{\varphi_1, \varphi_2\} = \{180°, 180°\}$ and become rounder with increasing k.

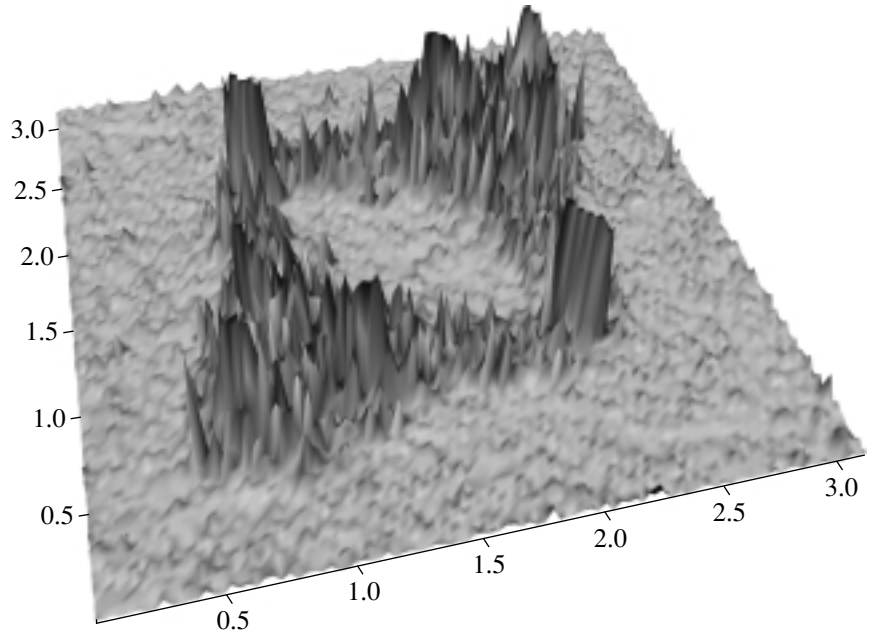

Fig. 6. The structure of relief $T(\varphi_1, \varphi_2)$ at $k = 0.5$.

It may be assumed that these finite-motion regions are associated with the stable periodic orbit of von Schubart (1956).

The further increase of the virial coefficient results in a gradual disruption of the regions associated with the von Schubart orbit and is accompanied by the simultaneous formation of three new regions; one of these emerges in the central part at $\{\varphi_1, \varphi_2\} = \{90°, 90°\}$ and extends along the diagonal $\varphi_1 + \varphi_2 = 180°$, while the other two form arcs that are symmetric with respect to this diagonal (Fig. 4).

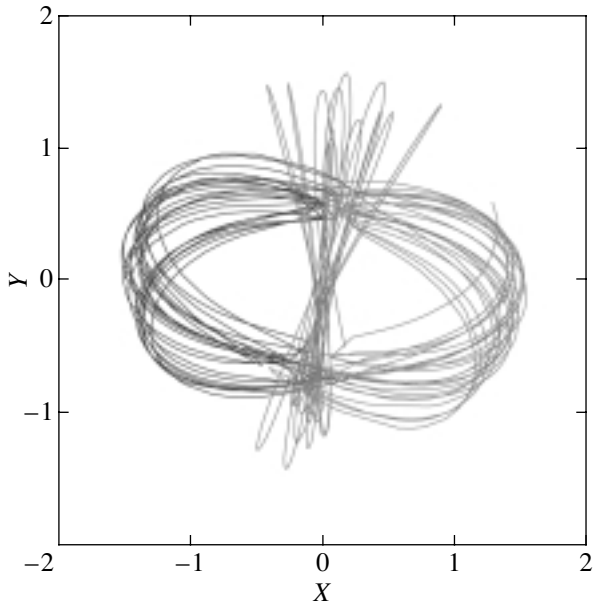

Fig. 7. The trajectories of the motion of bodies in the vicinity of Broucke's orbit.

Five isolated finite-motion regions coexist in a small interval of k values about $k \approx 0.4$. Two regions are associated with the von Schubart orbit; two regions, with the figure-eight orbit; and the central region, with the Broucke orbit (see below).

These regions are connected to each other by a "bridge" of trajectories, which remain for a long time within $r_{\max} < 5d$, but then cease to satisfy this condition. The evolution of these systems appears to end with their breakup.

As k increases, the central region breaks up into two parts separated by a thin bar (Fig. 5). The bar then breaks and a ringlike structure forms that consists of systems where motions remain finite for a long time (Fig. 6). The regions generated by the von Schubart orbit are adjacent to the upper and lower boundary of the ring along the main diagonal. As virial coefficient increases, the ring "dissolves" and the "debris" of the region of the von Schubart orbit continues to exist in a certain interval of k values. However, they too disappear in the end.

The trajectories of bodies that we constructed here with initial conditions taken in the aforementioned regions confirm the conclusions made above (Figs. 7–9). The trajectories in transition regions reproduce the features of those finite-motion orbits that are closest to the initial conditions.

By the behavior of their motion, trajectories in transition regions resemble the metastable systems

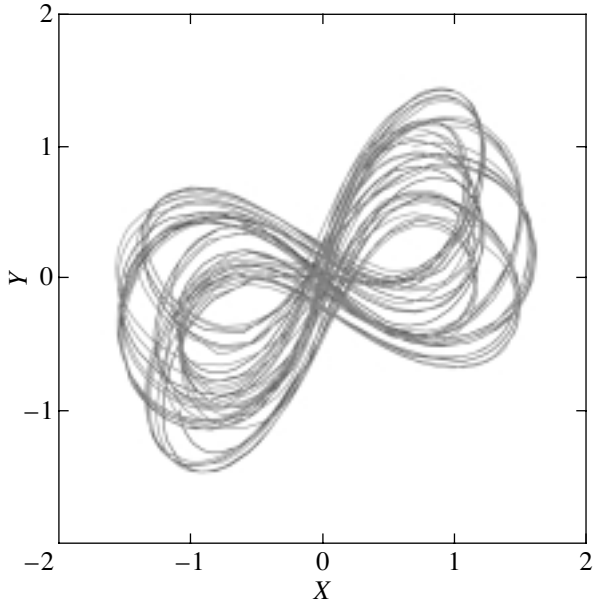

Fig. 8. Trajectories of bodies in the vicinity of the figure-eight orbit.

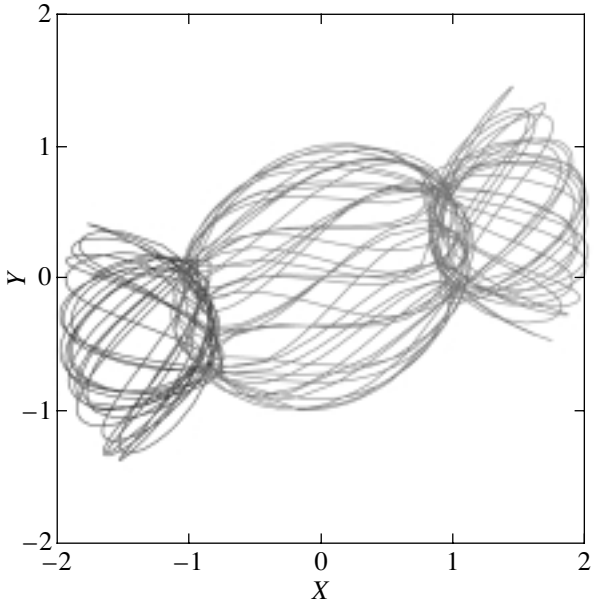

Fig. 9. Trajectories of bodies in the vicinity of the von Schubart orbit.

earlier found in the general three-body problem with zero initial velocities (Martynova *et al.* 2003). There is, however, an important difference: The trajectories considered by Martynova *et al.* (2003) pass into the metastable mode (sometimes very long) sometime after the start of the evolution. In this paper, the initial conditions for transition regions are already selected in regions of metastability.

DISCUSSION

In this paper, we have considered the dynamics of triple systems with equal-mass components and zero angular momentum. The initial conditions were chosen in such a way that all of the bodies are on one straight line, with one of the bodies being halfway between the other two. Such conditions are realized in three stable periodic orbits.

Each of the orbits is surrounded by a region of trajectories with finite motions, i.e., stable according to Lagrange. We were interested in the question of whether these regions of stability are connected with each other. The answer proved to be negative; the stability regions are isolated in the phase-space section considered here. However, we cannot rule out the possibility of their joining in other dimensions.

Another result obtained here is the discovery of a "bridge" of long-lived but unstable systems connecting the stability regions. Typical motions in these systems resemble those in neighboring regions of stability, but triple encounters and ejections of bodies begin some time after the onset of evolution. As a result, the triple system breaks up.

The structure of the region of initial conditions corresponding to the trajectories with finite motions evolves with increasing virial coefficient k as follows:

(1) the emergence and growth of the region generated by the von Schubart orbit;

(2) the roughly simultaneous appearance of regions around the figure-eight and the Broucke orbit;

(3) the coexistence of the regions generated by all three orbits connected by the "bridge" of long-lived, but breaking-up systems;

(4) the breakup of the region generated by the Broucke orbit into two parts connected by a thin bar;

(5) the formation of a ring of long-lived trajectories with two protrusions generated by the von Schubart orbit;

(6) the disruption of the ring structure;

(7) the disappearance of the "ruins" of the region of long-lived trajectories connected with the von Schubart orbit.

Thus, the regions of stable motions generated by the von Schubart orbit are observed over a wider range of virial coefficients than the stability regions associated with the other two orbits. The smallest stability region is that surrounding the figure-eight orbit.

In conclusion, let us note that the pattern of motions in long-lived but breaking-up systems resembles the dynamics of metastable systems that we identified previously.

Since the regions of initial conditions corresponding to the trajectories with finite motions have a

nonzero dimension, such motions can in principle take place in actual triple systems of stars or galaxies. Some of the observed nonhierarchical triple stars and triplets of galaxies can have similar motions if they had initial formation conditions in the vicinity of one of the stable periodic orbits.

ACKNOWLEDGMENTS

V.V. Orlov, A.V. Petrova, and A.V. Rubinov thank the Foundation for Support of Leading Scientific School (project no. 1078.2003.02), the Russian Foundation for Basic Research (project no. 02-02-17516), and the Universities of Russia program of the Ministry of Education of the Russian Federation (project no. UR.02.01.027).

REFERENCES

1. R. Broucke, Astron. Astrophys. **73**, 303 (1979).
2. A. Chenciner and R. Montgomery, Ann. Math. **52**, 881 (2000).
3. E. Davoust and R. Broucke, Astron. Astrophys. **112**, 305 (1982).
4. J. D. Hadjidemetriou, Celest. Mech. **34**, 379 (1984).
5. M. Hénon, Celest. Mech. **15**, 243 (1977).
6. C. Marchal, *The Three-Body Problem* (Elsevier, Amsterdam, 1990).
7. A. I. Martynova, V. V. Orlov, and A. V. Rubinov, Mon. Not. R. Astron. Soc. **344**, 1091 (2003).
8. C. Moore, Phys. Rev. Lett. **70**, 3675 (1993).
9. V. V. Orlov, A. V. Petrova, and A. I. Martynova, Pis'ma Astron. Zh. **27**, 549 (2001) [Astron. Lett. **27**, 470 (2001)].
10. V. V. Orlov, A. V. Petrova, and A. I. Martynova, Mon. Not. R. Astron. Soc. **333**, 495 (2002).
11. V. V. Orlov, A. V. Rubinov, and A. D. Chernin, Pis'ma Astron. Zh. **29**, 148 (2003) [Astron. Lett. **29**, 126 (2003)].
12. C. Simó, Preprint (Univ. of Barcelona, Spain, 2002).
13. J. von Schubart, Astron. Nachr. **283**, 17 (1956).
14. K. Zare and S. Chesley, Chaos **8**, 475 (1998).

Translated by A. Dambis